

Modelling of radio emission from cosmic ray air showers

Zur Erlangung des akademischen Grades eines
DOKTORS DER NATURWISSENSCHAFTEN
von der Fakultät für Physik
des Karlsruher Instituts für Technologie (KIT)

genehmigte
DISSERTATION

von Marianne Ludwig
aus Oldenburg

Tag der mündlichen Prüfung: 17.06.2011

Referent: Prof. J. Blümer

Korreferent: Prof. M. Feindt

Betreuer: Dr. T. Huege

Modelling of radio emission from cosmic ray air showers

Cosmic rays entering the Earth's atmosphere induce extensive air showers consisting of up to billions of secondary particles. Among them, a multitude of electrons and positrons are generated. These get deflected in the Earth's magnetic field, creating time-varying transverse currents. Thereby, the air shower emits coherent radiation in the MHz frequency range measured by radio antenna arrays on the ground such as LOPES at the KIT. This detection method provides a possibility to study cosmic rays with energies above 10^{17} eV. At this time, the radio technique undergoes the change from prototype experiments to large scale application. Thus, a detailed understanding of the radio emission process is needed more than ever.

Before starting this work, different models made conflicting predictions on the pulse shape and the amplitude of the radio signal. It turned out that a radiation component caused by the variation of the number of charged particles within the air shower was missed in several models. The Monte Carlo code REAS2 superposing the radiation of the individual air shower electrons and positrons was one of those. At this time, it was not known how to take the missing component into account. For REAS3, we developed and implemented the endpoint formalism, a universal approach, to calculate the radiation from each single particle.

For the first time, we achieve a good agreement between REAS3 and MGMR, an independent and completely different simulation approach. In contrast to REAS3, MGMR is based on a macroscopic approach and on parametrisations of the air shower. We studied the differences in the underlying air shower models to explain the remaining deviations.

For comparisons with LOPES data, we developed a new method which allows "top-down" simulations of air showers. From this, we developed an air shower selection criterion based on the number of muons measured with KASCADE to take shower-to-shower fluctuations for a single event analysis into account. With this method, we simulate for the first time the radio emission from an air shower directly comparable with the measured one. We validated with a comparison between REAS3 simulations and LOPES data that the understanding of the radio emission from air showers increased significantly. REAS3 is the first simulation predicting lateral slope parameters and electric fields as measured with LOPES without using any free parameters.

Last but not least, we show the didactic quality of the endpoint formalism. This formalism can be used to calculate any radiation from accelerated charged particles, which allows an increased insight in the radiation phenomena of classical electrodynamics. Thus, the endpoint formalism provides a universal tool which is relevant for scientists in many different fields.

Modellierung der Radioemission von Luftschauern kosmischer Strahlung

Beim Eintritt hochenergetischer kosmischer Strahlung in die Erdatmosphäre entstehen Luftschauer aus mehreren Milliarden Teilchen, hauptsächlich Elektronen und Positronen, die im Erdmagnetfeld abgelenkt werden und dabei sich zeitlich ändernde transversale Ströme induzieren. Hierbei wird elektromagnetische Strahlung im MHz-Frequenzbereich erzeugt, welche mit Antennenfeldern gemessen wird, z.B. mit LOPES am KIT. Trotz ihres geringen Flusses kann so kosmische Strahlung mit Energien $\geq 10^{17}$ eV untersucht werden. Derzeit findet der Übergang von Prototyp- zu großskaligen Experimenten statt, weshalb fundierte Kenntnisse des Emissionsmechanismus wichtiger als je zuvor sind.

Bisher widersprachen sich verschiedene Modelle in der Vorhersage der Pulsform und Amplitude des Radiosignals. Wie sich herausstellte, fehlten einigen Modellen ein Strahlungsbeitrag erzeugt durch die sich zeitlich ändernde Anzahl der Ladungsträger. Darunter war REAS2, das die Radioemission des Luftschauers durch Überlagerung der Beiträge einzelner Teilchen berechnet. Noch zu Beginn dieser Arbeit war unklar, wie die fehlende Strahlung berücksichtigt werden kann. Wir entwickelten einen universellen Ansatz basierend auf der Betrachtung der Emission an den Endpunkten, der eine vollständige Beschreibung aller Emissionsprozesse gewährleistet, und implementierten ihn in REAS3.

Erstmalig erzielten wir im Vergleich zwischen zwei unabhängigen und komplementären Modellen, REAS3 und MGMR, eine gute Übereinstimmung. Im Gegensatz zu REAS3 basiert das makroskopische Modell MGMR auf Parametrisierungen des Luftschauers. Wir untersuchten die Unterschiede der verwendeten Luftschauermodelle, um verbleibende Unstimmigkeiten zu erklären.

Für den Vergleich mit LOPES-Daten entwickelten wir ein neues Auswahlverfahren basierend auf der von KASCADE gemessenen Anzahl der Myonen, um Schauer-zu-Schauer Fluktuationen zu berücksichtigen. Dieses Verfahren erlaubt "top-down"-Simulationen von Luftschauern und wurde von uns erstmalig zur Luftschauersimulation genutzt, die direkt mit den gemessenen Schauern vergleichbar sind. Mit dem Vergleich zwischen Simulationen und LOPES-Daten bestätigten wir die deutliche Verbesserung des Verständnisses der Radioemission. REAS3 trifft als erste Simulation und ohne Verwendung freier Parameter Vorhersagen für Werte der lateralen Verteilungsfunktion und der Amplitude des elektrischen Felds, die vergleichbar mit den von LOPES gemessenen Werten sind.

Abschließend zeigen wir die didaktische Stärke des Endpunktformalismus. Dieser Ansatz ermöglicht die Beschreibung sämtlicher Strahlungsprozesse beschleunigter, geladener Teilchen, was tiefere Einblicke in die Strahlungsphänomene der klassischen Elektrodynamik zulässt. Der Endpunktformalismus ist demnach ein universelles Werkzeug für Wissenschaftler vieler verschiedener Forschungsfelder.

Contents

Abstract	i
1 Introduction	1
2 Cosmic rays and radio detection	3
2.1 The energy spectrum of cosmic rays	4
2.2 Observing techniques	6
2.2.1 Direct cosmic ray measurements	6
2.2.2 Extensive air showers	7
2.2.3 Indirect cosmic ray measurements	10
2.3 Radio measurements and experiments	13
2.3.1 Current set-ups of radio experiments	13
3 Modelling approaches for radio emission from air showers	17
3.1 Recent simulation approaches	18
3.1.1 Models predicting unipolar pulses	18
3.1.2 Models predicting bipolar pulses	19
3.1.3 REAS	21
3.1.4 MGMR	23
3.1.5 REAS2 vs. MGMR	23
3.1.6 REAS2 vs. LOPES data	24
3.2 The missing radiation component	26
4 REAS3	29
4.1 Simulation algorithm of REAS	29
4.2 Contributions due to charge variation	30
4.3 Continuous vs. discrete calculation	32

4.4	Numerical stability	34
4.5	Results of REAS3	35
4.5.1	REAS2 vs. REAS3	36
4.5.2	Discussion of charge excess emission	40
4.6	Incorporation of the refractive index	43
5	Details of the pulse shape	47
5.1	Particle energy	48
5.2	Lateral distance	50
5.3	Shower phases	52
5.4	Geometric height	54
6	Comparison of REAS3 and MGMR simulations	59
6.1	REAS3 vs. MGMR	60
6.1.1	Emission from a vertical air shower	62
6.1.2	Emission from an inclined air shower	65
6.1.3	Specific magnetic field configurations	68
6.1.4	Discussion of the comparison	69
6.2	Simplified REAS3 vs. MGMR	70
7	Comparison of REAS3 with LOPES data	73
7.1	Methods of air shower selections	75
7.1.1	Application to LOPES data	78
7.2	Results of the comparison with LOPES data	82
8	A universal endpoint formalism	91
8.1	Liénard-Wiechert potentials	92
8.2	Radiation from one endpoint	93
8.2.1	The time-domain derivation	94
8.2.2	The frequency-domain derivation	95
8.2.3	Building physical situations	96
8.3	Application to established theory	98
8.4	Discussion of the endpoint formalism	100
9	Conclusion	103
	Bibliography	105
	Danksagung	117

CHAPTER 1

Introduction

In 1912, Victor Hess opened a new field of physics research with his discovery of cosmic rays (Hess, 1912). With the observation of cosmic rays, a lot of progress in the field of particle physics was achieved. New particles have been found, namely the positron (Anderson, 1933), muon and pion (Neddermeyer and Anderson, 1937), before their production was possible in man-made accelerators. Furthermore, cosmic rays are still the only way to study ultra-high energy particle physics. However, after nearly 100 years of research, several open questions remain related to the origin, the acceleration and the propagation of cosmic rays in outer space (see, e.g., Gaisser and Stanev (2006)). To study cosmic rays, two different methods exist: direct and indirect measurements which themselves split again in many different detection techniques. For cosmic ray energies larger than 10^{15} eV, the flux of cosmic rays is too low to measure them directly in space since large detector areas and long observation times are needed. Hence, indirect measurements with ground-based experiments are used to detect the extensive air showers induced by cosmic rays in the Earth's atmosphere.

Extensive air showers are created in the Earth's atmosphere when a high-energy cosmic ray particle interacts with the atmosphere's nuclei (Auger et al., 1939). In further interactions, particle cascades consisting of billions of secondary particles are generated, electrons and positrons prominent among those. Due to their deflection in the Earth's magnetic field, the electrons and positrons induce time-varying transverse currents which lead to radio emission from the air shower. This emission is beamed in forward direction, since the electrons and positrons are highly relativistic.

Hence, one way to measure these air showers is the detection of their radio emission with antenna arrays on ground. Already 50 years ago, measurements of

the radio signal from air showers have been performed (Jelley et al., 1965), but the restrictions due to analogue data processing, precision of the measurements and the limited understanding of the emission mechanism were too large and the development of this technique was stopped.

In the last decade, the radio technique was reconsidered, developed further and the interest in this detection method was renewed (Horneffer et al., 2004; Falcke et al., 2005; Ardouin et al., 2005, 2006; Apel et al., 2006). Since a few years, the radio detection technique became even an option for large scale experiments of the next generation because its duty cycle is roughly 95% and the results obtained so far are promising (van den Berg et al., 2007, 2009; Melissas et al., 2010). With this increased interest, the importance of understanding the emission mechanisms in detail intensified and several simulation approaches came up (Huege, 2009). The different modelling approaches, however, made conflicting predictions on the radio signal.

The differences of the models have been of qualitative and quantitative nature (Huege et al., 2010b). Several models, in particular time-domain based ones, predicted unipolar pulses, whereas the pulse shapes predicted by other models were bipolar. The heights of the predicted amplitudes differed by factors of 10 and more. However, from theoretical arguments it became clear that the pulse shape of the radio signal has to be bipolar which is equivalent to frequency spectra dropping to zero for zero frequency. Since the radio emission from an air shower happens on finite time scales in finite space, the zero frequency cannot contain any power, which would belong to infinite time scales (Scholten and Werner, 2009).

One of the approaches predicting unipolar pulses was the Monte Carlo code REAS, which calculates the **R**adio **E**mission from **A**ir **S**howers by superposing the radiation of the individual electrons and positrons of the air shower. It became clear that REAS2 (Huege et al., 2007) and all the other models predicting unipolar pulses were missing a radiation component caused by the variation of the number of charged particles in the air shower. However, before starting this work, it was unclear how the missing radiation component could be implemented in the model and if some other effects might be missed.

Within the scope of this work, a universal approach, the endpoint formalism, was developed to include the missing radiation component in REAS (Ludwig and Huege, 2010b) and thereby reconciling the microscopic and macroscopic models. The details on the implementation and the resultant progress achieved with the implementation of the endpoint formalism in REAS3 is presented in this work.

CHAPTER 2

Cosmic rays and radio detection

In the early 20th century, Victor Hess discovered an increase of the electric conductivity of air with larger atmospheric height which he ascribed to an ionising radiation called “*Höhenstrahlung*”. In 1912, Hess made this discovery during balloon flights for which he was awarded with the Nobel-prize in 1936. Today, this radiation is known as “*cosmic rays*” which consists of charged particles, mainly protons and nuclei and only a few percent of electrons. The exact composition, however, depends on the origin and therefore on the energy of the cosmic rays and is in some parts of the energy spectrum (see section 2.1) still not known precisely. As the sources of cosmic rays, galactic as well as extragalactic objects are discussed (Blümer et al., 2009). As galactic sources, supernovae are generally accepted candidates (Baade and Zwicky, 1934) and their shock fronts as galactic accelerators for energies below $Z \cdot 10^{14}$ eV (Lagage and Cesarsky, 1983). For higher energies, the sources are not yet established but active galactic nuclei (AGN) are discussed as candidates (Protheroe and Szabo, 1992; Berezhko, 2008). Furthermore, it is not verified but assumed, that cosmic rays with the highest energies are all of extragalactic origin (Sigl et al., 1994). The interest in high-energy cosmic rays is not only caused by the thirst for knowledge on the origin of astroparticles from outer space but also by the possibility to study elementary particle physics at very high energies, since ground-based particle accelerators such as the LHC at CERN cannot accelerate particles to energies comparable to the highest cosmic ray energies. Thus, cosmic rays are the link between astronomy with large structures and particle interactions at a microscopic scale.

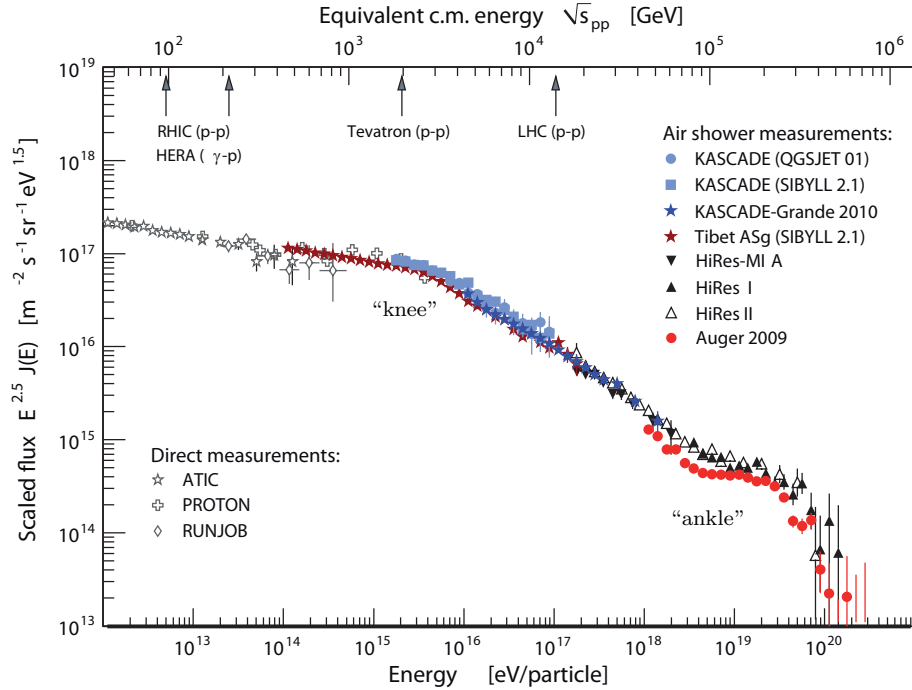


Figure 2.1: The energy spectrum of cosmic rays (Blümer et al., 2009). The flux of the cosmic rays is scaled by $E^{2.5}$. The flux was measured by several experiments sensitive in different energy ranges.

2.1

The energy spectrum of cosmic rays

The flux of cosmic rays depends strongly on the energy of the cosmic ray particles. This is illustrated by the energy spectrum of cosmic rays as can be seen in Figure 2.1. There, the flux of cosmic rays is scaled with $E^{2.5}$ versus the primary energy of the cosmic ray particle. The cosmic ray flux as well as the energy extend over many orders of magnitude. The energy spectrum is describable by a power law with the spectral index γ :

$$\frac{dN}{dE} \sim E^{-\gamma} \quad (2.1)$$

In the wide range of the energy spectrum, two main features exist. One of them is the so called “*knee*” at the energy around 10^{15} eV where the spectral index γ changes from 2.7 to 3.0. Today, mainly three different models are discussed to explain this behaviour:

First, the galactic accelerators run out of power for higher energetic particles. This means, there is a maximum energy reachable by the acceleration of cosmic rays such as supernova shock front acceleration (first order Fermi acceleration

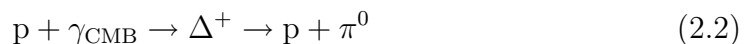
(Fermi, 1949)). The change of the composition to heavier particles (Apel et al., 2009) and a second knee expected at the energy of the “*iron knee*” (Apel et al., 2010c) bears this approach out.

Second, the magnetic fields of the Milky Way are not strong enough to keep higher energetic particles in the galaxy. Thus, the higher energetic particles escape from our galaxy faster and do not reach the Earth’s atmosphere (Ptuskin et al., 1993; Swordy, 1995).

The third explanation is linked to particle physics (Kazanas and Nicolaidis, 2003). Since at these energies no ground based accelerator data existed before LHC, the interaction models are purely based on theories and extrapolation from lower energetic interactions but not on experimental data. With exotic interactions of the particles in the atmosphere at energies higher than 10^{15} eV, one part of the primary energy of the cosmic ray might pass into a new decay channel, such as the creation of a neutralino. If this channel is not measured, the primary energy is underestimated from the reconstructions and thus, the knee in the spectrum arises. Even first LHC data seems to exclude such scenarios. A detailed overview on the existing theories is given in (Hörandel, 2004).

At the energy of 10^{18} eV, the spectral index drops from 3.0 to 2.7, i.e. the energy spectrum gets flatter again. This second feature of the energy spectrum is called the “*ankle*”. One explanation for the flattening is that the cosmic rays with higher energies originate from extragalactic sources with a different energy spectrum than the galactic cosmic rays. The exact energy region for the transition of galactic to extra-galactic cosmic rays is still unknown. The approaches explaining the ankle are distinguishable by their prediction for the transition energy: the dip model predicts the transition from galactic to extragalactic around the second knee and the ankle is generated due to the Bethe-Heitler process (Berezinsky, Veniamin, 2005). Hence, in this model, the extragalactic cosmic rays with energies above the ankle are only protons. The transition model assumes the transition region to be directly at the ankle. A mixed composition is possible but not needed (Allard et al., 2005). With today’s experimental data at the highest energies, both models are feasible. However, the transition model is preferred, since it allows a mixed composition and the data give hints on existing heavy nuclei at highest energies (Abraham et al., 2010a).

At the very high energies, larger than $5 \cdot 10^{19}$ eV, the flux of cosmic rays drops very fast. This is consistent with the predictions made by Greisen (1966) and Zatsepin and Kuzmin (1966). They predicted a cut-off in the energy spectrum due to the excitation of the high energetic cosmic ray protons by the cosmic microwave background photons to the Δ^+ -resonance, i.e.



The proton loses a fraction of its energy, which is used to produce a neutral pion.

For heavier cosmic rays, similar cut-off predictions exist at fractionally different energies. The mean free path length of protons with energies larger than 10^{20} eV is 50 Mpc. Therefore, cosmic rays detected on the Earth with energies larger than 10^{20} eV need to originate from near-by sources. As a different explanation for the suppression of cosmic rays at the highest energies it is discussed that the maximum energy is reached by extragalactic accelerators (Medvedev, 2007).

Since the flux of cosmic rays strongly depends on the energy, different detection methods are used to observe cosmic rays and thus study their sources, their propagation and acceleration. The observing techniques are briefly presented in the following section.

2.2

Observing techniques

To measure cosmic rays, several observing techniques exist and new methods are being investigated, in particular radio detection. The applicability of the detection method depends on the explored energy range of cosmic rays. For energies below the knee (cf. section 2.1), it is possible to detect cosmic rays directly (cf. section 2.2.1) with balloon or satellite experiments, i.e. in the upper part of the atmosphere or even above. For higher energies, the direct measurement of cosmic rays is no longer suitable due to the low flux of cosmic rays and indirect measurements are necessary, since they provide a larger detection area. Therefore, so-called extensive air showers (discussed in section 2.2.2) have to be measured and by analysing the characteristics of the air shower, e.g. the particle energy and the particle density, information on the primary cosmic rays is derived. The measurement of air showers is realised by ground-based measurements which are discussed in section 2.2.3.

2.2.1

Direct cosmic ray measurements

Learning about the composition and the origin of cosmic rays is one big aim in the field of astroparticle physics. Measuring cosmic rays directly in space answers the question about the composition. With detectors installed on satellites or balloons high in the atmosphere, the primary cosmic rays are measured before they interact with the Earth's atmosphere (for an overview, see e.g., Putze (2010)). However, the sources are not identifiable by detecting the charged nuclei as charged particles become deflected in the galactic magnetic fields, losing their directional information. By direct detections for energies below 10^{15} eV, the mass spectrum of galactic cosmic rays is known very well (Simpson, 1983). It has nearly the same composition as the matter in the solar system as shown in figure 2.2. The excess of the light elements Lithium, Beryllium and Boron is explained by spallation, i.e. they are generated from heavier elements while traversing the

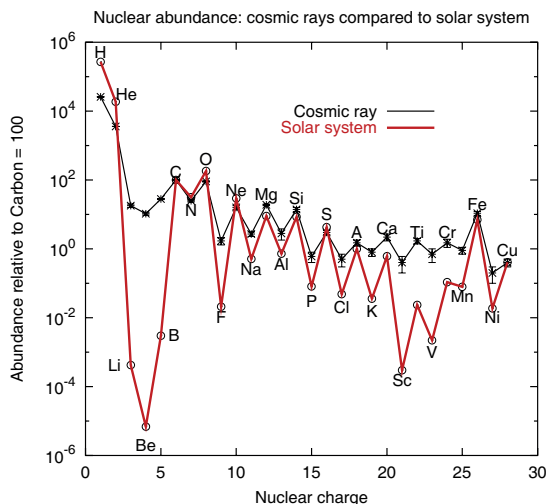


Figure 2.2: Comparison of the mass spectra of the galactic cosmic rays with energies less than 10^{15} eV with the elementary composition of the solar system (Gaisser and Stanev, 2006).

universe and interacting with the interstellar medium. For higher energies, the detection areas for direct measurements get too small since the cosmic ray flux is decreasing rapidly.

2.2.2

Extensive air showers

When a cosmic ray enters the Earth's atmosphere, it interacts with nuclei of the air and new particles are generated which are known as secondary cosmic ray particles (Auger et al., 1939). Depending on the cosmic ray mass and thus the cross section of the cosmic ray interaction with the atmospheric nuclei, the first interaction is higher or lower in the atmosphere (Gaisser et al., 1978).

A very simple model to describe the development of electromagnetic cascades was presented by Heitler (1954). Recently, this model was adapted to describe basic air shower physics of hadronic showers as well (Matthews, 2005). In the electromagnetic cascade, electrons and positrons emit a gamma by bremsstrahlung after the radiation length, while the gamma produces new electrons and gammas after the same length due to pair production. This results in 2^n particles after n radiation lengths. Thus, the primary energy is in first order proportional to the final number of particles. A sketch of the Heitler model is shown in figure 2.3

The hadronic interactions are described similar to the electromagnetic cascades. The hadrons interact and generate charged and neutral pions after traversing one radiation length. Neutral pions decay into two photons building electromagnetic subshowers. The hadronic cascades differ from the electromagnetic cascades in

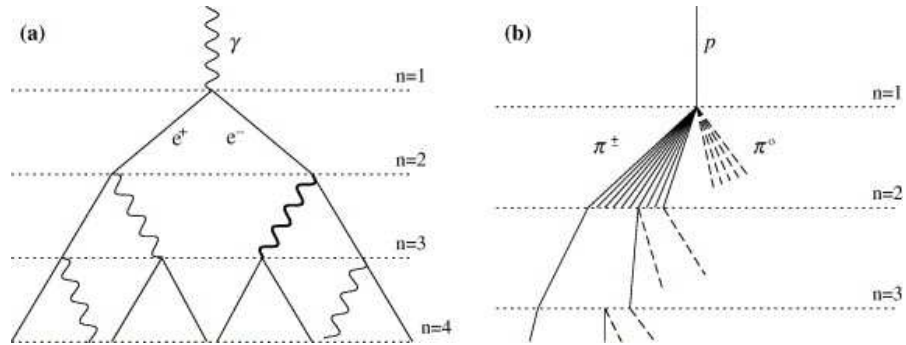


Figure 2.3: Sketch of Heitler's model for an electromagnetic cascade (lhs) and a hadronic shower (rhs). The dashed lines in the hadronic shower represent π^0 decaying quickly and building electromagnetic subshowers. After the second level not all pion lines are shown (Matthews, 2005).

particular due to the transfer of only two thirds of the energy into the hadronic component. In this case, the primary energy can be estimated as proportional to a combination of the number of generated particles (not only hadrons).

In the electromagnetic and the hadronic cascade, a maximum of generated particles is reached with a critical energy of the secondaries. In the case of the electromagnetic cascade, this critical energy represents the energy where ionisation losses start to dominate over bremsstrahlung. The hadronic cascade dies out when the charged pions reach the critical energy where they more likely decay (mainly into muons) than interact. The position where the number of particles reaches the maximum is known as the shower maximum of the air shower X_{\max} .

As shown in figure 2.4, the hadronic air shower can be divided in three different components: the muonic, the hadronic and the electromagnetic component. During the first few interactions, most of the secondary particles are hadrons, such as π^0 , π^+ , π^- and Kaons. Due to multiple interaction channels and different cross-sections, the first few interactions are not fixed for a specific primary particle, i.e. the air shower development is not equal for cosmic rays with the same mass, energy and origin. The arising shower-to-shower fluctuations are mainly determined by these first interactions.

The hadrons have high momenta in the direction of the shower, thus, they are clustered around the shower axis. A large fraction of the air shower energy is carried by the hadronic component and hence, they determine the development of the air shower. In further interactions, they produce more Kaons and pions. Moreover, the Kaons and charged pions mainly decay into muons. A part of these muons is decaying into electrons and positrons. Due to the large decay length of the muons, almost all of the muons produced in the air shower reach the ground without losing much of their energy through Bremsstrahlung. The π^0 particles

1999) due to the differences in the longitudinal development of the electromagnetic and muonic cascades depending on the mass of the primary particle. With larger mass of the primary particle, the total amount of particles in the air shower is increasing and thus the energy per particle is decreasing. This results in less electrons but more muons at ground for larger mass numbers. Moreover, the lateral distribution of electrons and muons differ for different primary particles (Antoni et al., 2005).

The detection of air showers is used to study cosmic rays with energies larger than 10^{15} eV. However, the identification of the composition of the primary cosmic rays is much more difficult than for direct measurements. The principles of these so-called indirect measurements of cosmic rays are explained in the following section.

2.2.3

Indirect cosmic ray measurements

To detect cosmic ray air showers, several techniques exist. The applicability of each detection method depends on the aim of the experiment, since every detection method has its own advantages and constraints. Therefore, combining complementary methods permits more detailed studies on the extensive air showers and the relation of shower characteristics to the primary cosmic rays. These “hybrid” measurements are already performed, for example at the Pierre Auger Observatory (Dawson and et al., 2007). In the following, the different detection techniques will be introduced and examples for their deployment at different experimental sites will be given. An overview over the existing detection methods of cosmic ray air showers is shown in figure 2.5 and discussed in (Haungs et al., 2003).

Particle detectors

The most traditional detection method of cosmic ray air showers is to measure the charged particles of the air shower which reach the ground. For this purpose, several detectors are placed on an area at the ground. The distance of the individual detectors depends on the observation level and energy range the experiment is interested in, since the extension of the air shower is increasing with higher primary energy and the total cost should be minimized. With a high number of such particle detectors, the “footprint” of the air shower on ground is measured. With particle detectors, it is possible to determine the arrival direction and the energy of the primary particle. The reconstruction of the primary energy, however, is strongly dependent on the hadronic interaction models. They are based on the cross-sections of the high-energetic particles, which have to be extrapolated from ground-based acceleration data (Knapp et al., 2003; Menjo et al., 2011). To distinguish between muons and electrons, a shielding of the detectors need to be used or the detectors are buried below the Earth’s surface. With these detectors,

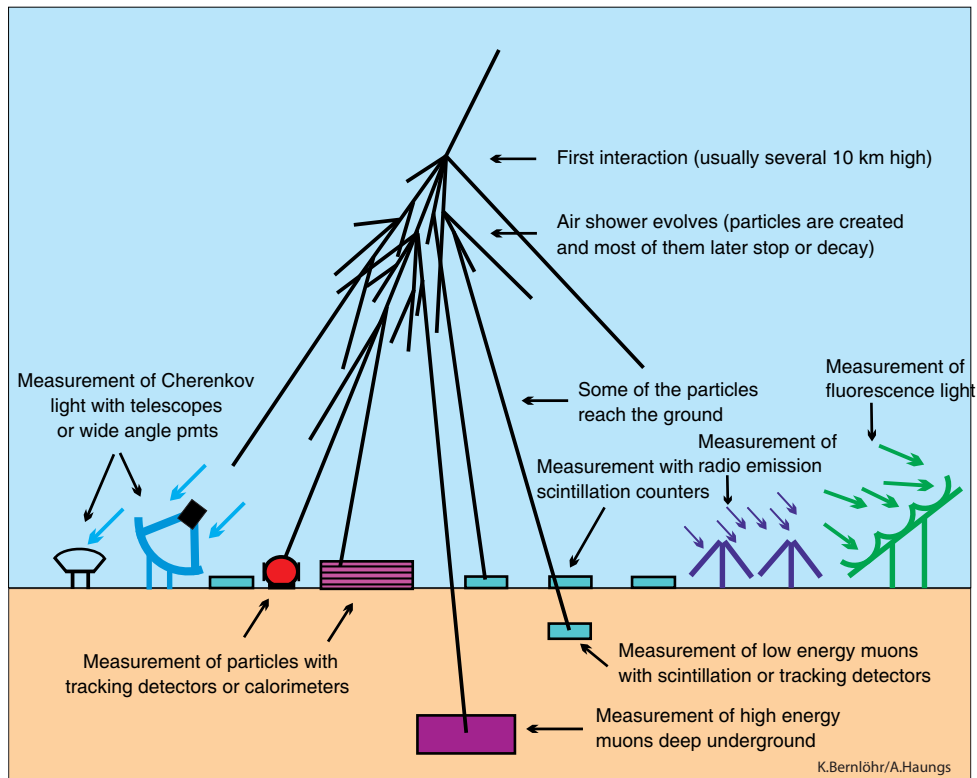


Figure 2.5: Overview over the different methods for the detection of an extensive air shower produced in the Earth's atmosphere, after Haungs et al. (2003).

only muons are measured, since these penetrate more matter than the electrons and positrons. To reconstruct the mean production height of muons, the muon tracks are measured in a position-resolving gas detector. Furthermore, for the detection of the hadronic component, calorimeters are used.

Typical particle detectors are scintillators or water-cherenkov tanks. A detailed overview on experiments measuring the charged secondary particles is given in Blümer et al. (2009). Liquid and plastic scintillators as well as gas detectors and a calorimeter are used by KASCADE (Antoni et al., 2003) and KASCADE-Grande (Apel et al., 2010b) in Karlsruhe, Germany. Water-cherenkov tanks are deployed as the surface detectors from the Pierre Auger Observatory (Pierre Auger Collaboration, 1996) located in Argentina.

Fluorescence detectors

The second detection method deployed at the Pierre Auger Observatory is the detection of the fluorescence light which is emitted by excited nitrogen molecules. The excitation occurs when a highly relativistic particle of an air shower interacts

with a nitrogen molecule of the atmosphere. Due to the transition into the ground state, the nitrogen molecule emits a photon at wavelengths of ultraviolet light, the fluorescence light (for an overview on the fluorescence technique and experiments see, e.g., Arqueros et al. (2008)). With large telescopes, the fluorescence light emitted by the excited nitrogen molecules is detected. Since this technique has to be very sensitive to light, its operation time is limited to moonless and cloudless nights. Therefore, the duty cycle is roughly 13-15% (Abraham et al., 2010b). The fluorescence detection has a low uncertainty of 22% for the determination of the primary energy and of the shower maximum X_{\max} of $20 \frac{\text{g}}{\text{cm}^2}$ (Abraham et al., 2010b) since it detects the longitudinal evolution of the air shower and not the footprint at the ground.

On smaller scales than the Pierre Auger Observatory, the Telescope Array (Telescope Array Collaboration, 2011) located in Utah (USA) is using the fluorescence detection together with ground-based particle detectors (scintillators). The Fly's Eye experiment was the first air shower fluorescence telescope which began taking data in 1982 (Baltrusaitis et al., 1985).

Cherenkov detectors

Charged secondary particles with relativistic velocities generate Cherenkov radiation in the atmosphere. The Cherenkov radiation is strongly beamed in forward direction of the air shower (Giller et al., 2004). Two different kinds of detectors are used for the measurements of the Cherenkov light.

On the one hand, large telescopes detect the Cherenkov light from gamma induced air showers above 100 GeV to TeV. These telescopes consist of spherical mirrors and photomultiplier cameras as, e.g., employed at HESS (Hinton, 2004) in Namibia. Aim of the Cherenkov telescopes is to find and study the sources of high energetic gamma rays. Since gammas do not get deflected by the magnetic fields in the universe, they point back to their sources.

On the other hand, wide angle photomultipliers installed at the ground in an array detect the Cherenkov light of cosmic ray air showers. This is the case for the TUNKA experiment in Siberia (Budnev and et al., 2009). The aim is to study the energy spectrum and the composition of cosmic rays at energies below 10^{18} eV. The detection of Cherenkov light is limited to moon- and cloudless nights like the detection of fluorescence light.

For the next years, the new experiment CTA (CTA consortium, 2010) is planned to detect the Cherenkov light from very high energetic gammas in the northern and southern hemisphere. The aim is to study the non-thermal high-energy universe. The final design and the location is not decided yet. A review on Cherenkov methods and other experiments is given by Lidvansky (2005).

Radio detectors

In recent years, an additional detection technique of air showers was established: the detection of the radio emission produced by the electromagnetic component of the air shower in the MHz range. The radio emission of air showers contains information on the longitudinal development of the air shower, similar as does fluorescence and Cherenkov light. The aim of the detection of radio emission is the reconstruction of the primary energy, the arrival direction and the mass of the primary particle, respectively the determination of the shower maximum X_{\max} . Details on this technique will be given in the following section. Radio detection does not depend on dark nights, but only on stable atmospheric electric fields. The measurement of the radio signal from the air shower is limited by thunderstorms and lightnings during which the electric field is high and unstable (Buitink et al., 2007). Nevertheless, the duty cycle of radio measurements is around 95% (Apel et al., 2011). A further limitation of the radio detection technique is man made noise which is reducible by using frequency filters or choosing a radio quiet area for the experimental site (Nigl et al., 2008). Furthermore, transient noise is making self-triggering difficult (Asch, 2009).

The measurements of GHz emission of an air shower is another method, which is new in the field of the indirect detection of cosmic rays. So far, this technique is under investigation and small groups started to work on this topic (Privitera, 2010). One of the GHz experiments is located in Karlsruhe, where the emission is studied in the scope of CROME (Werner, 2011).

2.3

Radio measurements and experiments

Already in the 1960s, the radio signal from air showers was detected and a correlation between the polarisation vector of the emission and the geomagnetic angle between the shower axis and the Earth's magnetic field was found (Jelley et al., 1965). For a review, see e.g., Allan (1971). However, after these very basic measurements, the application of radio emission from air showers was stopped since the restrictions due to the analogue technique available at that time were too high. Instead, other detection methods have been developed further, in particular the fluorescence method. But, progress in digital signal processing in particular for a new generation of low frequency radio telescope arrays for astronomy led to new activities in the field of cosmic ray radio detection in the last years. With advanced digital techniques, on the one hand interferometric analyses are possible. On the other hand, high quality signal processing such as filtering of transient noise sources became possible. Nearly 10 years ago, the first modern radio experiments started taking data.

2.3.1

Current set-ups of radio experiments

The high duty cycle of the radio detection method and the moderate costs for constructing the first antenna arrays have been very promising to further investigate this detection technique. Hence, new projects in this field started and already many results have been published (Melissas et al., 2010). In the following, an overview of the existing radio experiments is given.

LOPES

One of the most prominent experiments for the development of the radio detection of air showers is LOPES¹ (Falcke et al., 2005) which is integrated in the KASCADE field at the Karlsruhe Institute of Technology in Germany. KASCADE (Antoni et al., 2003) and KASCADE-Grande (Apel et al., 2010b) provide LOPES with a trigger and high-quality information of each measured air shower. In 2003, LOPES started with 10 antennas detecting the east-west polarised component of the radio signal. Several times, LOPES was reconfigured. Today, it is measuring all three polarisation components of the electric field vector with 10 antennas, i.e. 30 channels. The effective bandwidth of LOPES is 43-76 MHz and the primary energy range is $10^{16.7}$ eV – 10^{18} eV. The challenge at the KIT site is the noisy environment. The LOPES collaboration published a number of results such as the dependence of the radio signal on the geomagnetic angle, the amplitude of the radio signal on the energy (Horneffer et al., 2008), details on polarisation studies (Isar et al., 2009), the influence of electric fields in the atmosphere (Buitink et al., 2007), the lateral distribution function of the radio signal (Apel et al., 2010a) and many more (for an overview, please see Huege et al. (2010b); Link et al. (2011b)).

CODALEMA

CODALEMA² (Ardouin et al., 2005, 2006) started with the detection of radio emission from air showers roughly at the same time as LOPES. It is located at the Nançay radio observatory in France, where the human made noise is much less than at the LOPES site. CODALEMA started to measure with conical log-periodic antennas in the frequency band of 1-100 MHz and later replaced the array with active dipoles measuring in the frequency range of 1-220 MHz. Furthermore, scintillators have been put at the site of CODALEMA to get complementary information on the air shower. The effective energy range is $5 \cdot 10^{16}$ eV – 10^{18} eV. With CODALEMA, many results such as the reconstruction of the position of the shower core (Ardouin et al., 2005) and the exponential behaviour of the lateral distribution of the radio signal (Ravel, 2010) were achieved.

¹LOPES: **LO**FAR **P**rototype **S**tation

²CODALEMA: **C**osmic ray **D**etection **A**rray with **L**ogarithmic **E**lectro**M**agnetic **A**ntennas

AERA (Pierre Auger Observatory)

At the Pierre Auger Observatory, the research activities started already in 2007 with two smaller test set-ups. Meanwhile, AERA³ (Fliescher et al., 2010) is one of the enhancements of the Pierre Auger Observatory. Many collaborators of LOPES and CODALEMA share their expertise in the Pierre Auger Collaboration. The aim is to study the radio emission from cosmic rays on larger scales and at very high energies, since LOPES and CODALEMA run out of statistic for energies higher than 10^{18} eV. Since October 2010, the first phase of the set-up consisting of 24 antennas is deployed and data are being taken. The radio enhancement is colocated with AMIGA⁴ (Platino, 2009), an enhancement to measure muons and reduce the energy threshold to 10^{17} eV. In the future, within AERA, 161 antennas will be installed and the potential of super-hybrid measurements and radio detection as a large-scale stand-alone detection technique will be studied.

TREND

A very young radio experiment is TREND⁵ (Ardouin et al., 2010) located at the 21 cm array radio telescope in China. In 2009, the first prototype set-up consisting of 6 antennas was finished and started taking data. As a next step, 50 further antennas are being deployed. The science goal of TREND is to detect highly inclined air showers, particularly neutrino induced air showers. The chosen site is ideal for this purpose, since the radio background is very small at the 21cm array radio telescope and the site is surrounded by mountains where τ -neutrinos induce air showers with a high probability.

LOFAR

LOFAR⁶ (Röttgering et al., 2003; Falcke et al., 2006) is designed as a digital low frequency interferometer, mainly for radio astronomy purposes. In particular, LOFAR studies cosmic ray air showers and neutrino induced particle showers in the lunar regolith. LOPES was primarily built as a prototype station for LOFAR to ensure that the detection of air showers by their radio emission is possible. The antenna arrays of LOFAR mainly stretch across the Netherlands. Some of the detector stations are located in other European countries. The opening ceremony of LOFAR was in June 2010 and first pulsar polarisation profiles are published on the LOFAR webpage (LOFAR Team, 2011). The core of LOFAR (many antennas at a dense area) mainly will be used for cosmic ray detection and thus will be equipped with high density of antennas. Detailed air shower information from particle detectors is not available yet (Horneffer, 2010), but an array consisting

³AERA: Auger Engineering Radio Array

⁴AMIGA: Auger Muons and Infill for the Ground Array

⁵TREND: The TIANSHAN Radio Experiment for Neutrino Detection

⁶LOFAR: Low Frequency Array

of scintillators is planned to be built.

To summarise, the progress achieved in the field of radio detection from cosmic ray air showers is very promising. In recent years, several experiments detecting the radio emission from air showers published results or started taking data as discussed above. With the development of the detection technique, a number of theoretical models came up. In the next chapter, some of them are introduced and the state of the art regarding the theoretical understanding at the beginning of this thesis is given.

CHAPTER 3

Modelling approaches for radio emission from air showers

Over the past years the interest in the detection of radio emission from extensive air showers increased continuously due to its promising potential and the results derived with experiments such as LOPES and CODALEMA. To understand the measurements and to study the cosmic rays with the help of radio detection, detailed simulations and a solid theoretical understanding are needed. Since the activities in the measurements of radio emission from air showers increased, in parallel also several models arose during the last years.

Already in 1966, Kahn and Lerche showed that the emission process in air is dominated by geomagnetic effects, when they developed the first analytical model (Kahn and Lerche, 1966). In section 3.1, the latest simulation approaches are introduced. With the comparison between different models, it became obvious that there was a lack of theoretical understanding (cf. section 3.1.5). The main reason for the conflicting predictions of the models is uncovered within this work and is discussed in section 3.2.

REAS2¹, moreover, was the first simulation which was used to compare theoretical results with measured data from the LOPES experiment. The comparison of LOPES data with REAS2 simulations confirmed that there are still open questions in the theory of radio emission. In section 3.1.6, the results of this first comparison are summarised and open problems are discussed shortly.

¹Radio Emission from Air Showers

3.1

Recent simulation approaches

Already in 1965, radio emission from cosmic ray air showers was discovered (Jelley et al., 1965) and theoretical predictions were made. With the years, the number of models increased rapidly. Unfortunately only incomplete information on the historical modelling approaches has been published in journals and most of the models itself were making strongly simplifying assumptions (for more details on the early modelling approaches we refer to the review of Allan (1971)). One consequence was that in the last years when the interest in the detection of radio emission from air showers revived, completely new modelling approaches arose since this seemed to be most promising.

In recent years, it turned out that the existing models made conflicting predictions regarding the pulse shapes. On the one hand, there are simulations predicting unipolar pulses and on the other hand, models exist which obtain bipolar pulses for the radio signal of an air shower. In the following sections, thus, several selected simulation approaches which had been already published before the beginning of this work are presented. They are categorised by their pulse shape since this was the fundamental difference of the several models and contains physics information of the radio emission from air showers. A more detailed overview can be found in (Huege et al., 2006).

In section 3.1.3, REAS and its history is described in more detail since this is the basis of the present work. REAS will be compared in detail with MGMR, the macroscopic model of geomagnetic radiation. Hence, this model will be introduced in section 3.1.4 in somewhat greater depth.

3.1.1

Models predicting unipolar pulses

Interestingly, all of the models predicting unipolar pulses work in the time-domain. There is no model calculating the radio signal in the frequency-domain obtaining unipolar pulses. However, also models calculating the radio pulse in the time-domain predict bipolar pulses (as will be introduced in section 3.1.2). The fundamental idea for a number of models has its origin in an article of Falcke and Gorham (2003). They described that radio emission from cosmic ray air showers originates from the single electrons and positrons accelerated in the Earth's magnetic field. Due to the geomagnetic deflection it was called the geosynchrotron approach. In the same year, the first model was published by Suprun et al. (2003) predicting a unipolar pulse shape of the radio signal and frequency spectra levelling off at low frequencies. The next model predicting unipolar pulses was REAS1 (Huege and Falcke, 2005a) which is a Monte Carlo code based on the geosynchrotron approach. REAS1 was developed further (Huege and Falcke, 2005b) and with the newer version REAS2, the details of the air shower characteristics are taken into account (Huege et al., 2007). A similar approach was

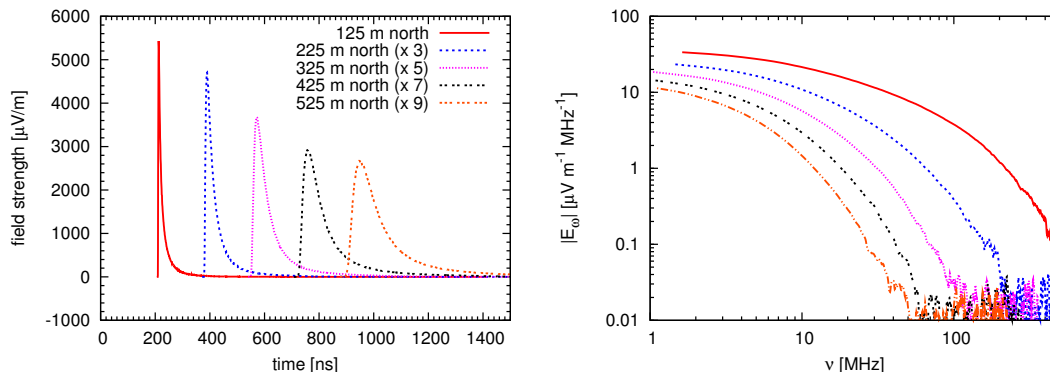


Figure 3.1: Unipolar pulses of REAS2 (left) and the corresponding frequency spectra (right) for an air shower with primary energy of 10^{18} eV and a zenith angle of 30° (Huege et al., 2010a). The frequency spectra level off at low frequencies.

made by DuVernois et al. (2005), when they implemented the geosynchrotron approach in the AIRES² code (Sciutto, 1999). REAS2 and the AIRES based model obtained both similar results and unipolar pulses but the height of the amplitudes differed by factors of 10-20 where AIRES predicted higher electric field strengths. In figure 3.1, such unipolar pulses and the corresponding frequency spectra are shown for the example of REAS2 for a proton induced air shower with primary energy of 10^{18} eV and a zenith angle of 30° . The time-domain calculation has the advantage that retardation effects can be treated more easily than in the frequency-domain. Also, since the radio signal occurs localized in time, a lot of technical advantages arise with time-domain implementations. These are reasons why more time-domain models exist than models based on the frequency-domain which are presented in the following section.

3.1.2

Models predicting bipolar pulses

In 2003, an analytical approach was developed in the frequency-domain taking the geosynchrotron approach from Falcke and Gorham as basis (Huege and Falcke, 2003). The model was based on the synchrotron spectra of single particles and therefore predicted frequency spectra which drop to zero for small frequencies. However, in this analytical approach many approximations and simplifications had to be made. In further investigations, Huege and Falcke developed the Monte Carlo code REAS where this behaviour became lost and the pulse shape changed from bipolar to unipolar (cf. section 3.1.1).

In 2005, a frequency-domain model was introduced by Konstantinov et al. (En-

²AIRshower Extended Simulations: AIRES is simulating extensive air showers

gel et al., 2005) which is based on the EGS³ code. The radiation is calculated from straight lines of individual particles and the edges of the trajectories. The two disadvantages of this frequency-domain model are the very time consuming calculations and the need to use approximations such as Fraunhofer approximation. The virtue, however, was the study of the influence of a realistic refractive index and therefore Cherenkov contributions on the radio signal of air showers. The derived results confirmed that the geomagnetic radiation dominates the radio signal from air showers in comparison to Cherenkov-like radiation. More detailed analysis has shown, however, that for realistic air shower calculations these two contributions cannot be strictly separated.

The only time-domain model predicting bipolar pulses published at the start of this work was developed by Scholten et al. and was published in 2008 (Scholten et al., 2008; Werner and Scholten, 2008). This model is based on a macroscopic view of the charged particles in an air shower resulting in transverse currents which are ascribable to the approach made by Kahn and Lerche already in 1966 (Kahn and Lerche, 1966). In contrast to the other time-domain models, MGMR does not superpose the radiation of individual particles but is looking at macroscopic systems of moving charges and changing currents.

Figure 3.2 shows bipolar pulses at different observer positions predicted by MGMR and the corresponding frequency spectra for a vertical air shower with primary energy of 10^{17} eV. The electric field is multiplied by d^2 , where d represents the distance of the observer to the shower axis. In section 3.1.4, the macroscopic model by Scholten et al. is described in greater depth.

The models discussed are listed in table 3.1 sorted by their year of publication. The table contains the information about the predicted pulse shape and whether the model was calculated in the time-domain or the frequency-domain.

3.1.3

REAS

Motivated by the geosynchrotron idea, Huege and Falcke started with the development of an analytical approach to describe the radio emission from extensive air showers. After they started in the frequency-domain, it became obvious that a time-domain calculation would be more convenient for this approach. Furthermore, this first analytical approach in 2003 necessitated many approximations and simplifications (Huege and Falcke, 2003). Consequently, the next step was the implementation of the geosynchrotron approach in a Monte Carlo model. With the C++ based Monte Carlo code REAS1, this was realised and published in 2005 (Huege and Falcke, 2005a,b). REAS1 still was somewhat simplified since it was based on parametrised air showers. Later, with REAS2 it was possible to calcu-

³Electron-Gamma-Shower: code system for Monte Carlo simulation of electron and photon transport

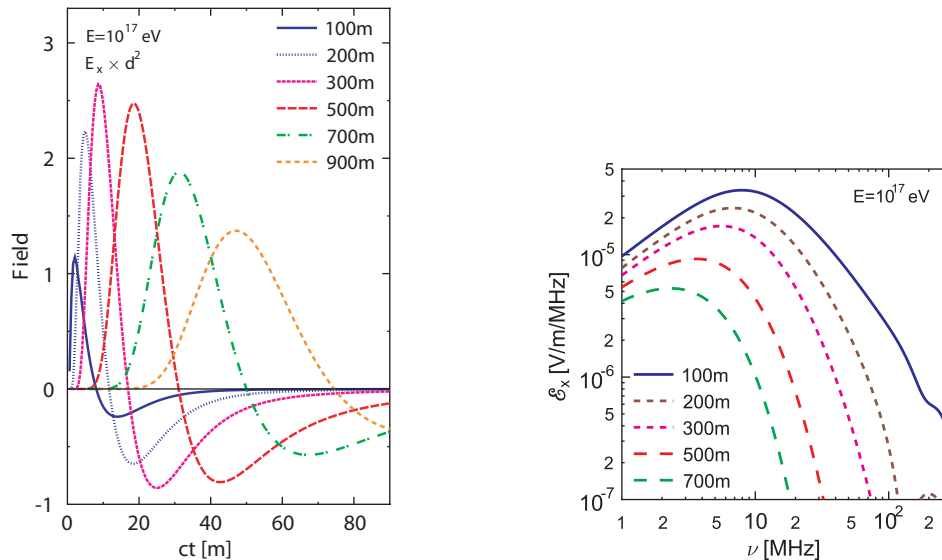


Figure 3.2: Bipolar pulses for the EW-component of the electric field predicted by MGMR (left) with the corresponding frequency spectra (right) for a vertical air shower with primary energy of 10^{17} eV (Scholten et al., 2008). The pulses are multiplied by d^2 , where d represents the distance of the observer to the shower axis. The frequency spectra drop to zero at small frequencies.

Table 3.1: Overview over recent simulation approaches sorted by the year of publication before the beginning of this work. The third row contains information about the pulse shape and the last row about the domain in which the model is calculated.

Publication (Year)	Model	Pulse shape	Domain
Suprun et al. (2003)	Suprun et. al	unipolar	time
Huege and Falcke (2003)	Anal. geosyn.	bipolar	frequency
Huege and Falcke (2005a)	REAS1	unipolar	time
Engel et al. (2005)	EGS-based	bipolar	frequency
DuVernois et al. (2005)	ReAIRES	unipolar	time
Huege et al. (2007)	REAS2	unipolar	time
Scholten et al. (2008)	MGMR	bipolar	time

late radio emission from air showers which had been simulated with CORSIKA⁴ (Heck et al., 1998).

CORSIKA is a Monte Carlo code used for detailed simulation of extensive air

⁴CORSIKA: COsmic Ray SIMulation for KASCADE

showers. Thereby many different primary particles such as protons, iron and photons and several hadronic interaction models for high energy interactions as well as for low energy interactions can be chosen for the simulation. The primary and secondary particles of the air showers are tracked by CORSIKA until they interact or decay. Moreover, various options exist such as for thinning of the air shower or the generation of Cherenkov radiation.

The air shower information derived with CORSIKA is saved in histograms by an interface program COAST⁵ (Lafèbre et al., 2009). These histograms are used by REAS2 to calculate the radio emission from the air shower (Huege et al., 2007).

On the left-hand side of figure 3.3, the scheme of the geosynchrotron approach is shown. While the particles are deflected they emit beamed radiation with an opening angle proportional to $1/\gamma$, where γ represents the Lorentz factor of the particle. The fundamental principle of REAS2 is to calculate the radiation of each of the secondary electrons and positrons and superpose their radiation at the end. The result, therefore, should represent the complete radio emission from this specific air shower. The real strength and quality of REAS2 is that no free physical parameters exist. No approximations have to be made when calculating the radio emission from an extensive air shower. For the calculation, it is sufficient to know the input parameters for this air shower.

3.1.4

MGMR

The macroscopic description of geomagnetic radiation is based on the approach of transverse currents by Kahn and Lerche (1966). With MGMR, a modern implementation of this approach was developed mainly by Scholten and Werner (Scholten et al., 2008; Werner and Scholten, 2008). On the right-hand side of figure 3.3 a sketch of this principle is shown. The electrons and positrons of the extensive air shower are deflected in the Earth's magnetic field. Due to the separation a transverse current \vec{j} is induced perpendicular to the magnetic field. This net electrical current \vec{j} is proportional to the number of charged particles in the shower front. The radio emission depends on the time variation of this current. Since the transverse currents move with the pancake of the air shower, i.e. with speed of light, the emitted radiation is beamed in the forward-direction of the shower axis. Furthermore, the MGMR model takes into account the radiation from a static and a moving dipole.

The basic idea of MGMR is the analytical investigation of the relation between pulse shape and shower profile with short computing times. With the macroscopic view on the air shower characteristics, this is possible. However, a number of simplifications have to be applied and detailed information of the single particles

⁵**CO**rsika **dA**ta **accesS** **T**ools: C++ code providing simple and standardized access to CORSIKA data

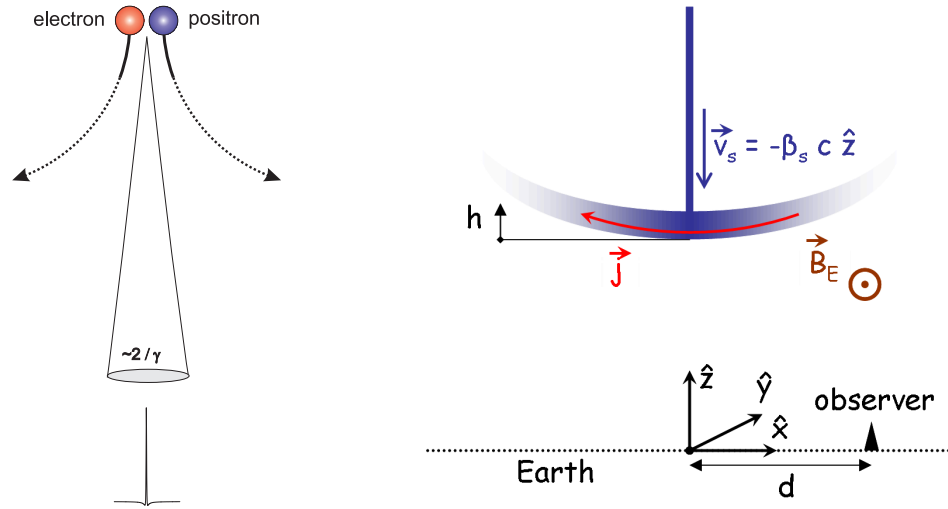


Figure 3.3: Left: The scheme of the geosynchrotron model as implemented in REAS. Electrons and positrons get deflected and emit forward-beamed radiation (REAS-Webpage, 2011). Right: The scheme of the transverse currents as MGMR is based on. The deflection of electrons and positrons leads to transverse currents in the air shower which are changing with time and therefore producing radio emission (Scholten et al., 2008).

is neglected, e.g. the angular distribution of the particles in the shower pancake. To calculate the radio emission from air showers with MGMR, some parameters have to be known before, e.g. the drift velocity of the electrons and positrons in the transverse currents and the charge excess fraction in the air shower which both are assumed to be constant in MGMR.

3.1.5 Consequence of the comparison between REAS2 and MGMR

As already became clear in the previous sections, the pulse shape of REAS2 and MGMR differ. Where REAS2 predicts unipolar pulses for the radio signal, the pulse shape derived with MGMR is bipolar (cf. figures 3.1 and 3.2). In the frequency domain, this corresponds to large differences at low frequencies. In case of MGMR, the field strength is falling to zero for the lowest frequencies and the field strengths predicted by REAS2 are levelling off at a finite value for the low frequency range. This discrepant behaviour enforced the discussions about these models.

From measurements, it was not possible to clarify which pulse shape satisfies the data as the measurements are performed in a specific, limited bandwidth whereas the predictions of the theories are for unlimited bandwidth. In the typical frequency range of the experiments which is around 40-80 MHz, the frequency spectra of REAS2 and MGMR were quite similar. A general physical argument

provided the evidence that the spectral field strength has to drop to zero for very low frequencies (Scholten and Werner, 2009):

The air shower and with this the source of the emission exists only for a finite time in a finite region of space. Thus, the zero-frequency component of the radio emission cannot contain any power, since this would correspond to an infinite time-scale. Hence, the frequency spectra of REAS2 (and all the other models predicting unipolar pulses) cannot be the correct ones. Only now, within the scope of this work the exact origin of this problem was found and is discussed in section 3.2.

3.1.6 Comparison between REAS2 and LOPES data

One aim of simulations is to understand the measured data and help to study the reconstruction possibilities of air-shower parameters from the radio signal. The LOPES collaboration realised a comparison of measured data with the Monte Carlo simulation REAS2, where they compared the characteristics of the lateral distribution of the radio signal (Nehls, 2008; Apel et al., 2010a). For the comparison with data, the simulated radio pulses had to be filtered to a finite observing bandwidth.

In the case of LOPES a filter for the frequency bandwidth of 43 – 76 MHz, the effective bandwidth of LOPES 10, was taken. It has been shown (Apel et al., 2010a) that the lateral distribution approximately follows a decreasing exponential and the electric field ϵ of the single antennas with distance R to the shower core is given by:

$$\epsilon = \epsilon_0 \cdot \exp\left(-\frac{R}{R_0}\right), \quad (3.1)$$

where the fit parameter ϵ_0 specifies the electric field at the core position and R_0 denotes the lateral slope of the distribution. The two parameters have been reconstructed with a set of 110 LOPES measured air showers and the results of the reconstructions from data and simulations have been compared. The input parameters used for the simulations are reconstructed by KASCADE or KASCADE-Grande, i.e. core position, primary energy, zenith and azimuth angle. Each air shower was simulated with CORSIKA where QGSJetII (Ostapchenko, 2006) was chosen as high energy interaction model, UrQmd1.3.1 (Bass et al., 1998) as low energy interaction model and a proton as primary particle. The radio emission from the air shower was simulated by REAS2 without using any parametrisations. In figure 3.4, the result for the scale parameter R_0 is shown. It is obvious that REAS2 predicted smaller scale parameters R_0 , i.e. steeper lateral distributions, than they have been measured with LOPES. The red histogram representing LOPES data shows some events which have a large R_0 , i.e. it is larger than the

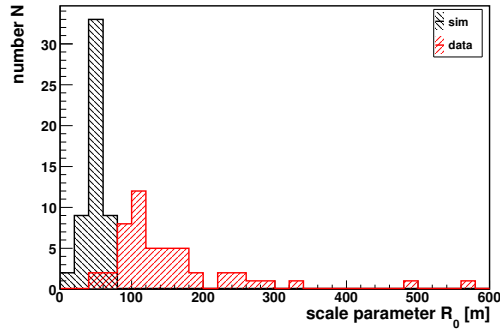


Figure 3.4: Comparison of the scale parameter R_0 derived by REAS2 (black histogram) and reconstructed with LOPES data (red histogram) (Nehls, 2008).

expansion of LOPES (≈ 200 m). Around 10% of all measured data are such flat events. With REAS2 it was not possible to reproduce even one of them.

The parameters ϵ_0 and R_0 are obtained by a fit using equation 3.1 for each of the 110 events. With this fit function, the electric field ϵ_R is calculated at specific distances R for simulations and measured data. The resulting field strengths can be compared with those of the REAS2 simulations. The results for the comparison of the electric field strengths at different lateral distances are illustrated in figure 3.5. Since the scale parameter R_0 was in general larger for the data than for the simulations, it is not surprising that the electric fields predicted by the simulations are larger than the ones measured with LOPES for $R = 0$ m. For $R = 225$ m the simulations predict smaller field strengths than the data. For a distance between $R = 75$ m and $R = 150$ m from the shower core, however, the simulated field strengths nearly all lie close to the expected diagonal, i.e. the simulated field strengths are similar to the measured ones. In spite of the discrepancies, this was promising, since REAS2 did not depend on any free parameters.

In summary, the REAS2 simulations predicted in general steeper lateral slopes than they have been measured with LOPES. Flat events as measured rarely with LOPES were never reproduced by REAS2. This results in systematically higher field strengths ϵ_0 at the core from simulations compared to the measured field strengths. For observer distances around 75 m from the shower core, the field strengths predicted by the simulation agree with the measured data. These results give the hint that the missing radiation contribution indeed was not negligible and that radio emission from air showers was understood in first order but not in detail.

In the course of this work, the missing radiation contribution was identified and we developed a method which allows a canonical implementation in REAS3 (cf. chapter 4). A comparison of REAS3 and LOPES data will show that the

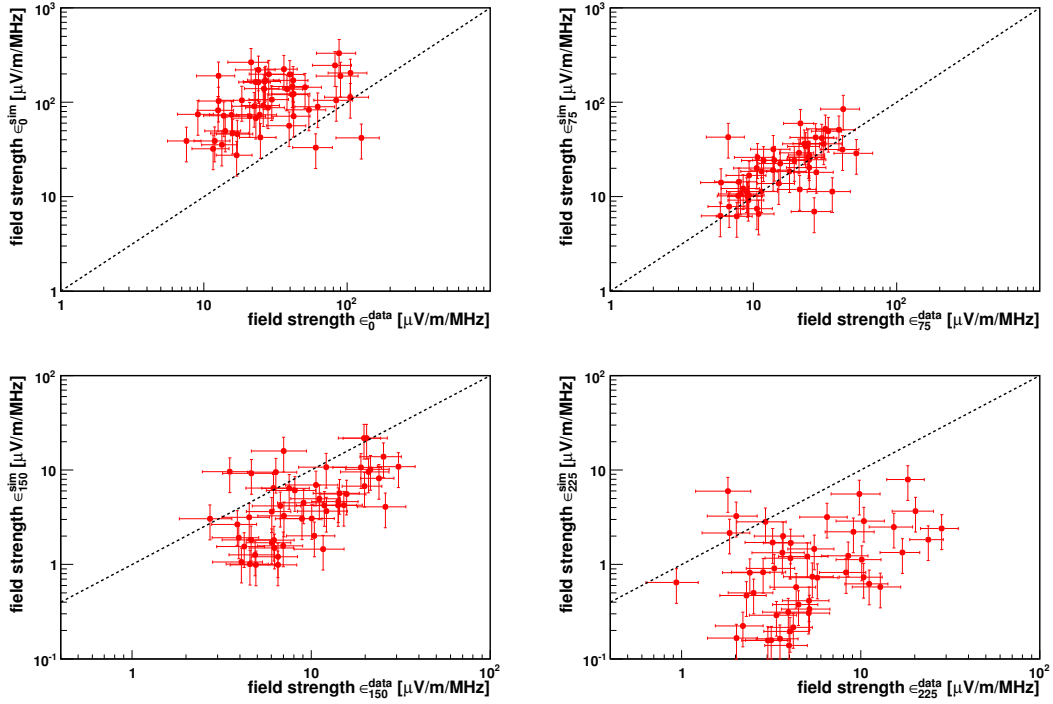


Figure 3.5: Comparison of the field strengths predicted by REAS2 with the measured field strength of LOPES at different distances to the shower core. Points on the diagonal would have equal field strengths for simulations and data (Nehls, 2008).

understanding increased significantly (see discussion in chapter 7).

3.2

The missing radiation component

The main reason for the contradicting results of the different models was that in REAS2 (and all other time-domain approaches based on single particle acceleration) emission due to the variation of the number of charged particles within the air shower was not considered. As a result of this thesis, these missing contributions are taken into account in REAS3 as will be shown in chapter 4. Nowadays, it is understood why so many models missed the above mentioned radiation contribution. For the first time this has been presented on the ARENA conference in 2010 (Huege et al., 2010a). In all of the cases where the models missed a contribution, the basis for the calculation of radio emission from air showers is the description of the electric field $\vec{E}(\vec{x}, t)$ produced by a single moving charged

particle as derived with the Liénard-Wiechert potentials:

$$\vec{E}(\vec{x}, t) = q \left[\frac{\vec{r} - \vec{\beta}}{\gamma^2(1 - \vec{\beta} \cdot \vec{r})^3 R^2} \right]_{\text{ret}} + \frac{q}{c} \left[\frac{\vec{r} \times [(\vec{r} - \vec{\beta}) \times \dot{\vec{\beta}}]}{(1 - \vec{\beta} \cdot \vec{r})^3 R} \right]_{\text{ret}}, \quad (3.2)$$

where $q = \pm e$ indicates the particle charge, $\vec{\beta} = \vec{v}(t)/c$ is given by the particle velocity, $R(t) = |\vec{r}(t)|$ describes the distance between particle and observer position, $\vec{r}(t) = \vec{r}(t)/R(t)$ is the line-of-sight direction between particle and observer, and γ is the Lorentz factor of the particle. The index “ret” means that the equation needs to be evaluated in retarded time.

However, this formula is valid for one charged particle only, whereas the number of charged particles $N(t)$ in an air shower varies with time. The models predicting unipolar pulses effectively integrate the total radio emission in the air shower as:

$$\vec{E}_{\text{tot}}(\vec{x}, t) = N(t)\vec{E}(\vec{x}, t) \quad (3.3)$$

While taking \vec{E}_{tot} as the final radio emission from air showers, there is still a radiation component neglected. Although $N(t)$ is considered explicitly, the contribution resulting from the variation of the number of charged particles is still not regarded. This becomes clear when remembering that the electric field $\vec{E}(\vec{x}, t)$ from a moving charge is derived by

$$\vec{E}(\vec{x}, t) = -\nabla\Phi(\vec{x}, t) - \frac{\partial\vec{A}(\vec{x}, t)}{\partial t} \quad (3.4)$$

where

$$\Phi(\vec{x}, t) = \left[\frac{e}{(1 - n\vec{\beta} \cdot \vec{r})R} \right]_{\text{ret}} \quad \text{and} \quad \vec{A}(\vec{x}, t) = \left[\frac{q\vec{\beta}}{(1 - n\vec{\beta} \cdot \vec{r})} \right]_{\text{ret}} \quad (3.5)$$

are the Liénard-Wiechert potentials. Calculating the electric field not only for one moving charge q but for a number of moving charges $N(t)$, it is obvious that using equation 3.3 will miss some radiation contributions. In the potential $\vec{A}(\vec{x}, t)$ the number of charged particles $N(t)$ has to be included instead of the single particle q . The charge $N(t)$ will change with the development of the shower, i.e. with time. With the time-derivative of $\vec{A}(\vec{x}, t)$, hence, an additional radiation term will contribute to the electric field $\vec{E}(\vec{x}, t)$. This represents the same situation as given in an air shower where the number of the radiating charged particles $N(t)$ depends on the time and not only one charged particle radiates.

For a long time, it was not clear in which way the models missing this contribution can be corrected. In the scope of this work, we developed a method to include the missing radiation contributions and implemented it in REAS3. In this

method, the endpoint formalism, the radiation is associated with the “endpoints” of the individual particle trajectories. In chapter 4, the implementation of the endpoint formalism is discussed in detail and the impact of this missing radiation contribution on the resulting emission predictions is discussed.

REAS3: Modelling radio emission from cosmic ray air showers using an endpoint formalism

As already discussed in chapter 3, in recent years, various approaches for modelling radio emission from air showers have been developed. Since the predictions of the models differed it became obvious that at least some of the models were not complete. This was the case for REAS2 as well and is discussed in detail in section 3.2. With the endpoint formalism, the complete radio emission from air showers can be calculated in a canonical way. The implementation of the missing emission contributions using the endpoint formalism is presented in detail in the following sections and led to a publication (Ludwig and Huege, 2010b). In section 4.5, the results obtained with REAS3 in comparison to REAS2 are then discussed.

For the comparison of REAS2 and REAS3, the refractive index is set to unity and therefore not included in the formulas, since in REAS2 the refractive index was set to 1 as well. This allows a reasonable comparison. The inclusion of the refractive index and the changes on the results are discussed at the end of this chapter (see section 4.6).

4.1

Simulation algorithm of REAS

From REAS2 to REAS3, the simulation algorithm is unchanged and the air shower information is provided by CORSIKA and COAST in the same way as before. Therefore, in this chapter only a short overview of the technical implementation is given. More details on this topic can be found in Huege et al. (2007).

First, the shower is simulated with CORSIKA using the air shower parameters

of interest (such as primary energy, magnetic field, mass of primary, incoming direction, etc.). Using COAST, the information of the electrons and positrons is saved in histograms. These histograms contain information about the atmospheric depth of the particle, the particle arrival time, the lateral distance of the particle from the shower axis, the particle energy and the particle momentum direction. In the next step, REAS is generating individual electrons and positrons randomly according to the histogrammed distributions. These particles are then tracked analytically in the geomagnetic field. Note that the trajectories of the REAS simulation do not represent real trajectories of particles, i.e. one long particle trajectory is represented by an ensemble of several shorter, unrelated trajectories in the code. The length of the trajectories is determined by a parameter λ which is explained in section 4.4.

4.2 Contributions due to charge variation

In REAS2 (Huege et al., 2007), the radiation of single particles of an air shower is calculated as

$$\vec{E}(\vec{x}, t) = e \left[\frac{\vec{r} - \vec{\beta}}{\gamma^2(1 - \vec{\beta} \cdot \vec{r})^3 R^2} \right]_{\text{ret}} + \frac{q}{c} \left[\frac{\vec{r} \times [(\vec{r} - \vec{\beta}) \times \dot{\vec{\beta}}]}{(1 - \vec{\beta} \cdot \vec{r})^3 R} \right]_{\text{ret}}, \quad (4.1)$$

where $q = \pm e$ indicates the particle charge, $\vec{\beta} = \vec{v}(t)/c$ is given by the particle velocity, $R(t) = |\vec{R}(t)|$ describes the vector between particle and observer position, $\vec{r}(t) = \vec{R}(t)/R(t)$ is the line-of-sight direction between particle and observer, and γ is the Lorentz factor of the particle. The index “ret” means that the equation needs to be evaluated in retarded time.

The electrons and positrons emit radiation continuously along their track. To get a consistent description of radio emission in air showers, however, not only contributions due to the deflection of the particles in the magnetic field have to be taken into account, but also contributions due to the variation of the number of charged particles as discussed in section 3.2.

REAS2 treats radiation processes only along the trajectories, but not at the end or the beginning of trajectories. Strictly speaking, this is equivalent to the situation that the particle arrives with the velocity $v \approx c$ given by CORSIKA, enters the Earth’s magnetic field where it is deflected and describes a short curved track and finally flies out of the influence of the magnetic field still with a velocity $v \approx c$. Figure 4.1 shows a sketch for such a particle trajectory (lhs). It is obvious that this is not describing the real situation in an air shower. Consequently, to complement the description in the Monte Carlo code, radiation at the beginning and at the end of each particle trajectory has to be calculated. If at a given atmospheric depth more particle trajectories start than end, i.e. the number of



Figure 4.1: Sketch of the trajectory of an electron. Left: how it was implemented in REAS2. Right: with start- and end-point as needed for a consistent description of radio emission from EAS.

charged particles grows, this results in a net contribution. The same is true if the number of charged particles declines, i.e. more particle tracks end than start. Note that a net contribution occurs as well due to the change of the geometrical distribution caused by the spatial separation of the charged particles.

In REAS3, a particle is treated as if it was created at rest and became “instantaneously” accelerated to $v \approx c$, flew on a short curved track through the Earth’s magnetic field and got decelerated to rest again (see rhs of Figure 4.1). The acceleration process at the injection as well as the removal of an electron or positron takes place on time scales short in comparison with the frequencies of interest ($\nu_{\text{observed}} \leq 100 - 1000 \text{ MHz}$), i.e. $\delta t \ll \frac{1}{\nu_{\text{observed}}}$. Hence, only the time-averaged process is of interest, which will give a discrete contribution in contrast to the continuous emission along the curved particle trajectory. To calculate contributions for the start-point, the far field term of the general radiation equation is considered and it is integrated over the injection time δt . The “static” term of the radiation formula (Eq. 4.1), the velocity field, can be neglected, because the “radiation” term completely dominates the signal for distances R relevant in practical applications. The relation for the retarded time used for transforming the integral from dt to dt' is derived from $t' = t - R(t')/c$. With $dt = (1 - \vec{\beta} \cdot \vec{r})dt'$ the integral is solved as shown in the following calculation:

$$\begin{aligned}
 \int \vec{E}(\vec{x}, t) dt &= \frac{e}{c} \int_{t_0}^{t_1} \left. \frac{\vec{r} \times [(\vec{r} - \vec{\beta}) \times \dot{\vec{\beta}}]}{(1 - \vec{\beta} \cdot \vec{r})^3 R} \right|_{\text{ret}} dt = \frac{e}{cR} \int_{t'_0}^{t'_1} \frac{\vec{r} \times [(\vec{r} - \vec{\beta}) \times \dot{\vec{\beta}}]}{(1 - \vec{\beta} \cdot \vec{r})^2} dt' \\
 &= \frac{e}{cR} \int_{t'_0}^{t'_1} \frac{d}{dt} \left(\frac{\vec{r} \times (\vec{r} \times \vec{\beta})}{(1 - \vec{\beta} \cdot \vec{r})} \right) dt' = \frac{e}{cR} \left[1 \cdot \frac{\vec{r} \times (\vec{r} \times \vec{\beta})}{(1 - \vec{\beta} \cdot \vec{r})} \right]_{t'_0}^{t'_1} - \frac{e}{cR} \int_{t'_0}^{t'_1} 0 dt' \\
 &= \frac{e}{cR} \left(\frac{\vec{r} \times (\vec{r} \times \vec{\beta})}{(1 - \vec{\beta} \cdot \vec{r})} \right) \quad (4.2)
 \end{aligned}$$

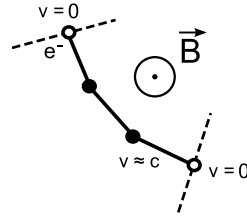


Figure 4.2: Sketch of the trajectory with a discrete description and endpoints.

Likewise, one gains the electric field for the end-point of the trajectory:

$$\int \vec{E}(\vec{x}, t) dt = -\frac{e}{cR} \left(\frac{\vec{r} \times (\vec{r} \times \vec{\beta})}{(1 - \vec{\beta} \cdot \vec{r})} \right) \quad (4.3)$$

It is important to first transform the integration time into retarded time before calculating the integral. The electric fields of the endpoints¹ and of the radiation along the track then have to be added to get a self-consistent implementation for modelling radio emission in an air shower.

4.3 Continuous vs. discrete calculation and incorporation of endpoint contributions

Adding the discrete endpoint contributions to the continuous contributions along the tracks may produce problems. The radiation associated with the end-points does not only contain the emission due to the tangential acceleration. Due to the change in the direction of particle movement between the beginning and the end of the trajectory, radiation associated with the perpendicular acceleration, which was so far treated in the continuous description, is also contained. Combining the two descriptions therefore exhibits a risk of double-counting. In order to avoid such problems, it is preferable to change the calculation for the continuous contributions along the curved particle tracks to a discrete representation. Hence, the chosen representation in REAS3 is completely discrete to ensure that the calculations are self-consistent.

To describe radio emission contributions along the particle trajectories in a discrete picture, the trajectories of the particles are split in straight track fragments joined by “kinks” in which the velocity of the particles is changing instantaneously. A sketch of this description is given in figure 4.2. The instantaneous change of

¹In the following the term “end-points” is used as a general term for both, start-points and end-points, as both are treated in the exact same way.

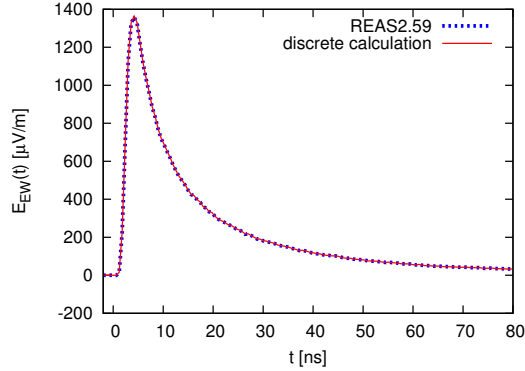


Figure 4.3: Comparison of discrete and continuous description of radio emission (without endpoint contributions) for an observer 100 m north of shower core of a vertical 10^{17} eV air shower. The results are identical.

velocity at the kinks leads to radiation. With particle velocity $\vec{\beta}_1 \cdot c$ before and $\vec{\beta}_2 \cdot c$ after the kink, radiation for one kink of the trajectory is:

$$\begin{aligned} \int \vec{E}(\vec{x}, t) dt &= \int_{t_1}^{t_2} \frac{e}{c} \left| \frac{\vec{r} \times [(\vec{r} - \vec{\beta}) \times \dot{\vec{\beta}}]}{(1 - \vec{\beta} \cdot \vec{r})^3 R} \right|_{ret} dt = \vec{F}(t_2) - \vec{F}(t_1) \\ &= \frac{e}{cR} \left(\frac{\vec{r} \times (\vec{r} \times \vec{\beta}_2)}{(1 - \vec{\beta}_2 \vec{r})} \right) - \frac{e}{cR} \left(\frac{\vec{r} \times (\vec{r} \times \vec{\beta}_1)}{(1 - \vec{\beta}_1 \vec{r})} \right) \end{aligned} \quad (4.4)$$

To verify that the continuous and the discrete calculations of emission contributions along the trajectories are equivalent and that both descriptions produce the same results, the REAS2 code was changed to calculate emission using the discrete approach of straight track segments connected with kinks (without the additional contributions of end-points). Analytically, the equivalence of the two approaches for the frequency domain has been shown by Konstantinov et al. (Konstantinov, 2009).

Several tests with the REAS code have confirmed that the implementation of the discrete description is equivalent to the continuous one as can be seen in figure 4.3. The figure illustrates the equivalence for a vertical proton-induced air shower with primary energy of $E_p = 10^{17}$ eV. The observer position is 100 m north of the shower core. The advantage of the discrete calculation is the consistency of the description of emission contributions along the tracks and emission at the endpoints which is making the incorporation of radiation at the endpoints canonical. To complement the former implementation in the Monte Carlo code with the emission due to the variation of the number of charged particles, it is therefore convenient to use the discrete description. In the discrete picture, contributions

at the beginning and the end of a track are just kinks with $\vec{\beta}_1 = 0$ and $\vec{\beta}_2 = 0$, respectively. This self-consistent emission model has been incorporated in REAS3, taking into account the radiation at the beginning and the end of a trajectory as well as along the curved trajectory. The obtained results for the radio signal are discussed in section 4.5, but first the numerical stability will be demonstrated.

4.4

Numerical stability

As already mentioned in chapter 4.1, particle trajectories are represented by ensembles of several shorter, unrelated trajectories in the code. This ensures that the phase-space distribution of the analytically propagated particles stays consistent with the underlying particle distribution without having to treat energy losses during the propagation explicitly (cf. section 4 of Huege et al. (2007)).

The length of the short segments is controlled by a parameter λ . This parameter λ determines the length of the short tracks into which the real trajectories of the particles are divided (it does not denote the sampling density of kinks on a track). If λ is chosen inadequately large, the discrepancies between the particle distributions recreated in REAS and the distributions histogrammed in CORSIKA are getting too large. Thus, to avoid these discrepancies λ has to be chosen small enough.

In REAS2, it was recommended to set this parameter to $1 \frac{\text{g}}{\text{cm}^2}$, even though it is just a technical parameter, i.e. the result does not depend on the exact value of λ as long as λ is set small enough. Also, in REAS3 the track length of the single short trajectories should have no influence on the physics results as long as it is chosen small enough. This cross check was made for a vertical proton-induced air shower with $E_p = 10^{17}$ eV. As shown in figure 4.4 for an observer 100 m north of the shower core, the result converges with decreasing values of λ . The same result is obtained for an observer 400 m north of the shower core which is displayed in the right column of figure 4.4. The comparison of both observer positions demonstrates that far away from the shower core, the result converges faster than close to the shower core. For $\lambda = 0.1 \frac{\text{g}}{\text{cm}^2}$, a stable result is obtained in both cases.

For observer positions close to the shower core, as for 100 m distance, it is also visible that for larger values of λ , e.g. for $\lambda = 1.0 \frac{\text{g}}{\text{cm}^2}$, there is already a finite radio contribution for negative times. These non-physical contributions appear if particles are created with symmetric trajectories around the place of particle generation and λ is chosen inadequately large. For small enough values of λ , however, the symmetric trajectories ensure a faster convergence of the result than the asymmetric trajectories used in REAS2.

With smaller parameters of λ , however, the high frequency noise increases as well as the computing time. This first effect is larger for observers far away as can

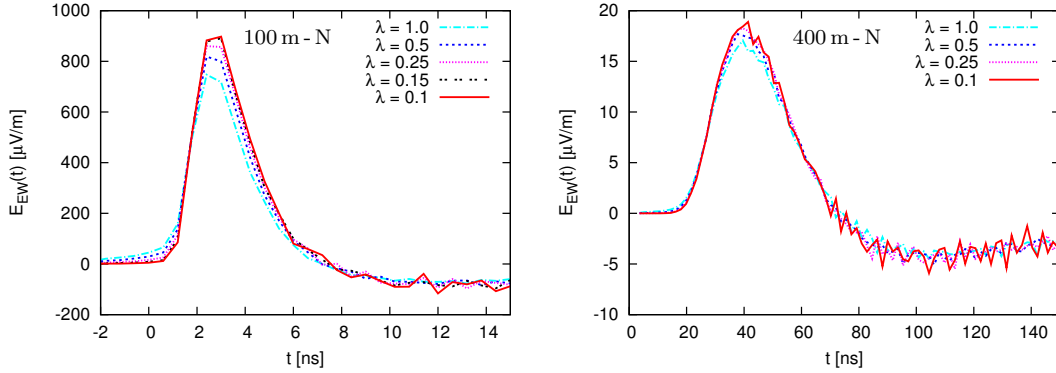


Figure 4.4: Influence of different values of the technical parameter λ . Left: observer 100 m north of shower core. Right: observer 400 m north of shower core.

be seen in figure 4.4. To optimize the calculation in REAS3, the path depth λ of the electron and positron trajectories is therefore chosen as a dynamical parameter depending on the lateral distance of the observer. Therefore, it is recommended to set λ to $0.1 \frac{\text{g}}{\text{cm}^2}$ at the core and increase this value linearly every 100 m as it is done by default in REAS3. The advantage of this implementation is on the one hand to gain stable results for all observers and on the other hand to avoid high frequency noise for observers at larger lateral distances. The difference in the recommended value of λ in REAS2 and REAS3 is due to the fact that the emission model in REAS3 requires a precise description of the particle momenta during the propagation, which requires a more fine-grained treatment.

4.5

Results of REAS3

In chapter 4.4, it was verified that REAS3 is producing stable results and that the endpoints were implemented correctly. In section 4.5.1, we focus on the results obtained with REAS3 and in section 4.5.2 the influence of the charge excess in air showers on the radio emission is discussed. In both, the radio emission was calculated for a proton-induced vertical air shower with primary energy of $E_p = 10^{17} \text{eV}$. The shower itself was generated with CORSIKA 6.7 and COAST. The positions of the observers were chosen at sea level with different lateral distances and relative observer orientations to the shower core. For the simulations with REAS2 and REAS3, identical showers were taken. This is easily possible because the histogramming approach allows an easy separation between the air shower modelling and the radio emission calculation.

4.5.1

REAS2 vs. REAS3

To study the changes introduced by the implementation of emission due to the variation of the number of charged particles, a simple, vertical shower geometry was chosen as specified above. The magnetic field was taken as horizontal with a field strength of 0.23 Gauss to get a geomagnetic angle of 90° . Figure 4.5 shows a comparison between unfiltered (i.e. unlimited bandwidth) pulses and frequency spectra of REAS2 and REAS3 for observers with different positions with respect to the shower core. The spectra show the total field strength for two azimuthal observer directions: the thick line displays the absolute field strength for an observer east of the shower core and the thin line for an observer north of the shower core.

It is clear that the strength of the pulses as well as the time structure of the pulses have changed, while the changes in the pulse amplitudes are dependent on the observer azimuth angle. The time structure of the pulses has changed from unipolar to bipolar. This can also be seen in the frequency spectra (lowest row of figure 4.5) where in case of REAS3, the spectral field strengths drop to zero for frequency zero, as it was the case in the analytical implementation (Huege and Falcke, 2003). It can be argued from basic physical arguments that the spectral field strength has to drop to zero for small frequencies because the source of the coherent emission exists only for a finite time in a finite region of space and thus the zero-frequency component of the emission, which corresponds to an infinite time-scale, can contain no power (cf. Scholten and Werner (2009)).

While the emission pattern of REAS2 was azimuthally asymmetric, REAS3 simulations are much more symmetric, as is expected for the given shower geometry. The increased symmetry can also be seen in the frequency spectra where the characteristics of the spectral field strengths with frequency are getting very similar for the two different azimuthal observer positions in case of REAS3. The remaining asymmetry will be discussed in section 4.5.2.

To get a more general impression of the changes in the amplitudes of the signal with REAS3, the lateral dependence of the emission is studied. Figure 4.6 shows this dependence for the unfiltered, full bandwidth amplitudes. In REAS2, there was a much stronger signal for observers in the north or south than for observers in the east or west. In REAS3, the signal pattern is much more symmetric, but observers in the eastern direction measure a higher absolute field strength and observers in the west see a lower field strength than observers with other azimuthal positions. In general, the amplitudes of the field strength got lower from REAS2 to REAS3, while the changes for observers north and south of the shower core are much larger than for observers in the east or the west.

To compare simulations with experimental data (e.g. of LOPES), the REAS simulations have to be filtered to a finite observing bandwidth. This is done by the helper application REASPlot which is included in the REAS3 package. In this

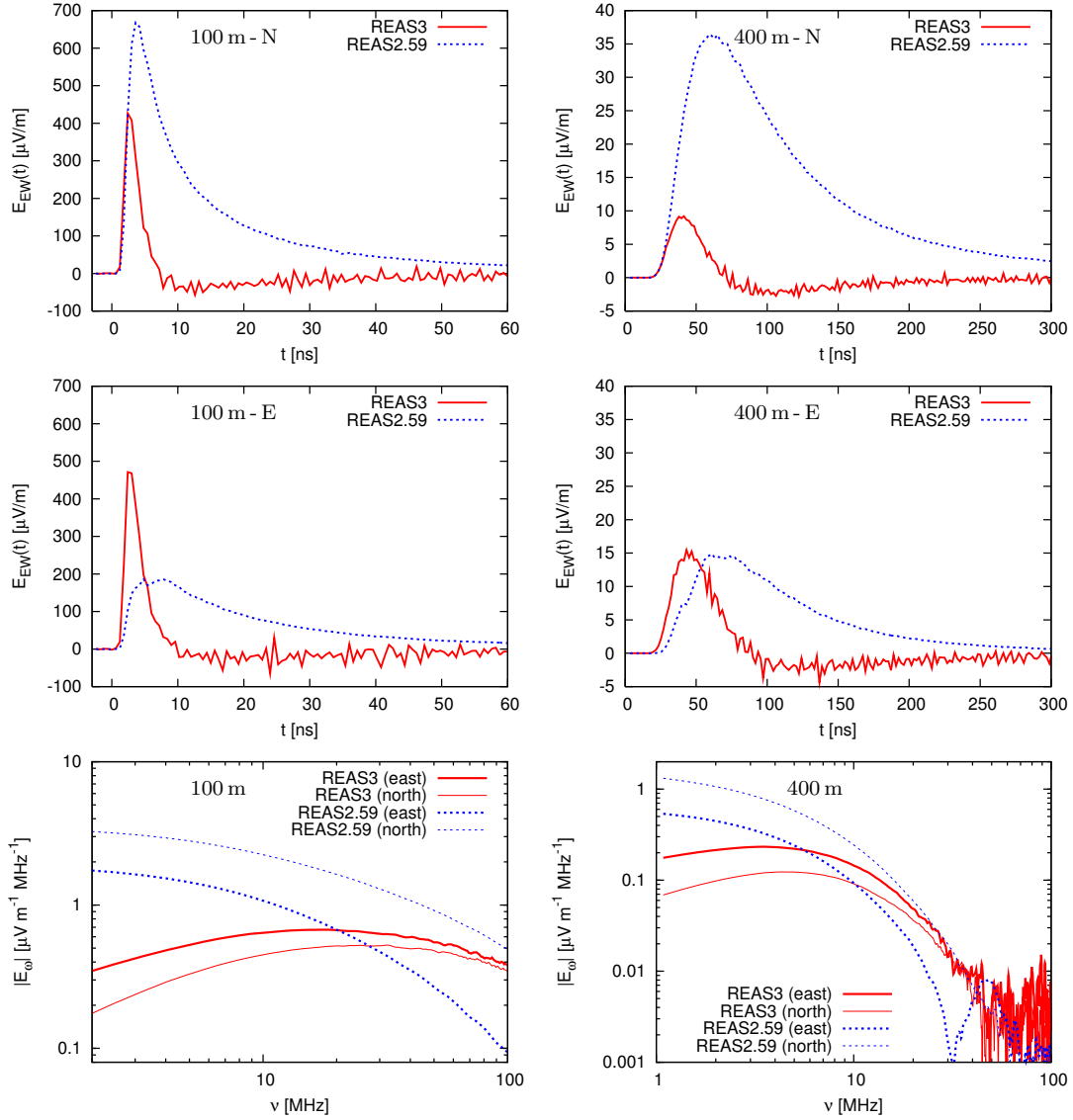


Figure 4.5: Upper row: raw pulses for observers 100 m (left) and 400 m (right) north of shower core. Middle row: raw pulses for observers 100 m (left) and 400 m (right) east of shower core. Lowest row: frequency spectra for observers 100 m (left) and 400 m (right) east and north of shower core. For the raw pulses the east-west polarisation of the electric field is shown, whereas for the frequency spectra the total spectral field is shown.

paper, REASPlot was used with an idealised rectangular 43 MHz-76 MHz band-pass filter which can lead to acausal contributions at negative times due to the idealisation of the filter. In figure 4.7, the filtered pulses for observers with lateral distance of 100 m east and north of the shower core are shown. The quick oscilla-

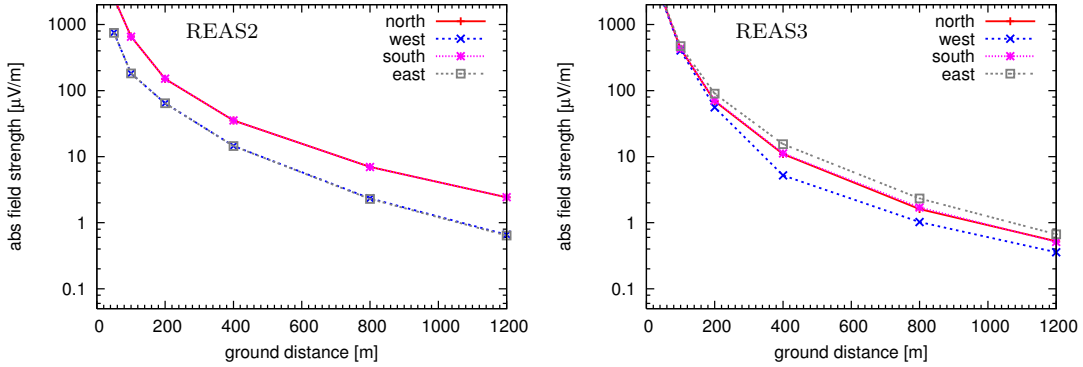


Figure 4.6: Lateral dependence with full bandwidth amplitudes. Left: REAS2. Right: REAS3.

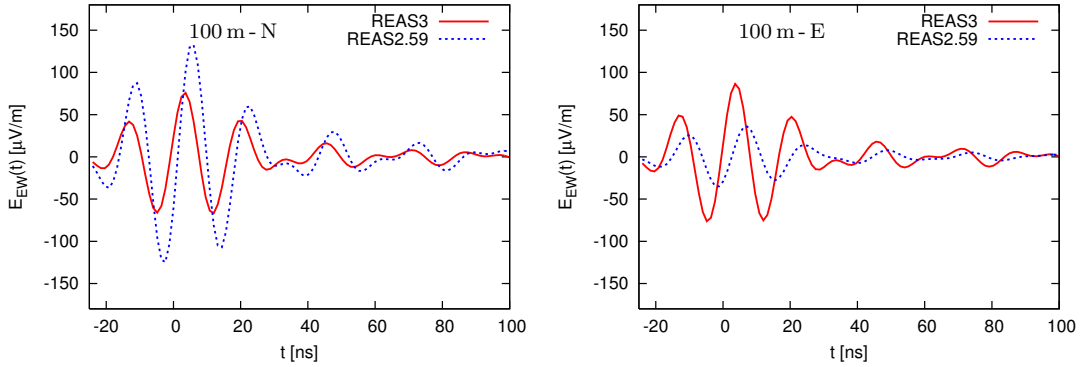


Figure 4.7: Filtered pulses (a simple rectangular 43-76 MHz bandpass filter is used) for observers with 100 m distance to the shower core. Left: the observer is north of the shower core. Right: the observer is east of the shower core.

tions are determined by the selected filter bandwidth. The differences in the pulse strengths are much smaller for the filtered than for the raw pulses because the strongest changes between REAS2 and REAS3 occur at low frequencies. (Please note that figure 4.5 is plotted on a log-log scale.) In general, e.g. for different geometries, the differences in the amplitudes of the filtered pulses can be larger than in this example (cf. Ludwig and Huege (2010a)).

Again, the increased azimuthal symmetry of REAS3 is observable. To get an overall impression of the change from REAS2 to REAS3 and the influence of the net charge excess on the east-west asymmetry, the contour plots of the 60 MHz field strength are shown in figure 4.8. The ellipticity which is seen in REAS2 is replaced by a nearly azimuthally symmetric pattern in REAS3. The “clover” pattern seen earlier in the north-south polarisation component is no

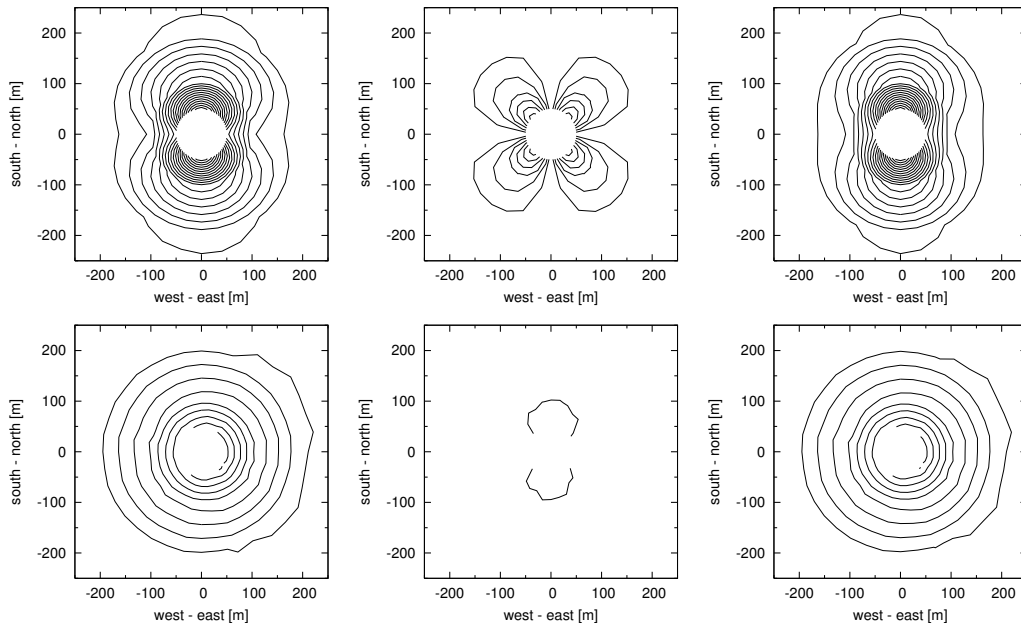


Figure 4.8: Contour plots of the 60 MHz field strength for emission from a 10^{17} eV vertical air shower. From left to right: total field strength, north-south and east-west polarisation component. Contour levels are $0.1 \mu\text{Vm}^{-1}\text{MHz}^{-1}$ apart. The closest position of the simulated observers to the shower core is 50 m. Upper row: REAS2. Lower row: REAS3

longer existing. In the vertical polarisation component (not shown here), there is no significant flux for either of the two simulations, as expected for a vertical shower. In the contour plots of REAS3, the east-west asymmetry is visible as well.

The resulting REAS3 emission pattern can be interpreted as a superposition of a circularly symmetric contribution with a $\vec{v} \times \vec{B}$ (in this case thus pure east-west) polarisation and a radially polarised emission contribution caused by the time-varying net charge excess.

In summary, the incorporation of radiation due to the variation of the number of charged particles in the form of endpoint contributions results in a clear change from REAS2 to REAS3. The revised, self-consistent implemented model in the Monte Carlo code REAS3 predicts bipolar pulses with a mostly symmetrical emission footprint. In addition to these changes, a further emission contribution arises from the variation of the net charge excess, which explains the remaining asymmetries. This contribution will be discussed in the following section.

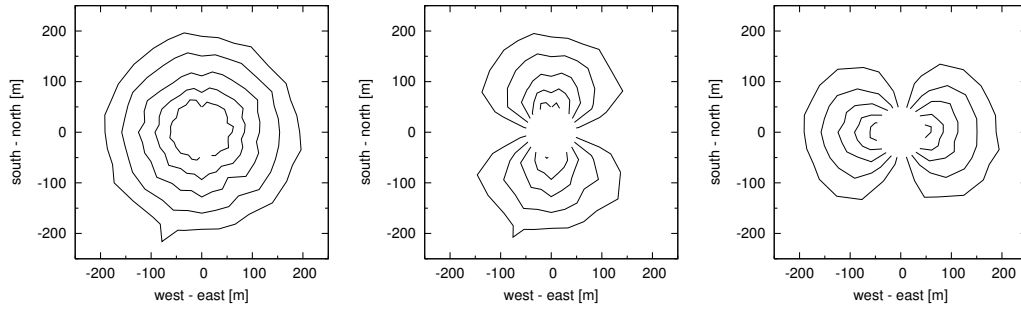


Figure 4.9: Contour plots of the 60 MHz field strength for emission from a 10^{17} eV vertical air shower without any magnetic field. Contour levels are $0.03 \mu\text{Vm}^{-1}\text{MHz}^{-1}$ apart. The closest observer position to the shower core is 50 m. From left to right: total field strength, north-south and east-west polarisation component. The “spike” in the lower-left part of the contours is associated with noise in the simulation.

4.5.2

Discussion of charge excess emission

The observed east-west asymmetry mentioned in section 4.5.1 arises from the fact that more electrons than positrons exist in an extensive air shower (Bergmann et al., 2007). This net charge excess of order 10-20% leads to a contribution in the radio signal even in the absence of any magnetic field. Hence, in this section an air shower was simulated with CORSIKA for the geometry and primary characteristics as already mentioned at the beginning of this chapter, but in contrast to section 4.5.1, the magnetic field strength was set to 0. Although the showers calculated with $B = 0.23$ Gauss and $B = 0$ do not represent the exact same particle distributions, the predictions for the shower with $B = 0$ can be interpreted as the contribution due to the net charge excess of the shower used in section 4.5.1. This allows us to test whether indeed the east-west asymmetry can be associated with the pure charge excess.

In REAS2, radio emission is produced due to deflection of charged particles in the magnetic field. Hence, there is no radiation without magnetic field. In contrast, REAS3 takes also emission due to the variation of the net charge excess into account. A radially polarised component for emission due to charge excess is expected, as seen also in the macroscopic approach (Werner and Scholten, 2008). The radiation pattern for a shower with $B = 0$ Gauss is indeed radially polarised as illustrated in the contour plots of the 60 MHz field strength in figure 4.9. For the vertical component (not shown here) there is again no significant flux, as expected. Again, the closest observer position to the shower core is 50 m. Please note that the contour levels for the simulation without magnetic field are smaller than for the simulation with magnetic field, i.e., the relative field strength of the charge excess emission at 60 MHz is small in the distance range up to 200 m.

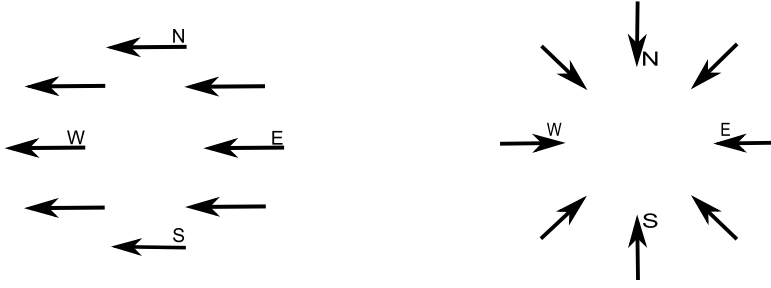


Figure 4.10: Sketch of the polarisation vector. Left: uniform pattern as it is the case for pure geomagnetic emission. Right: radial pattern as it is the case for the net charge excess emission.

To study the influence of the net charge excess emission on the overall radio signal, it is helpful to look at the polarisation vectors in the plane perpendicular to the shower axis. For the pure geomagnetic emission, the polarisation vectors at all observer positions point in the same direction as illustrated in the left sketch of figure 4.10. The right sketch illustrates the polarisation vector for the emission due to the variation of the net charge excess. The direction in which the vector points is changing with the observer position, following a radial pattern. Hence, for an observer in the east the total signal S_E is given by

$$S_E = S_{gm} + S_{ce} \quad (4.5)$$

where S_{gm} is the pure geomagnetic contribution and S_{ce} the net charge excess contribution to the signal. For an observer in the west, the total signal S_W is composed of

$$S_W = S_{gm} - S_{ce} \quad (4.6)$$

With the signals measured east and west from the shower axis, the signal for the pure geomagnetic emission and for the net charge excess can be calculated by

$$S_{gm} = \frac{1}{2}(S_E + S_W) \quad \text{and} \quad S_{ce} = \frac{1}{2}(S_E - S_W). \quad (4.7)$$

To verify the assumption made in equations (4.5) and (4.6), the signal of the charge excess as it is resulting from above was calculated for the shower with $B = 0.23$ Gauss and was compared with the emission of the shower with $B = 0$. Figure 4.11 illustrates that both pulses match. Therefore, the east-west asymmetry in the azimuthal emission pattern seen in the figures of section 4.5.1 is completely reducible to the emission of the net charge excess in an air shower.

Finally, it is interesting to quantify the relative strength of the charge excess emission with respect to the pure geomagnetic radio emission. Analyses studying

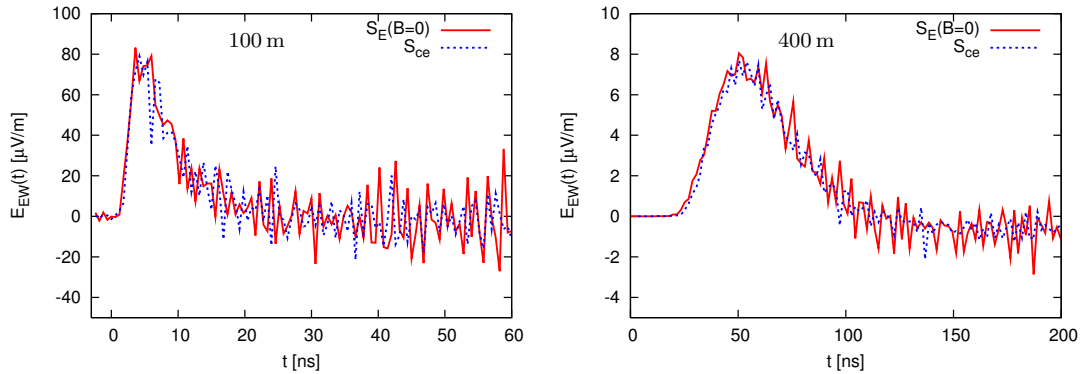


Figure 4.11: Comparison of emission due to net charge excess without magnetic field (solid line) and the calculated signal for the net charge excess (dashed line) from a shower with magnetic field. Displayed is in each case the east-west polarisation. Left: 100 m distance from shower core. Right: 400 m from shower core.

the dependence of the radio signal on pure geomagnetic emission have already been done and have shown that there might be discrepancies between a pure geomagnetic model and the measured data (Isar et al., 2009). The ratio of the net charge excess signal and the pure geomagnetic radiation can be calculated from equation (4.7) to quantify the relative influence of the net charge excess. Figure 4.12 illustrates the ratio for the unfiltered full bandwidth amplitudes and the 43 to 76 MHz filtered bandwidth amplitudes for the east-west polarisation component. For the filtered case the ratio in the plot is shown only for observers up to 400 m lateral distance. The reason is that the frequency spectra for a vertical shower drop fast with increasing lateral distance as was also seen in figure 4.5. Consequently, in the used frequency range the signal is not any more distinguishable from numerical noise at very large distances. For the amplitudes of the unfiltered pulses the charge excess has more and more influence with larger distances, from a few % close to the core to around 90% of the pure geomagnetic emission at 1200 m. However, for the filtered pulses the ratio is almost constant over the whole range, at a level of $\sim 10\%$. It is important to clarify that the emission of the net charge excess occurs due to the variation of the number of charged particles and not due to Cherenkov-like emission. Both processes have been described in the pioneering articles of Askaryan (Askaryan, 1962, 1965), but the term “Askaryan radiation” is today generally interpreted as Cherenkov emission in dense media. For the inclusion of Cherenkov-like emission, a refractive index is needed which is not “unity”. Up to the next section, REAS3 approximated the index of refraction to be unity. In the last part of this chapter, the inclusion of the refractive index of the atmosphere in REAS3 is discussed and initial results

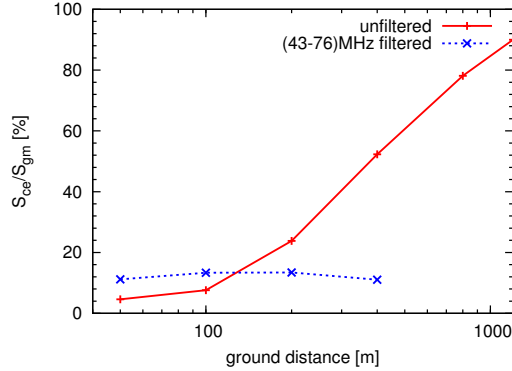


Figure 4.12: Comparison of the charge excess and the pure geomagnetic contribution on the radio signal of a vertical air shower for the east-west polarisation component. The lines may not represent the correct interpolation between the points due to the logarithmic scale of the x-axis. The ratio of the filtered data is only shown for distances up to 400 m, because at large distances the signal is not any more distinguishable from noise in this frequency band.

are shown.

4.6

Incorporation of the refractive index

To incorporate the refractive index of the atmosphere, two aspects have to be considered: First, the travel time of the emission from the source point to the observer increases. Second, the electric field amplitude arising due to the acceleration of the charged particles is influenced. Within the endpoint formalism, the refractive index n is implemented according to equation 4.2 as follows:

$$\begin{aligned} \int \vec{E}(\vec{x}, t) dt &= \frac{e}{c} \int_{t_0}^{t_1} \left| \frac{\vec{r} \times [(\vec{r} - n\vec{\beta}) \times \dot{\vec{\beta}}]}{(1 - n\vec{\beta} \cdot \vec{r})^3 R} \right|_{ret} dt \\ &= \pm \frac{e}{cR} \left(\frac{\vec{r} \times (\vec{r} \times \vec{\beta})}{(1 - n\vec{\beta} \cdot \vec{r})} \right) \end{aligned} \quad (4.8)$$

The + corresponds to a startpoint, the – corresponds to an endpoint. In principle, the implementation of a non-unity refractive index in REAS3 should be straightforward. However, it turned out that some algorithms used in REAS3 are not adequate for this situation, since discontinuities arise if the denominator gets zero for particles at the Cherenkov angle. Or, with other words, single particles make a high contribution when their direction to the observer lies on the Cherenkov cone. The answer to this problem is currently under investigation, but it has not been solved completely at the time of finishing the present work.

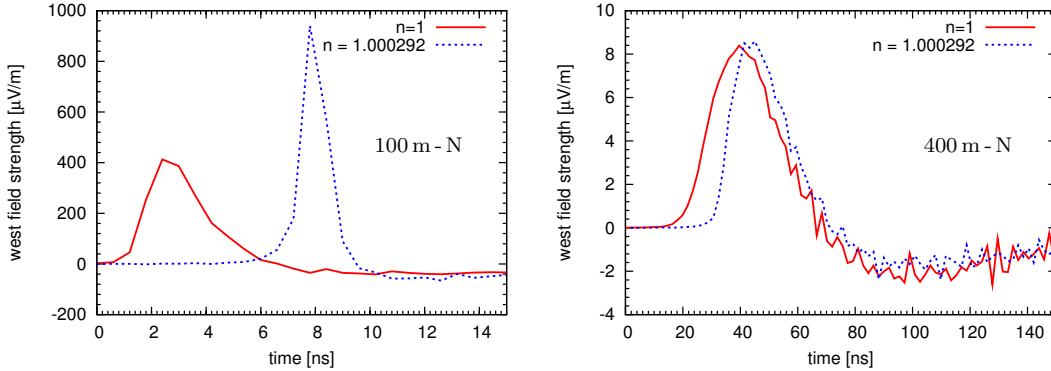


Figure 4.13: The blue pulse shows the influence of a constant refractive index for all altitudes of the atmosphere on the light-travel time of the signal for an observer at 100 m (lhs) and 400 m (rhs) north of shower core. The pulse is delayed and gets narrower but higher, since the radio emission from the air shower becomes more compact with a refractive index larger than 1.

However, the influence of the refractive index on the light-travel time was studied. For the present, the change of the amplitude is neglected but the increase of the travel time of the emission is considered. Therefore, the time t_{observer} at which the emission reaches the observer has to be calculated as the sum of the time of the emission t_{emission} plus the light travel time for the distance R between the source of the emission and the observer, i.e.

$$t_{\text{observer}} = t_{\text{emission}} + \frac{n \cdot R}{c} \quad (4.9)$$

As shown in figure 4.13 for observers 100 m and 400 m north of the shower core, already with a constant refractive index of the atmosphere of $n = 1.000292$, the pulse width gets smaller, the height larger and the pulse arrival time is delayed. The explanation of the general time-delay of the pulse is obvious. Due to a refractive index unequal to unity, the light-travel time is increasing for the emission propagating in the atmosphere. For observers further away from the shower core, the delay is getting less significant with respect to an observer close to the shower core. This is explainable, since the relative time-delay due to the increasing distance R has a larger impact than the absolute time-delay due to the refractive index n .

The change in the pulse shape is well-understood as well. With a refractive index of unity, the allocation of t_{observer} to t_{emission} is well-defined. With a constant refractive index, the emission from particles higher in the atmosphere is getting more delayed than the emission from particles lower in the atmosphere. This implies that emission from particles higher in the atmosphere can reach the

observer at the same time than the emission from particles lower in the atmosphere although the travelled distance is shorter. (Please note that the particles of the shower still travel with roughly the speed of light but the travel time of the emission is affected by the refractive index). With this, the emission from two different source points reaches the observer at the same time. Thus, the allocation of the emission and the observing time is not anymore well-defined. Hence, the air shower seems more compact and thus more localized in time and with this, the pulse is getting shorter in time. Again, the influence on the pulse shape is larger for small observer distances as discussed above.

It is obvious that the refractive index of the atmosphere has to be considered for future comparisons of data and simulations. Since the implementation is still under investigation, the refractive index of the atmosphere was set to unity for the further studies in the present work. Furthermore, the refractive index needs to be implemented as a function of atmospheric depth, since the density is changing with the altitude. The refractive index n at a given altitude h is characterised by the refractivity $\epsilon(h)$ of the atmosphere:

$$n(h) = 1.0 + \epsilon(h) = 1.0 + \frac{\epsilon_{\text{ground}}}{\rho_{\text{ground}}} \cdot \rho(h) \quad (4.10)$$

where ϵ_{ground} is the refractivity at ground, i.e., $n(0) - 1.0$, and $\rho(h)$ is the density of the atmosphere. Thus, with higher altitude and lower density of the atmosphere, the refractive index is getting smaller. In 8 km height, the refractive index of the atmosphere is roughly 1.00011 instead of 1.000292 on ground.

In summary, with the development and incorporation of the endpoint formalism large progress was achieved. We showed that REAS3 produces stable results and that the pulse shape changed from unipolar to bipolar which agrees with theoretical considerations. As we discussed in section 4.5.2, the charge excess contribution is automatically taken into account. To understand the emission and the pulse shape in detail, the relation of the pulse shape to shower characteristics will be studied in the following chapter.

CHAPTER 5

Details of the pulse shape

With REAS3, it is possible to study the radio pulse shapes and their relation to shower characteristics in detail. To achieve this, the particles of the air shower are categorized under several aspects, e.g. their energy or their atmospheric depth. For each category, its contribution to the complete radio signal is evaluated. Analysing the pulse shapes as done in the following sections helps to understand how the particles of the chosen categories contribute to the radio signal. This may also give hints to enhance the optimisation strategies of the REAS code.

A detailed study on the pulse shapes with REAS3 is possible, since REAS3 is using COAST (Lafèbre et al., 2009) histograms derived from CORSIKA (Heck et al., 1998) simulations. In the histograms, the information on the particle distributions is saved and can be tracked through the complete air shower. For the analysis presented in the following sections, particles of the air shower are selected which fulfill a given criterion, e.g. in section 5.1 the radio emission of particles in a specific energy range is calculated and compared with the emission of other energy ranges. Already with REAS2, the details of the pulse shape have been analysed (Huege et al., 2007) in a similar fashion. For comparability, the categories and regions of the air shower development were chosen equal to the ones chosen for the REAS2 analysis. The analysis on the pulse shape was done at sea level for a vertical air shower with primary energy of 10^{17} eV and a magnetic field corresponding to the one at the Pierre Auger Observatory.

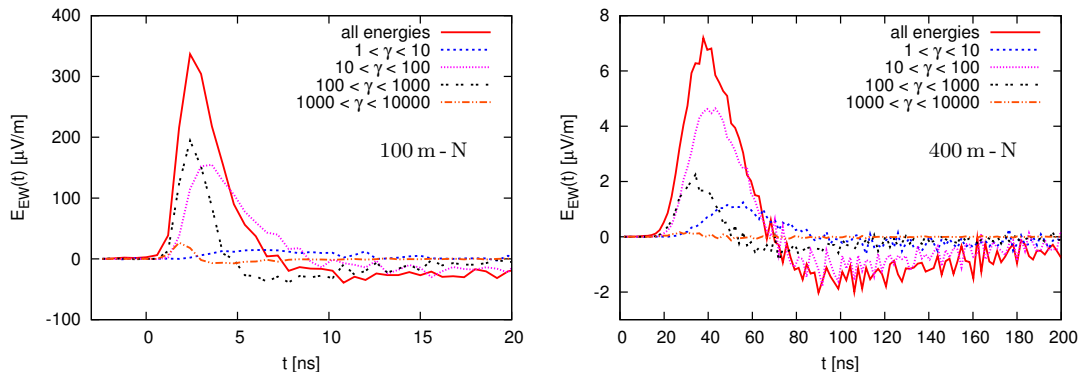


Figure 5.1: Contributions of different particle energy regimes to the east-west polarisation of the raw radio pulses for observers 100 m (lhs) and 400 m (rhs) north of the shower core.

5.1 Contribution of different particle energy regions

In this section, it is studied how particles with different energies contribute to the radio signal. Figure 5.1 shows the contributions of different particle energy regimes to the east-west polarisation where the radio pulse at 100 m north is on the left-hand side and at 400 m on the right-hand side. Close to the shower core, the particles with Lorentz factors between 10 and 100 dominate the radio signal. The particles with very small energies and Lorentz factors larger than 1000 contribute only little to the full radio signal. The particles with Lorentz factors between 10 and 100 and the particles with Lorentz factor between 100 and 1000 give roughly equal contributions to the overall radio pulse for the observer with 100 m distance. Although the particles with higher energies are fewer, the contribution is slightly larger, since beaming-effects lead to a more efficient radiation close to the shower core. Furthermore, close to the shower axis they are prominent.

However, this result is different from the one obtained with REAS2. With REAS2, the particles with a Lorentz factor between 100 and 1000 dominated strongly the signal at an observer distance of 75 m (cf. figure 24 in Huege et al. (2007)). This implies that the endpoints of the particle trajectories contribute more efficiently at lower energies and less beamed than the pure geosynchrotron contributions considered in REAS2.

Comparing this with the contributions to the radio pulse at 400 m (rhs of figure 5.1), it is evident that particles with lower energies dominate the signal at larger distances. The particles with very large Lorentz factors do not contribute distinctly to the radio signal at this distance as it was true for REAS2 as well. This behaviour confirms that beaming effects influence the radio emission from air showers. For both observers, it is obvious that particles with different en-

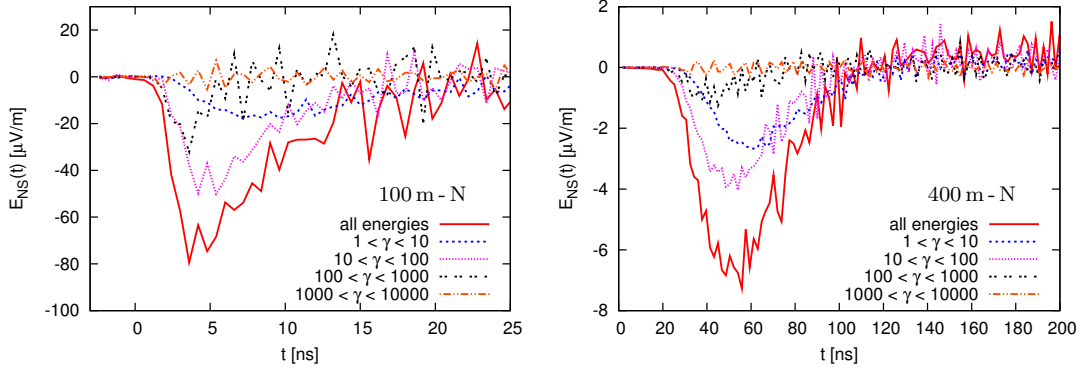


Figure 5.2: Contributions of different particle energy regimes to the north-south polarisation of the raw radio pulses for observers 100 m (lhs) and 400 m (rhs) north of the shower core.

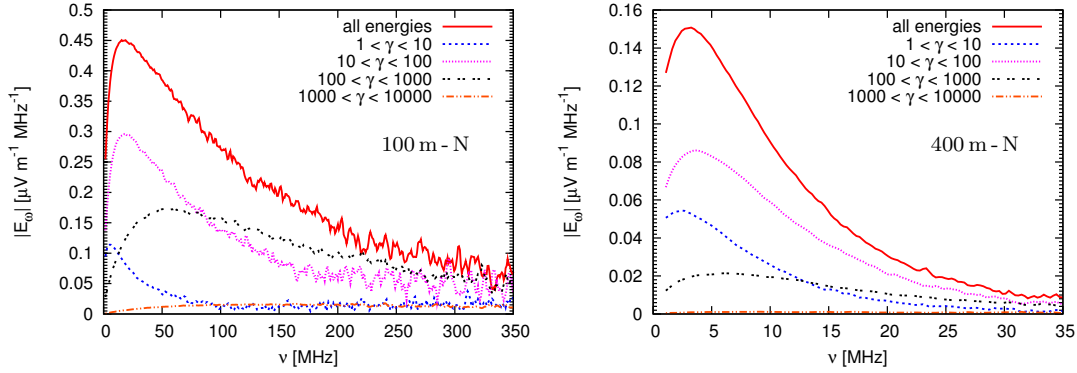


Figure 5.3: The frequency spectra of the contributions of different particle energy regimes for observers 100 m (lhs) and 400 m (rhs) north of the shower core. The spectra of the higher energetic particles are flatter, i.e. the particles are more localized.

ergies contribute at different times to the radio signal. The pulses for particles with higher energies have their maximum earlier than the pulses for low-energetic particles.

Figure 5.2 shows the contributions of different particle energy regimes to the north-south polarisation. (Please note the lower amplitudes for the observer at 100 m distance.) The radio pulse at 100 m north is on the left-hand side and at 400 m on the right-hand side. It is obvious that compared to the east-west polarisation, the lower energetic particles contribute more to the radio signal than high energetic particles. This is not surprising since the north-south polarised radio emission from a vertical air shower is arising purely from the charge excess

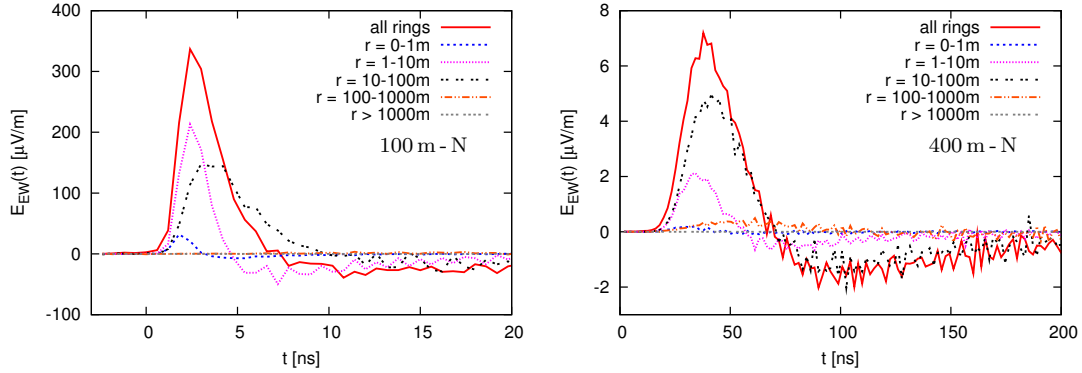


Figure 5.4: Contribution of different lateral rings to the east-west polarisation of the raw radio pulses for observers 100 m (lhs) and 400 m (rhs) north of the shower core.

in the air shower. The charge excess electrons mainly have lower energies because they originate from the atmosphere molecules from which they have been removed by ionisation and the corresponding positrons have been captured by negative charged ions in the atmosphere.

The frequency spectra shown in figure 5.3 confirm that the high energetic particles are distributed on a smaller space than the low energetic particles since for high energetic particles the spectra are flatter than for low energetic particles. If the source of the radiation is distributed more widely as in the case for particles with lower Lorentz factors, the minimum wavelength for coherent emission gets larger. Hence, the contributions to the signal dominate at smaller frequencies and the spectra are falling to higher frequencies. For particles distributed on smaller scales, the minimum wavelength for coherent emission gets smaller and thus, the frequency spectrum gets flatter. This is in agreement with the raw pulses of figure 5.1 where the pulses of the high energetic particles are shorter in time.

5.2

Contribution of different lateral distances

To compare the contribution of different lateral distance ranges, the air shower has been split in rings. Since the radio signal scales with geometrical lengths and not with the atmospheric matter traversed, these rings are defined by geometrical distances independent of the atmospheric depth (and with this the density). Otherwise, the rings would have been defined dependent on the Molière radius. The result of the separation in geometrical cylinders is shown in figure 5.4. For small lateral observer distances, the particles close to the shower core mainly determine the signal. Particles which have a lateral distance larger than 100 m do not contribute to the observed radio signal at 100 m on ground. At this observer distance,

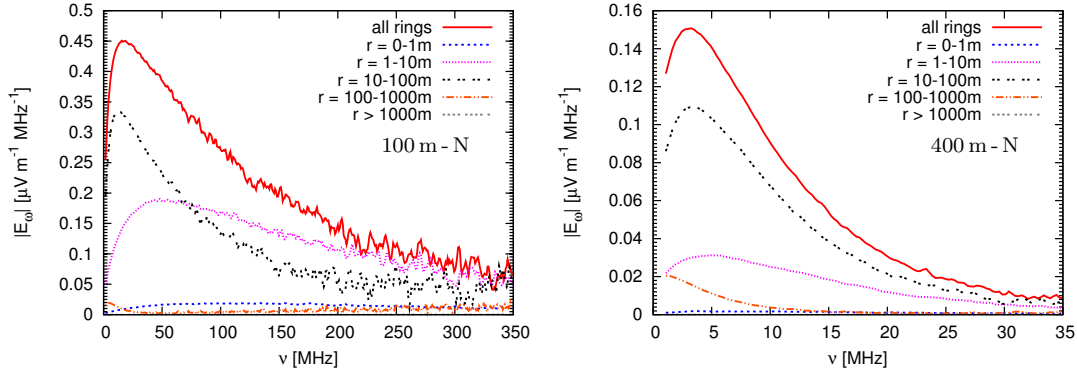


Figure 5.5: The frequency spectra of the contributions of different lateral rings for observers 100 m (lhs) and 400 m (rhs) north of the shower core. The spectra of the particles from the innerst rings are flatter, since they are all clustered around the shower core. With increasing lateral distance, the spectra becomes steeper due to the larger spread of the particles.

the strongest emission comes from particles between 1 m–10 m and 10 m–100 m. This is in agreement with the γ -distribution in the previous chapter, where the higher energetic particles dominate the radio signal close to the shower core and these particles are clustered close to the shower axis.

At an observer distance of 400 m, the radio signal is clearly dominated by the particles with a lateral distance of 10 m–100 m from the shower core. Only a small contribution is coming from the particles with lateral distances less than 10 m. The particles with distances larger than 100 m from the shower axis contribute very little to the radio signal at 400 m on ground. This is true for the observer at 100 m distance as well.

The pure charge excess signal in the north-south polarisation component behaves similarly to the east-west polarisation component and therefore is not shown here. The frequency spectra of the different lateral rings agree with the expectations as well. They are shown in figure 5.5. For the smallest lateral rings, the frequency spectra are flat as expected since the particles are clustered all close to the shower axis and the pulse in time is shorter compared to larger lateral rings (cf. figure 5.4). Comparing the results of this section with the previous results obtained with REAS2 (Huege et al., 2007), no major differences appear. This is well understood since the high energetic particles are clustered close to the shower axis and dominate the radio signal at small observer distances, while the signal at larger observer distances is dominated by the lower energetic particles from the cylinder with radius of 10 – 100 m.

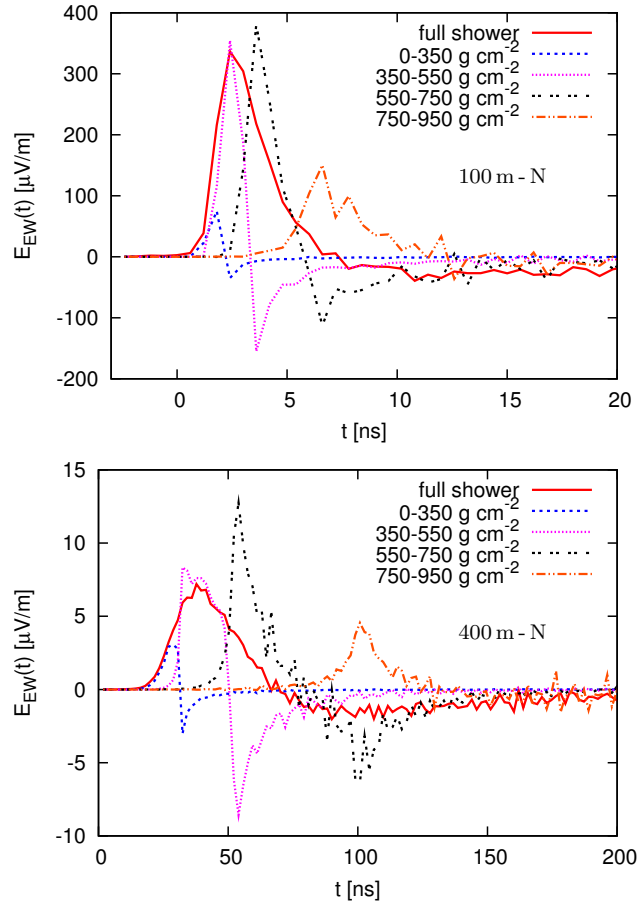


Figure 5.6: Contribution of different shower evolution stages to the east-west polarisation of the raw radio pulses for observers 100 m (top) and 400 m (bottom) north of the shower core.

5.3

Contribution of different shower phases

Not only the contributions of particles with a specific energy or lateral distance are of interest, but also the contributions of different evolution phases of the air shower. To investigate this, the air shower has been divided in segments of atmospheric depth. Figure 5.6 displays the results for four different segments.

At first glance, one may wonder that the pulses of the individual slices overlap with each other. This is mostly determined by the construction of the individual slices in the code. A particle is chosen randomly and the atmospheric depth is appointed. If the atmospheric depth has a value corresponding to the selected shower phase, the particle is followed for further calculations. In the following calculations, a longitudinal and a lateral displacement are added to the particle.

The longitudinal displacement of the particles is always to lower atmospheric depths and therefore, it causes a time delay for all observers on the ground. The more distant the observers are to the shower core, the larger is the time delay. With the lateral displacement added to the particle, the particle can be shifted closer to the observer or further away. According to the displacement, the observer detects the emitted radiation sooner or later. With these time delays, it can happen that the contribution of two different shower phases arrives at the observer at the same time. The spatial displacements affect the arrival times more strongly for observers further away from the shower core.

The bipolarity of the individual pulses is as well understood by the construction of the individual slices in the code. Since the particles are shifted along the shower axis after their classification into separate slices it happens that at the end of a layer, e.g. at $350 \frac{\text{g}}{\text{cm}^2}$, starting points of new particle tracks are missing because they are sorted in the layer which starts at $350 \frac{\text{g}}{\text{cm}^2}$. This is equivalent to a situation where the longitudinal shower profile grows, reaches a maximum and then declines towards zero towards the end of each layer.

The shower maximum of the extensive air shower considered in this section (and the previous and following sections) is at $689 \frac{\text{g}}{\text{cm}^2}$. Hence, the black curves represent the contributions of the slice including the shower maximum. For small observer distances, the radiation mainly comes from the regions around and before the shower maximum. For larger distances the region before the shower maximum dominates the signal, but the region around the shower maximum gives the largest positive contribution. This contribution is rather compensated by the radiation of the region before the shower maximum (magenta line at the top of figure 5.6).

With REAS2, very similar results were obtained (Huege et al., 2007). There, the emission was dominated by the shower phase around the shower maximum and the phase shortly before the shower maximum. Close to the shower core, the radiation of the different slices arrives nearly at the same time. With larger observer distances the arrival times get delayed due to geometrical effects. For smaller lateral distances, the geometrical time-delays are smaller. Considering a realistic refractive index in the atmosphere, the arrival times of the single pulses are expected to change at these distances and the radio pulse of the full shower will get narrower (cf. section 4.6).

Figure 5.7 shows the north-south polarisation of the different shower phases. In the first phase of the air shower, the charge excess is negligible and contributes only very little to the radio signal at observer positions far away from the shower core. For the observer at 100 m distance (top) the signal is dominated by the shower phase around the shower maximum and in contrast to the east-west polarised signal by the shower phase after the shower maximum. That is not surprising, since the fraction of the charge excess with respect to the total charge rises with the development of the air shower and thus contributes more strongly at the end of the shower. In figure 5.8, the fraction of the charge excess with

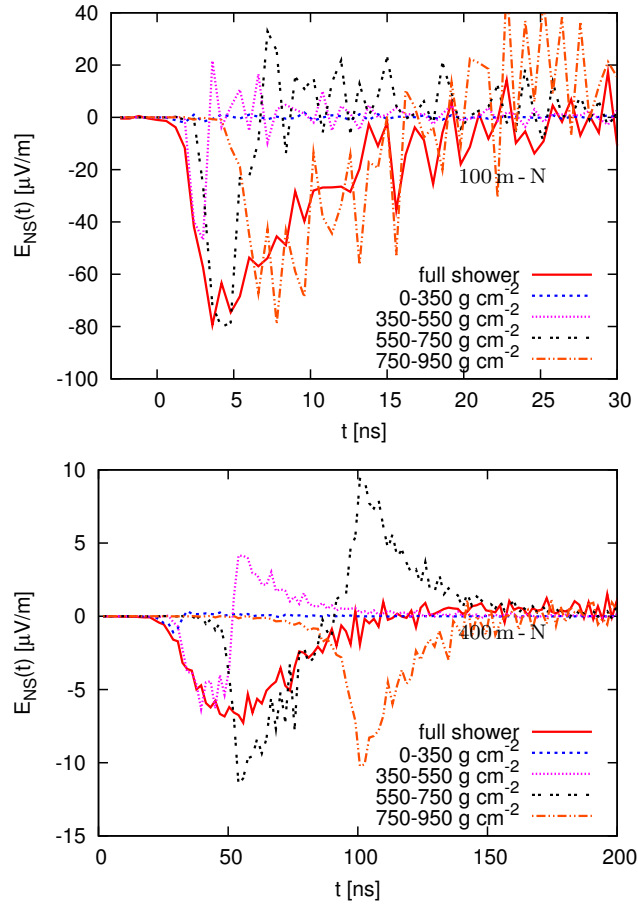


Figure 5.7: Contribution of different shower evolution stages to the north-south polarisation of the raw radio pulses for observers 100 m (top) and 400 m (bottom) north of the shower core. Please note that for the observer at 100 m, the scale on the y-axis differs from the scale for the east-west polarisation (fig. 5.6).

respect to the total number of electrons and positrons is shown for particles with energies larger than 400 keV. In the early phases of the air shower, around 16% more electrons than positrons exist. At the end of the shower, the charge excess is roughly 27%.

5.4 Contribution of different geometric heights

In conjunction with the previous section, it is interesting to look at the different regions of the air shower with respect to the geometrical height determining the radio physics instead of the atmospheric depth determining the air shower physics. To investigate this, the particles are equally chosen than in the previous

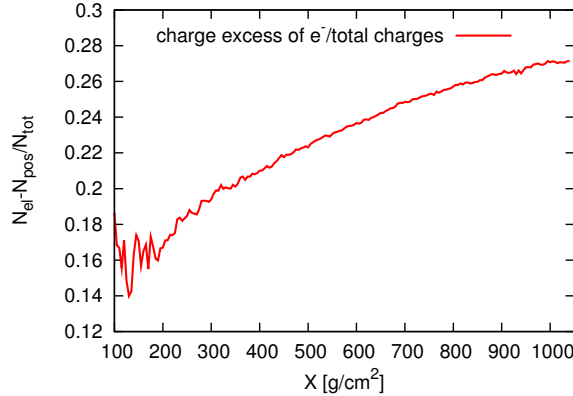


Figure 5.8: Shown is the fraction of the charge excess with respect to the total number of electrons and positrons with energies ≤ 400 keV as a function of atmospheric depth. With larger atmospheric depth, the fraction rises. The large fluctuations at the upper part of the atmosphere are due to the shower development. At this early phase only a few electrons and positrons are created and thus, single particles have a large impact on the calculated fraction.

section, while not the atmospheric depth is appointed but the height (in meters) above sea level. Figure 5.9 shows the contribution of the different heights above ground. Similar to the contributions of the atmospheric depths, the radio signals originating from the early phases (large heights) of the air shower arrives at first, then the others follow with decreasing height. The time-delay of the single pulses is larger for increasing observer distances as well. Again, the pulses have an overlap due to the construction of the slices in the code.

In contrast to the contributions of the different atmospheric depths, the maxima of the pulses from different geometrical heights are similar. This is consistent with the fact that geometrical scales determine the radio emission and not atmospheric scales. This is an important conclusion since it means that air shower physics can be decoupled from radio physics. For (air) shower physics the penetrated matter is crucial, e.g. for cross sections and interactions, whereas the quantities of radio physics such as the wavelength and light travel time depend on geometrical distances.

Moreover, particles below 1500 m do not contribute significantly to the overall radio signal, especially for the observer 400 m distant from the shower core. The results obtained in this section are comparable to the previous results obtained with REAS2. The charge excess component behaves similar to the one of the shower depth selection and thus, it is not shown here.

With the results derived in this chapter, we understood the details and the influence of the shower development on the pulse shapes and showed that the

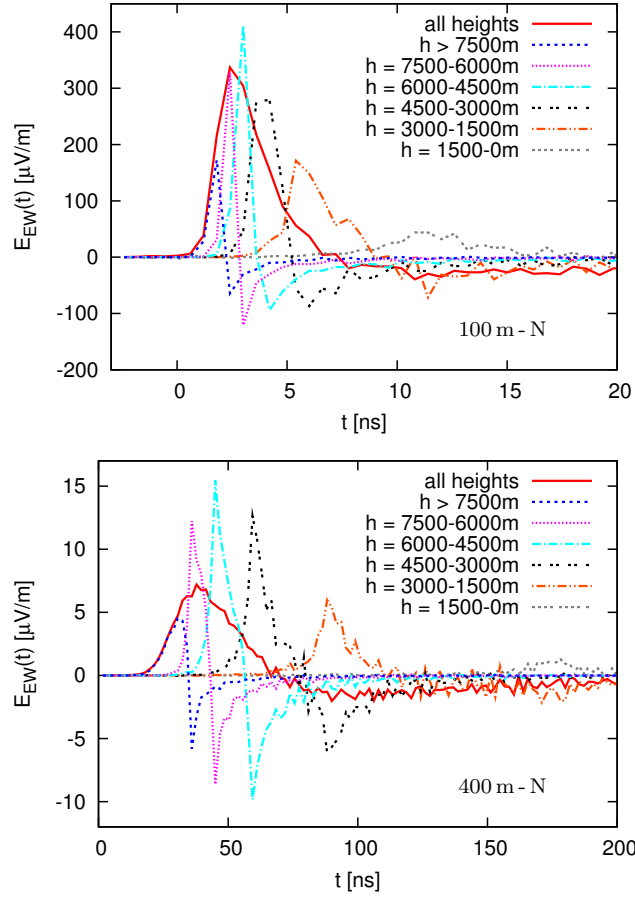


Figure 5.9: Contribution of different geometrical heights of the atmosphere to the east-west polarisation of the raw radio pulses for observers 100 m (top) and 400 m (bottom) north of the shower core.

pulse shape contains information on the shower development itself. In general, the previous results obtained with REAS2 were confirmed, but the relation of the charge excess pulse shape to the shower characteristics was studied for the first time. We discussed that the charge excess emission is dominated by the later shower phases. This is interesting since the geomagnetic emission is dominated by the shower phases around and before the shower maximum. Nevertheless, this behaviour is well understood due to the rising of the fraction of the charge excess with respect to the total charge with the development of the air shower.

With this understanding of the pulse shapes, the next step is to compare REAS3 with other models, in particular with an analytical approach which exhibits a simple correlation between pulse shape and shower development. Such a model is MGMR which is compared to REAS3 in the next chapter.

Comparison of REAS3 and MGMR simulations

In chapter 3, different simulation approaches and their implementations have been introduced. In the scope of this chapter, a detailed comparison of the MGMR model and REAS3 is given. In the past, REAS2 and MGMR made conflicting predictions on the pulse shape and the height of the amplitude. While REAS2 predicted unipolar pulses, the pulses calculated with MGMR were bipolar and a factor of 10 lower than the amplitudes obtained with REAS2. With REAS3, the missing radiation component resulting from the variation of the number of charged particles within an air shower is now considered. REAS3 thereby predicts bipolar pulses (cf. chapter 4). In MGMR, an additional contribution due to the charge excess was implemented (de Vries et al., 2010). These revisions motivate a detailed comparison of REAS3 and MGMR.

To make sure that the results are indeed comparable, a set of prototype showers has been defined for the simulations. All of these air showers have a fixed geometry with a specific energy for the primary particle and the observer positions are well-defined. For each prototype shower, a set of CORSIKA showers has been simulated. To consider shower-to-shower fluctuations, one typical shower was selected, i.e. one which has a shower maximum X_{\max} close to the mean X_{\max} . The chosen hadronic interaction models were QGSJetII.03 (Ostapchenko, 2006) and UrQmd1.3.1 (Bass et al., 1998). The values for the magnetic field have been set to the Argentinian magnetic field at the site of the Pierre Auger Observatory. The observer positions were all set to 1400 m above sea level, which corresponds to the site of the Pierre Auger Observatory. REAS3 is taking into account the full information of these showers (cf. Huege et al. (2007)) using histograms written out by COAST. Krijn D. de Vries used the longitudinal profiles of the CORSIKA simulated air showers to perform the MGMR simulations. This ensures that a

Table 6.1: Overview of the parameters set in MGMR-v1.6 used for the comparison with REAS3.

Parameter (name)	Value	Comment
drift velocity v_d	$0.025 \cdot c$	$c =$ speed of light
pancake thickness L	3.9 m	assumed as constant
fraction of charge excess	0.23	assumed as constant
velocity of the pancake	$v = c$	

similar parametrisation of the air shower is used for the provided MGMR simulations. Hence, the results of the two models are based on the same air shower characteristics. The difference between both, however, is the depth in which they take details of the air shower into account. Moreover, to calculate the radio emission from air showers with MGMR, some parameters need to be set before. For this comparison they are listed in table 6.1 and published in de Vries et al. (2010). Furthermore in MGMR, the lateral distribution of the particles in the shower pancake is switched off and the longitudinal distribution is parametrised. In section 6.2, these approximations are discussed in detail.

In section 6.1 a first comparison between the two models is shown with the focus on different aspects such as the raw (unlimited bandwidth) pulses of the radio emission, the frequency spectra, the lateral distribution of the radio signal, etc. As will be shown, the biggest differences of the model predictions occur close to the shower core. This might originate from the different shower models which get more important the closer the distance of the observer to the shower core. To study this effect, REAS3 was simplified to be more similar to the parametrisations done in MGMR. The results of this comparison are shown in section 6.2. Note, that for the comparison in this chapter the refractive index of the atmosphere was set to unity for both models.

6.1

REAS3 vs. MGMR

In figure 6.1, the pulses of REAS3 and MGMR for an observer at a position 200 m north from the shower core and the corresponding frequency spectra are shown emitted by a vertical air shower with primary energy of 10^{17} eV. Recalling the quantitative and qualitative differences in the predictions made by REAS2 and MGMR as discussed in section 3.1.5, the good agreement in the pulse shapes, amplitudes and the frequency spectra in particular for low frequencies is a breakthrough in the understanding of modelling the radio emission. This agreement warrants that a more detailed comparison between both models which follows in

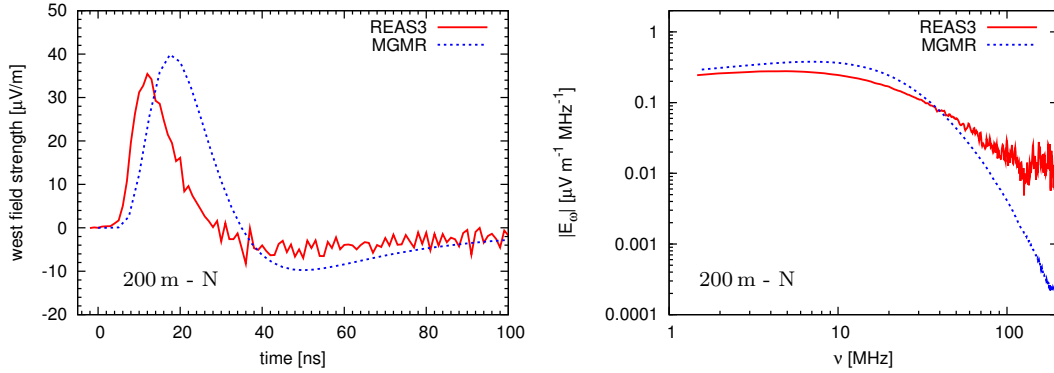


Figure 6.1: Comparison of the radio pulses and the frequency spectra predicted by REAS3 (solid lines) and MGMR (dashed lines) at an observer position 200 m north from the shower core. The agreement between both models is obvious, in particular recalling the qualitative differences between the previous versions.

Table 6.2: Overview of the set of selected prototype air showers which were simulated for a detailed comparison between REAS3 and MGMR. An inclination of -37° corresponds to the magnetic field geometry of the Pierre Auger Observatory.

Energy	Zenith, Azimuth	Strength of \vec{B}	Inclination of \vec{B}
10^{17} eV	$0^\circ, 0^\circ$	0.23 Gauss	-37°
10^{18} eV	$0^\circ, 0^\circ$	0.23 Gauss	-37°
10^{19} eV	$0^\circ, 0^\circ$	0.23 Gauss	-37°
10^{17} eV	$0^\circ, 0^\circ$	0.23 Gauss	0° (horizontal)
10^{17} eV	$0^\circ, 0^\circ$	0.23 Gauss	90° (vertical)
10^{17} eV	$0^\circ, 0^\circ$	0.0 Gauss	-
10^{17} eV	$50^\circ, 45^\circ$	0.23 Gauss	-37°

the next sections.

In table 6.2, the set of selected prototype air showers are listed. The set contains vertical air showers with different primary energies, one inclined air shower and vertical air showers where the magnetic field first was orientated perpendicular to the shower axis and second parallel to the shower axis. One shower was calculated in the absence of any magnetic field to compare the emission of non-geomagnetic radiation. This section focuses on three different points: vertical air showers (section 6.1.1), an inclined air shower (section 6.1.2) and special magnetic field configurations (section 6.1.3).

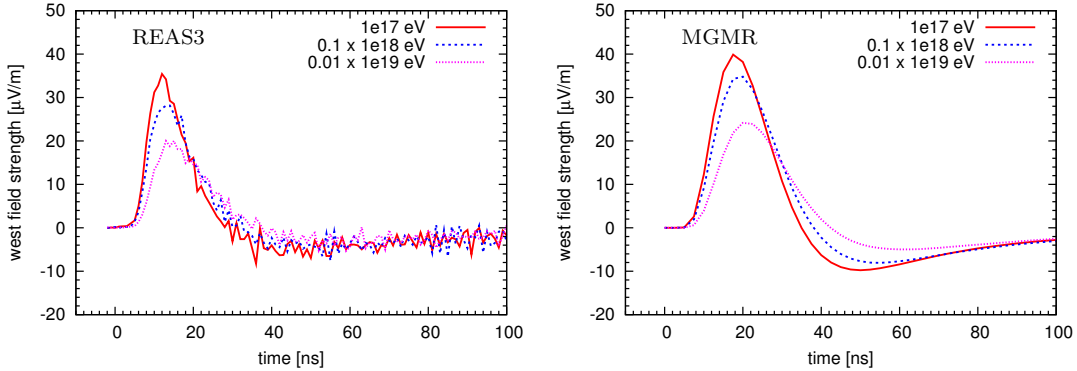


Figure 6.2: Comparison of the east-west polarisation component emitted by vertical air showers with three different primary energies at an observer position 200 m north from the shower core: 10^{17} eV (solid red), 10^{18} eV (dashed blue) and 10^{19} eV (dotted magenta) for REAS3 (left) and MGMR (right). Both simulations obtain similar results.

6.1.1

Emission from a vertical air shower

To compare the emission from a vertical air shower, three different primary energies were simulated. The primary energies were chosen as 10^{17} eV, 10^{18} eV and 10^{19} eV since these are the typical energies measured by the radio enhancement of the Pierre Auger Observatory, AERA. The higher the energy of the primary particle E_p , the more electrons and positrons are generated in an air shower. A rough estimation for the number of charged particles in the shower maximum is given by $N_{\max} = E_p/\text{GeV}$ (Allan, 1971). The scaling of the number of particles with the primary particle energy is directly reflected to the scaling of the field strength with particle energy for coherent radio emission, i.e. $N_{\max} \propto E_p^{0.96}$ (cf. section 4.4 in Huege (2004)).

The increase of the amplitudes with larger primary energy is true for the MGMR model as well as for the REAS3 simulation as shown in figure 6.2. The pulse for $E_p = 10^{18}$ eV is multiplied with 0.1 and for $E_p = 10^{19}$ eV, the pulse is multiplied with a factor of 0.01 to allow a better comparison between the pulses in the same plot. From figure 6.2, it is obvious that the height of the radio signal approximately (but not exactly) scales linearly with the energy. The reasons are well understood: On the one hand, the position of the shower maximum is deeper in the atmosphere for higher primary particle energies and thus, the lateral distribution of the radio signal gets steeper (cf. section 4.4 in Huege (2004)). Furthermore, the scaling of the field strength is $\propto E_p^{0.96}$. Combining the dependence of the primary particle energy and the position of the shower maximum, the dependence of the field strength on the primary particle energy is still describable by a power-law. (For further details we kindly refer the reader to

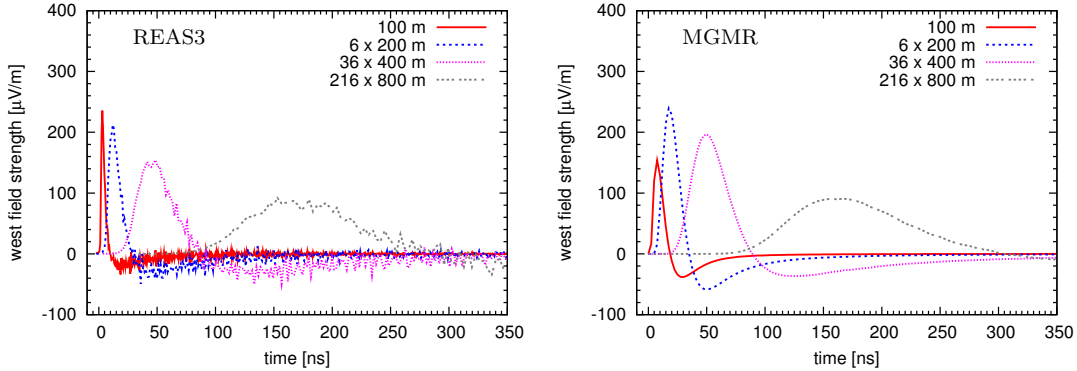


Figure 6.3: Comparison of the east-west polarisation component emitted by a vertical air shower with a primary energy of 10^{17} eV for REAS3 (left) and MGMR (right). The figures show pulses for observers at different lateral distances to the shower core. With increasing distance, the results of both models converge.

section 4.5. in Huege (2004).)

Since the characteristics of the radio signal are unchanged with higher energies and thus the result of the comparison between both models are not influenced by the choice of energy, the following comparison is concentrated on the vertical air shower with primary energy 10^{17} eV.

The figure also shows that the numerical noise level of REAS3 is somewhat higher than the noise level of the MGMR simulation. This effect is mostly relevant for near-vertical showers as discussed in this section. The figures of the inclined air shower illustrate this (cf. section 6.1.2). In the MGMR model, the motion of particles is averaged at the beginning of the calculation of the coherent emission and the corresponding electric field is calculated at the end. Thus, the result of the MGMR model is less affected by numerical noise.

Comparing the raw (unlimited bandwidth) radio pulses from the vertical air shower in figure 6.3, it is obvious that both models have bipolar pulses. Furthermore, the amplitudes obtained with REAS3 and MGMR agree within a factor of ~ 2 , recalling that the difference between the maximal field strengths of the raw pulses of the previous versions of both models was a factor of ten. Only close to the shower core, the deviations are getting larger. This effect will be seen in all of the other figures presented in this section as well. The remarkable agreement for larger distances is visible in the frequency spectra of figure 6.4 where the total electric field strength is shown as a function of frequency. For observers with lateral distances larger than 400 m, the results match accurately except for the incoherent noise. At 100 m observer distance, REAS3 predicts a flatter frequency spectrum than MGMR, especially in the frequency range of 30–80 MHz, in which

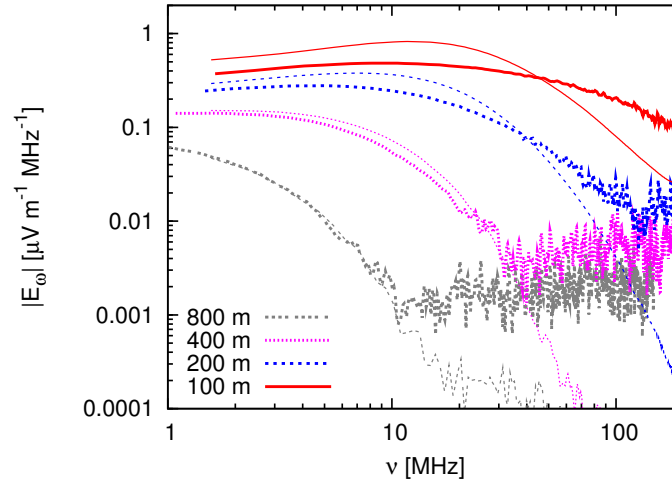


Figure 6.4: Comparison of the frequency spectra for REAS3 (thick lines) and MGMR (thin lines) for a vertical air shower with a primary energy of 10^{17} eV. The total spectral field strength is shown for observers at different lateral distances from 100 m up to 800 m.

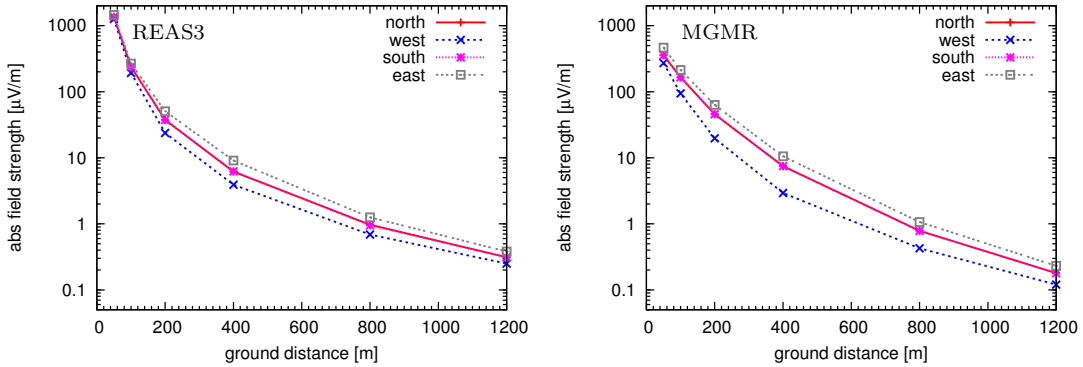


Figure 6.5: Comparison of the lateral dependences with full bandwidth amplitudes for a vertical air shower with a primary energy of 10^{17} eV predicted by REAS3 (left) and MGMR (right). The figures display the absolute field strength at a given lateral distance of an observer to the shower axis.

most of the experiments measure. The predicted amplitude of the radio emission by the two models in different azimuthal directions of the air shower can be compared with the lateral distributions of the peak amplitude of unlimited bandwidth pulses, i.e. the unfiltered signal, as illustrated in figure 6.5. The lateral distributions derived from REAS3 and MGMR show an evident east-west-asymmetry. This asymmetry is explained by the existing charge excess in air showers causing

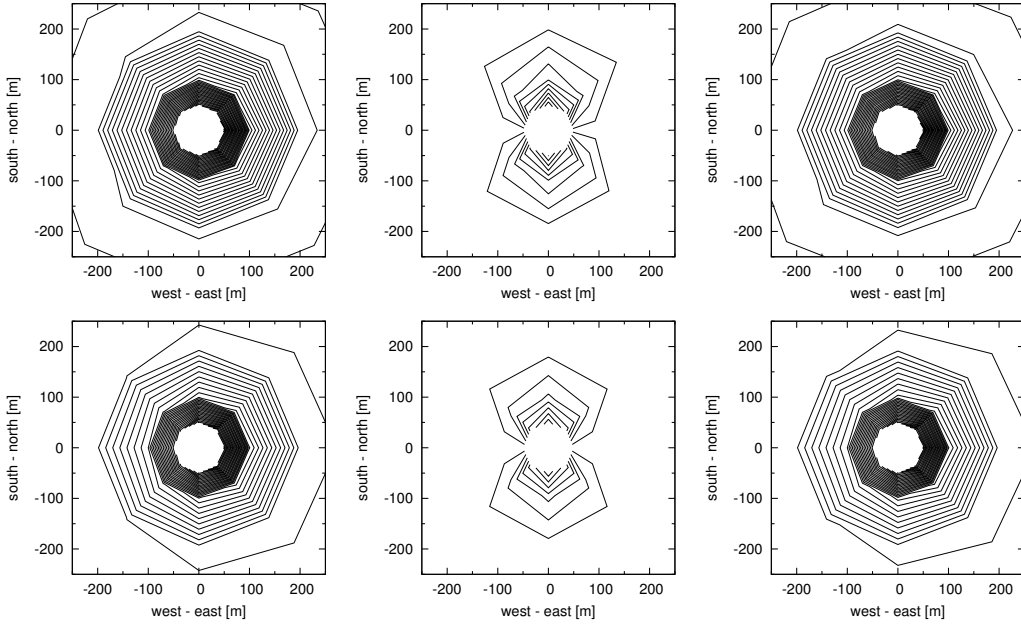


Figure 6.6: Contour plots of the 60 MHz field strength for the emission from a 10^{17} eV vertical air shower. From left to right: total field strength, north-south and east-west polarisation component. Contour levels are $0.1 \mu\text{Vm}^{-1}\text{MHz}^{-1}$ apart. The closest position of the simulated observers to the shower core is 50 m. Upper row: REAS3. Lower row: MGMR

a radiation contribution with a radial polarisation signature and was already discussed in chapter 4.5.2. Therefore, the two models give evidence that the radio emission from cosmic ray air showers is not purely $\vec{v} \times \vec{B}$ polarised (cf. chapter 4).

Looking at the contour plots of the 60 MHz spectral emission component displayed in figure 6.6, the same signature is visible. For radiation due to pure geomagnetic emission, no contribution for the north-south polarisation would be expected for the vertical air shower, as well as a symmetric pattern in the east-west polarisation component. The comparison of the contour plots, however, shows that there are still deviations between MGMR and REAS3, in particular in the strength of the east-west asymmetry predicted by the models.

6.1.2

Emission from an inclined air shower

In this section, the results for an inclined air shower are compared between REAS3 and MGMR. The primary energy of the air shower is 10^{17} eV and the air shower has a zenith angle of 50° . The azimuth angle of 45° denotes that the shower is coming from south-east (i.e., pointing to north-west). Figure 6.7 shows the raw

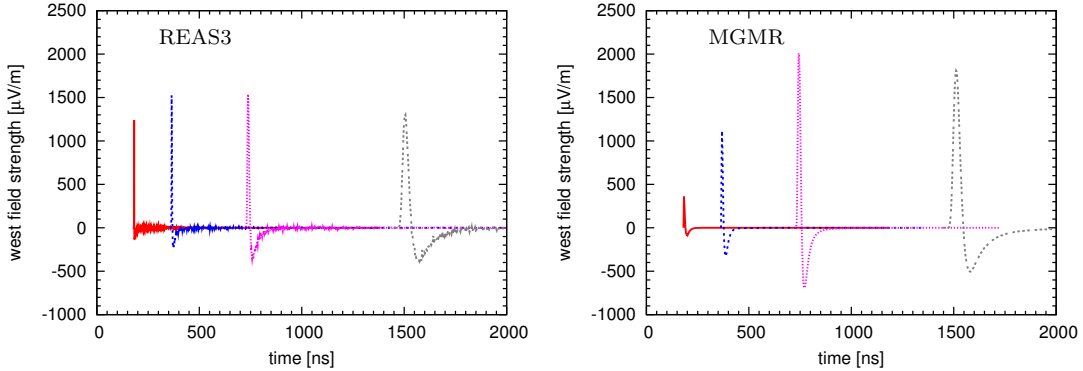


Figure 6.7: Comparison of the east-west polarisation component emitted by a 50° inclined air shower with a primary energy of 10^{17} eV for REAS3 (left) and MGMR (right). The figures show pulses for observers at different lateral distances to the shower core. With increasing distance, the results converge. For small distances, the predictions of both models differ by a factor of three.

pulses simulated with both models for this geometry. Please note that the zero time corresponds to the time when the primary particle would hit the ground. Since the observers are located north of the shower core and the air shower is coming from south-east, the emission arrives later than in the vertical case. Close to the shower core, the predictions of REAS3 and MGMR differ nearly by a factor of three, whereas the results are almost the same for larger lateral distances. The pulses derived by REAS3 close to the shower core exhibit higher amplitudes than the pulses obtained with MGMR. The larger deviations close to the shower core are evident in figure 6.8, where the lateral distributions are shown. The amplitudes predicted by REAS3 increase significantly with smaller distances to the shower axis. For MGMR, the lateral distribution is somewhat flattening to the center. Furthermore, the differences between each azimuthal observer direction, i.e. north, east, south and west, are larger for MGMR than for REAS3. In REAS3, the observers in the north and east receive nearly the same signal as the observers in the south and west. For MGMR this is not true. The largest discrepancies overall appear for the observers in western direction.

Above all, this might be a hint that close to the shower core, the details of the air shower model, which differs in REAS3 and MGMR become important. Where REAS3 is using the complex information from CORSIKA simulations, the MGMR model currently uses parametrisations of the air shower characteristics. This begins with the atmospheric model which follows one simple exponential in MGMR (in REAS the atmosphere is described differently for five layers as included in the U.S standard atmosphere description) and stops with the distribution of the electrons and positrons in the shower pancake. The macroscopic

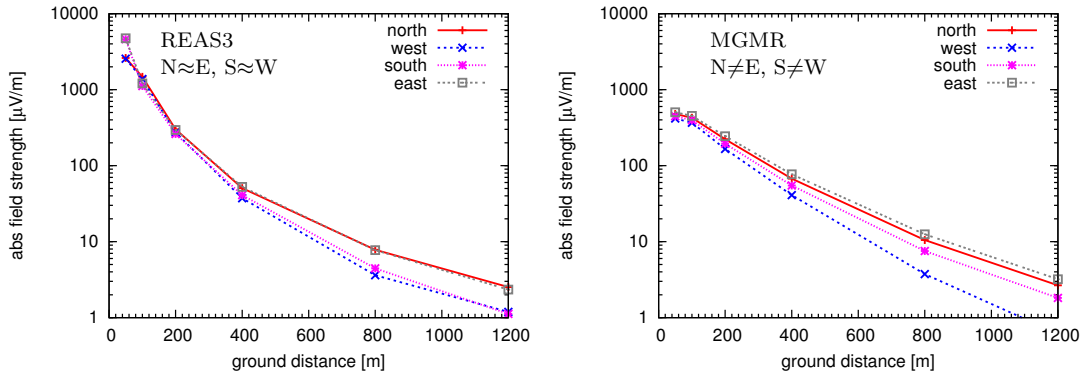


Figure 6.8: Comparison of the lateral dependences with full bandwidth amplitudes for an air shower with zenith angle of 50° and primary energy of 10^{17} eV predicted by REAS3 (left) and MGMR (right). The figures display the absolute field strength at a given lateral distance of an observer to the shower axis for the four orientations.

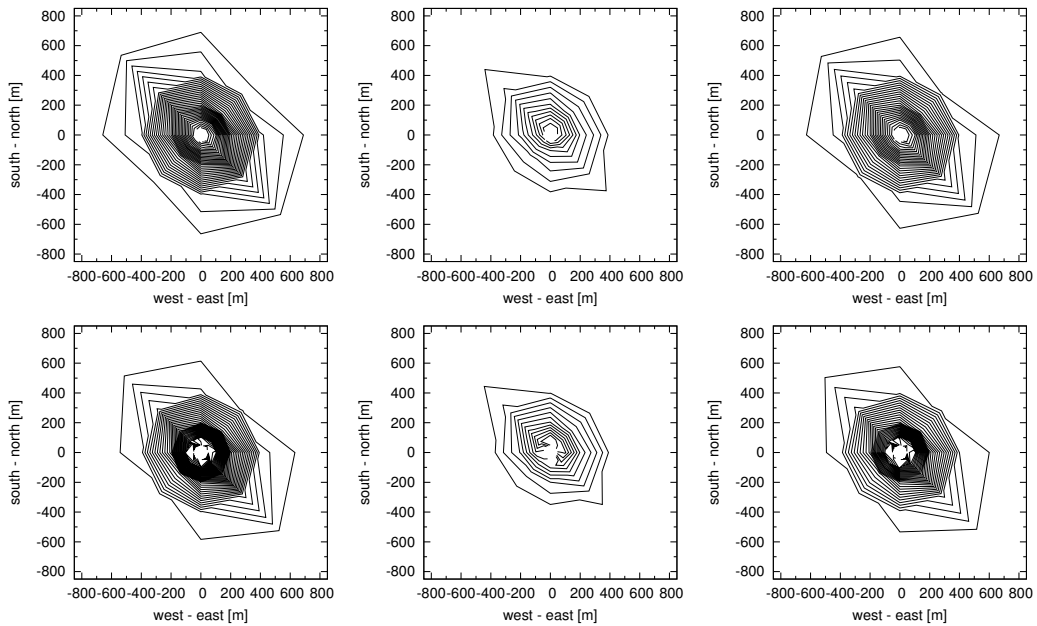


Figure 6.9: Contour plots of the 60 MHz field strength for the emission from a 10^{17} eV air shower with 50° inclination. The shower arrives from the south-east direction. From left to right: total field strength, north-south and east-west polarisation component. Contour levels are $0.1 \mu\text{Vm}^{-1}\text{MHz}^{-1}$ apart. The closest position of the simulated observers to the shower core is 50 m. Upper row: REAS3. Lower row: MGMR

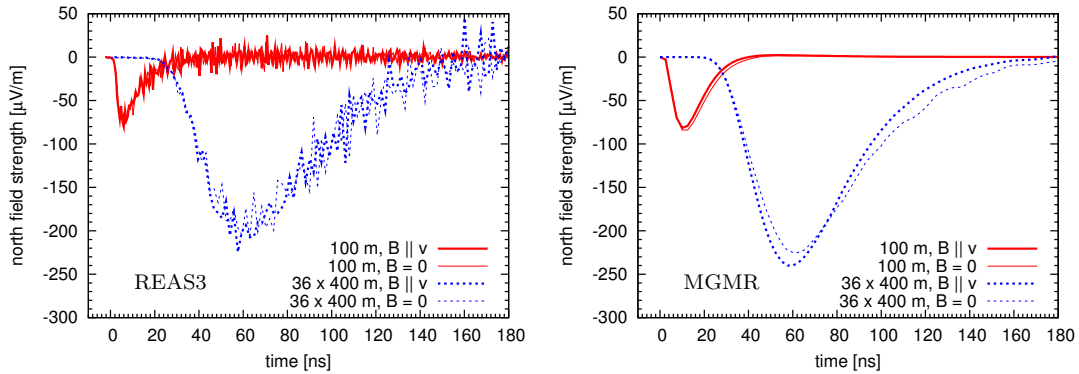


Figure 6.10: Comparison of the pulses emitted by a vertical 10^{17} eV air shower in the absence of a magnetic field (thin lines) and a magnetic field parallel to the shower axis (thick lines). Left: REAS3. Right: MGMR.

model neglects the lateral distribution of the single particles in the pancake and uses a parametrisation for the thickness of it. This has a larger impact on inclined air showers than for nearly vertical ones, as identical ground distances correspond to smaller effective axis distances. The latter is true, since the effective distance d_e to the axis is proportional to the cosine of the zenith angle Θ , i.e. $d_e = \cos \Theta \cdot d_g$, where d_g represents the distance on ground to the shower core. Thus, the larger the zenith angle, the smaller becomes the effective distance and with this the shower details get more important. Moreover, the geometrical distance to the position of the shower maximum X_{\max} increases with larger Θ and thus, the angle between shower axis and the line of sight between X_{\max} and observer effectively gets smaller.

The larger signal derived with REAS3 for the east-west polarisation and the general agreement between both models can also be seen in the contour plots for the inclined air shower illustrated in figure 6.9.

6.1.3

Specific magnetic field configurations

In addition to the realistic air shower geometries shown in the last sections, it is interesting to look at more contrived situations such as some special magnetic field configurations, since the Earth’s magnetic field is responsible for the geomagnetic radio emission in air showers. In this section, the magnetic field was once switched off completely and once was chosen to be parallel to the air shower axis. With these special configurations of the magnetic field, the influence of the radiation due to the variation of the number of charged particles, i.e. the “Askaryan radiation” (but without Cherenkov-like emission) (?Askaryan, 1965), is studied.

Figure 6.10 shows that the results for these two configurations are indeed very

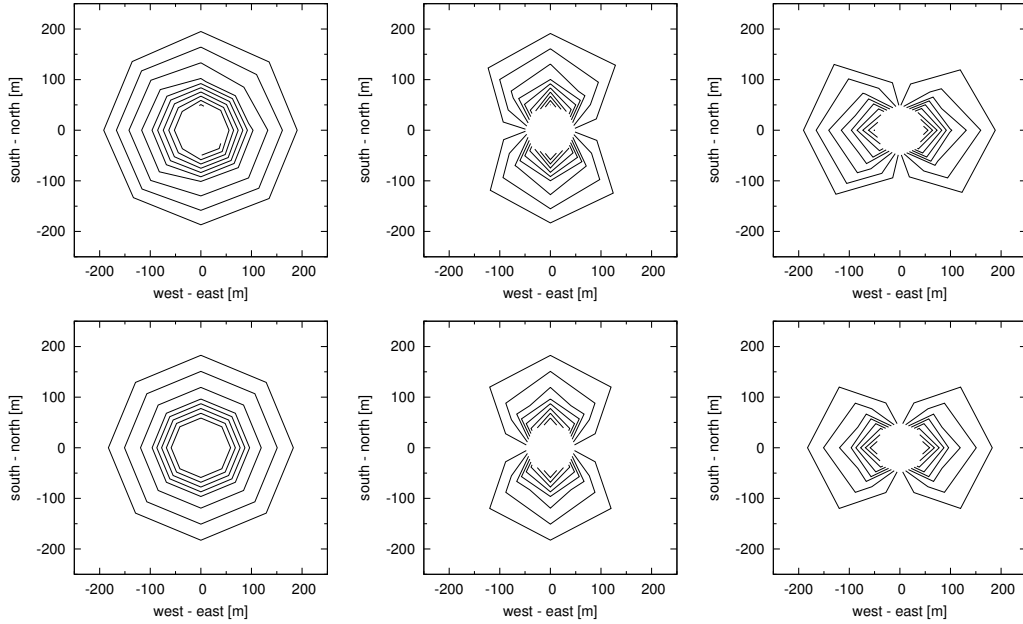


Figure 6.11: Contour plots of the 60 MHz field strength for the emission from a 10^{17} eV air shower where the magnetic field is switched off completely. From left to right: total field strength, north-south and east-west polarisation component. Contour levels are $0.1 \mu\text{Vm}^{-1}\text{MHz}^{-1}$ apart. The closest position of the simulated observers to the shower core is 50 m. Upper row: REAS3. Lower row: MGMR

similar. The predictions of REAS3 and MGMR agree very well. The differences in the strength of the pulses are much less than a factor of two. The pulses for observers at 400 m distance are multiplied with a factor of 36 for better comparison. The two models show also the expected radial polarisation patterns as displayed in the contour plots of figure 6.11. The resounding agreement between both models for the two situations shown in this section are evident for the increased understanding of the radio emission mechanism with REAS3.

6.1.4

Discussion of the comparison

Summing up the results of the previous sections, the comparison between REAS3 and MGMR shows an overall agreement within a factor of $\sim 2 - 3$. Remembering that few years ago the models predicted even different pulse shapes and characteristics in the frequency spectra, this agreement is a milestone in the understanding of radio emission from cosmic ray air showers. It should be stressed once more that the models are technically very different and completely independent from each other.

While in REAS3, the radiation of single particles is superposed and no assumptions have to be made, for the macroscopic treatment of radio emission as implemented in MGMR a number of free parameters have to be set with the advantage of a short calculation time. Furthermore, in MGMR different processes are taken into account individually, i.e. the transverse currents, the static dipole and the charge excess. Looking at the details of the results from the comparison between both models, it is obvious that there are still deviations which are too large to be ignored. Especially for the inclined shower studied in section 6.1.2 the assumption that the shower model is important was strengthened. In several figures, it was shown that the pulse amplitudes predicted by REAS3 are larger than the amplitudes from MGMR, at least for small observer distances to the shower core. The reason for this deviation has to be studied in detail, since also these discrepancies need to be understood. For the future, the aim is to understand the existing differences not within a factor of 2-3, but within less than 10% effects. Thus, the influence of the air shower modes has to be studied and with this if the differences in the underlying air shower models are responsible for the deviations. In MGMR, the air shower model is parametrized whereas it is based on histograms of CORSIKA simulations for REAS3. Hence, the air shower model implemented in REAS3 has to be simplified to get a more similar model to the one used in MGMR and to study the effects on the radio emission. In the following section, this will be done.

6.2 Comparison of MGMR with simplified REAS3

To adapt REAS3 for comparing the details with MGMR, first the differences of the air shower models need to be identified. One major difference is that the distribution of the particles in the shower pancake are different. Where in REAS3 the distributions follow the distributions of the detailed CORSIKA simulations, in MGMR parametrisations are used.

The arrival time distribution, i.e. the longitudinal displacement of the particles inside the shower pancake, in MGMR is fitted with a Γ -probability distribution function and converted into thickness following the given relation:

$$f(h) = h \cdot e^{-2h/390 \text{ cm}} \cdot \frac{4}{(390 \text{ cm})^2} \quad (6.1)$$

where h denotes the distance from the shower front. To mimic the behaviour of MGMR in REAS3, we replaced the longitudinal displacement of the particles in the shower core according to this Γ -probability distribution function.

Next, the lateral displacement of the particles in the shower core had to be changed. In MGMR, this displacement is not directly considered, but a radiation contribution from a static dipole with a length of 1500 cm is added to the overall

radio signal. Hence, in REAS3, we shifted the electrons by 750 cm in the eastern direction of the shower axis and the positrons by 750 cm in the western direction and switched off the lateral distribution of the particles in the shower pancake.

Further parametrisations and approximation made in MGMR have not been considered for this comparison. These parametrisations are briefly discussed in the following. REAS3 and MGMR differ also in the amount of charge excess. In REAS3, the fraction of the charge excess with respect to the total number of charges increases with the shower development (cf. figure 5.8 in section 5.3). In MGMR, the ratio is set to 25% for the whole air shower.

Furthermore, the velocity of the particles in the shower pancake is set to the speed of light, i.e. $\beta = 1$, in the case of MGMR. In REAS3, the particle velocities are taken individually according to the histograms. An unknown influence might arise due to the underlying atmosphere models used by REAS3 and MGMR which are not equal. In REAS, the same atmosphere models are implemented as given in CORSIKA. For the present prototype showers, the US standard atmosphere was used. The atmosphere model implemented in MGMR, however, follows the following exponential function for the whole air shower development:

$$X[h] = \frac{1000.0}{\cos \theta} \frac{\text{g}}{\text{cm}^2} \cdot \exp \left[\frac{-\log(0.68) h}{4000.0 \text{ m}} \right], \quad (6.2)$$

where θ is the zenith angle and h is the height above sea level from where the signal is emitted. To calculate the radio emission in REAS3 with a modified atmosphere, the atmosphere model has to be adapted in CORSIKA as well, since this influences the air shower development. In this section, however, the modified atmosphere has not been considered.

In figure 6.12, the pulses of REAS3, MGMR and the simplified REAS3 are shown for observer distances of 100 m and 800 m. It is obvious that close to the shower core, the parametrisations affect the radio emission the most. However, the agreement is not increasing when using the same parametrisations in REAS3 which are used in MGMR. Hence, the different atmosphere models should be considered as well as the constant charge excess ratio of the electrons. Nevertheless, it was shown that the air shower model has large impact on the radio signal close to the shower core. At 800 m distance, the radio signal is hardly affected by the air shower model. For observer distances comparable with the average distance of the LOPES antennas to the shower core, thus, it is very important to take into account the details of the air shower development as is done in REAS3.

In summary, a breakthrough in the understanding of the modelling of radio emission from air showers was achieved. We showed that for the first time, two independent and complementary models, REAS3 and MGMR, agree in the predicted pulse shapes and the height of the amplitudes within a factor of ~ 2 . The next

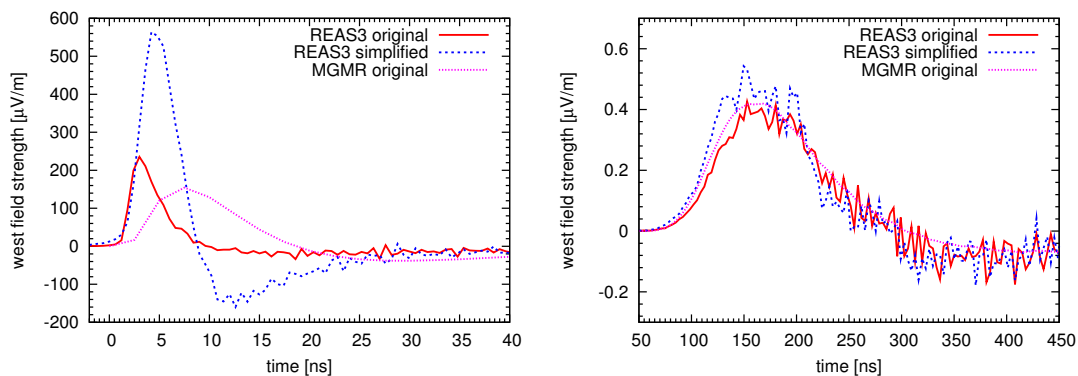


Figure 6.12: Comparison of the radio signal predicted by REAS3, MGMR and the simplified REAS3. The influence of the parametrisations is at 100 m (lhs) much larger than at 800 m (rhs). The simplified REAS3 and MGMR, however, agree not better than before.

step will be to understand the differences on a 10%-level and therefore further develop the models and identify the reasons for the remaining discrepancies. With the results derived in this chapter, the need of a comparison between data and simulations is obvious. Hence, in the following chapter a comparison of REAS3 simulations with LOPES data is drawn.

Comparison of REAS3 with LOPES data

The comparison of different models as discussed in the previous chapter showed that the understanding of radio emission from air showers increased significantly with the incorporation of the endpoint contributions in REAS3. Nevertheless, the real interest lies in the questions if simulations describe measured data correctly and if predictions made by simulations can be verified by comparison with data. In this chapter, the results of the studies regarding the agreement between LOPES data and REAS3 simulations are discussed. However, the comparison of simulations and measured data is influenced by two major circumstances, independent from the selected model or experiment.

On the one hand, uncertainties on the reconstruction of the measured observables, e.g. the primary energy and the core position of the air shower, influence the results of the simulation, since they are used as input parameters for the simulation. These depend on the respective experiment. For instance, the core position uncertainty of KASCADE is in the order of a few meters while for the SD reconstruction of the Pierre Auger Observatory, the uncertainty on the core position can be more than 100 m. Such uncertainties have to be taken into account, however, for the comparison with LOPES data, mainly the uncertainty on the primary energy is important and discussed where appropriate.

On the other hand, shower-to-shower fluctuations, which are mainly determined by the first few interactions in the air shower, impact the predicted radio emission from simulations. Figure 7.1 shows the longitudinal profiles of 100 simulated air showers with the same input parameters, i.e. a proton with primary energy of $1.24 \cdot 10^{17}$ eV and a zenith angle of 43.6° . The difference between the smallest and the largest atmospheric depth of the shower maximum is around $300 \frac{\text{g}}{\text{cm}^2}$. The shower-to-shower fluctuations need to be considered for the comparisons be-

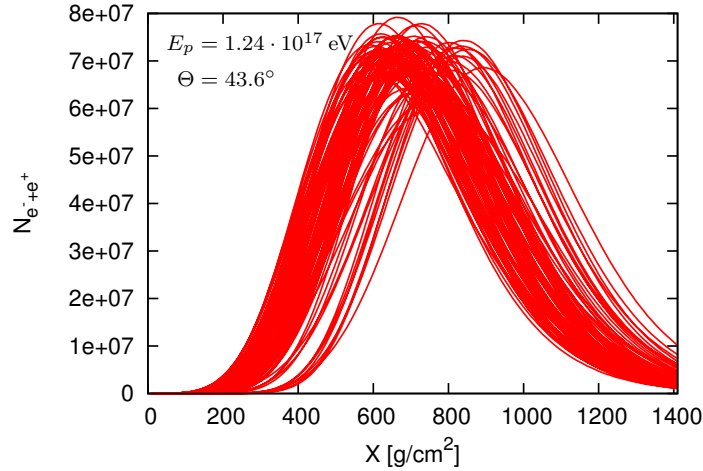


Figure 7.1: The longitudinal profiles of 100 proton induced air showers for the same input parameters simulated with QGSJet and UrQmd. On the x-axis is the atmospheric depth X in $\frac{\text{g}}{\text{cm}^2}$ and on the y-axis the number of electrons and positrons. The position of the shower maximum varies from $\approx 600 - 900 \frac{\text{g}}{\text{cm}^2}$.

tween simulation and data. Hence, one challenge for the comparison of data with simulations is to choose an adequate simulated air shower. This requires a sophisticated selection criterion which is technically feasible. Before starting this work, however, the selection method was limited by technical reasons (details on this limitations are discussed in the following section).

Already with REAS2, comparisons between data and simulations have been made (cf. section 3.1.6), but deviations between both were not understood. With the significant changes in the radio emission model, this comparison is repeated with REAS3. Furthermore, the analyses of LOPES data have been improved significantly in the recent years as well, e.g. the treatment of noise is nowadays implemented self-consistently in the LOPES analysis pipeline (Schröder et al., 2010). Within the scope of this thesis, a new selection criterion which is based on the number of muons measured by KASCADE was developed to choose an adequate air shower for the comparison between data and simulations. This enhanced air shower selection is useful also for other applications, e.g. the fluorescence detection, as it allows “top-down” simulations of air showers chosen to reproduce any given air shower observable ($N_\mu, X_{\text{max}}, \dots$). Details of the selection process are presented in section 7.1. In section 7.2, the results of a comparison of REAS3 simulations produced with the muon selection and LOPES data are shown.

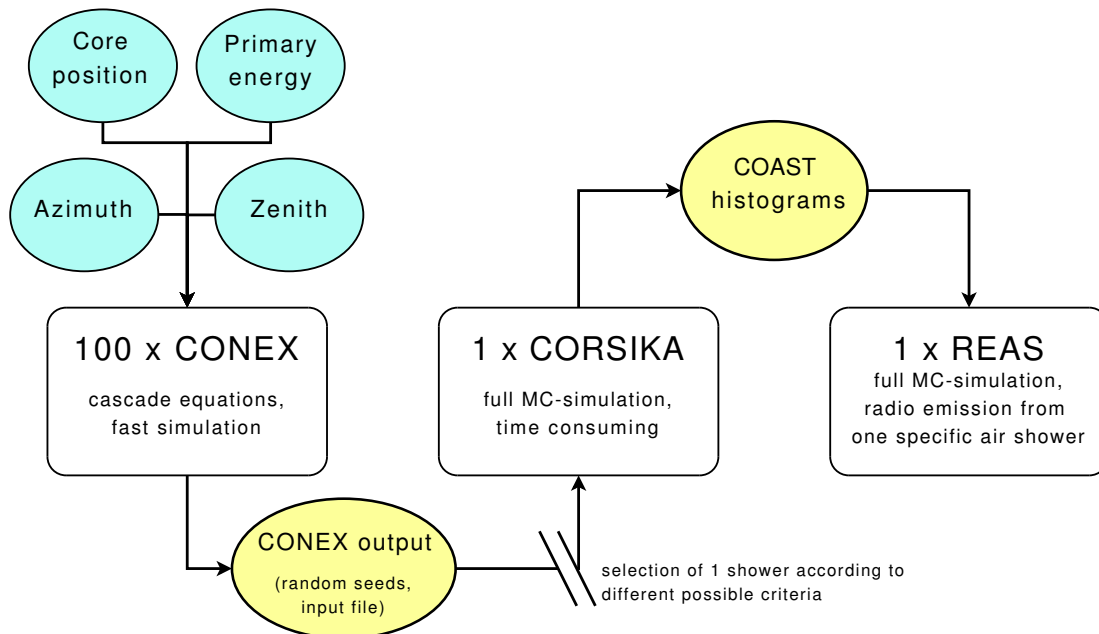


Figure 7.2: Flow chart of a typical simulation chain. In the blue highlighted ellipses are input parameters determining the air shower physics. In the yellow highlighted ellipses are parameters or information from the programs itself for the following program.

7.1

Methods of air shower selections

For simulating the radio emission from air showers and considering shower-to-shower fluctuations, a given procedure as specified below is followed. This is necessary, since only a few air shower and REAS3 simulations per measured cosmic ray event are processable due to limited computing times. Figure 7.2 illustrates a flow chart of a typical simulation chain as developed in the scope of the present work. First of all, the air shower parameters for the incoming direction, the core position and the energy of the primary particle are input to the fast air shower simulation program CONEX (Pierog et al., 2006). With this code, which is based on cascade equations, a number of air showers is simulated. Taking the same parameters for these simulations, the resulting air showers will be different due to shower-to-shower fluctuations. Next, one of these air showers is selected to be simulated with CORSIKA (Heck et al., 1998). Finally, the REAS simulation based on the histograms written by COAST (Lafèbre et al., 2009) provides the radio emission from this air shower. With this procedure, the computing time is optimized while taking into account the shower-to-shower fluctuations.

The challenge of this simulation chain, however, is the reproducibility of the

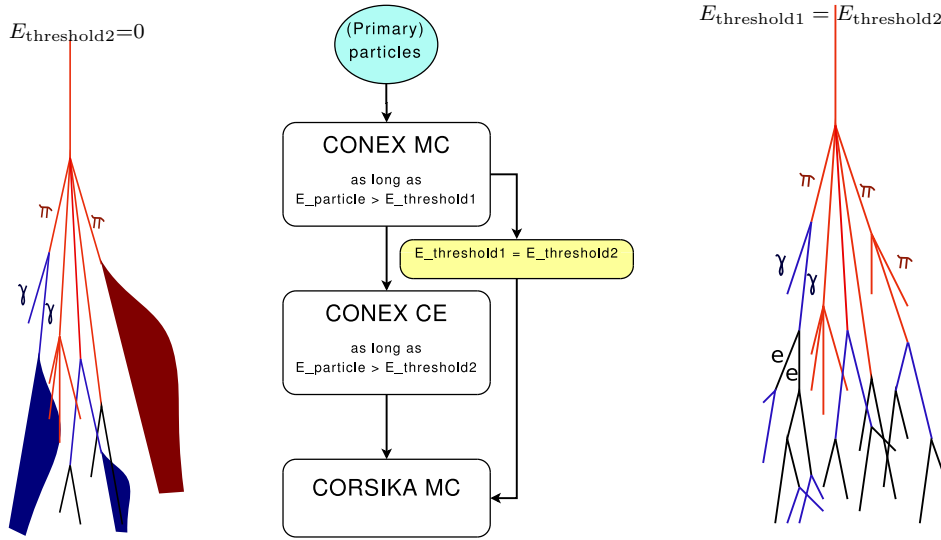


Figure 7.3: Sketch of the structure of CONEX (lhs) and CORSIKA (rhs) (Ulrich, 2010) and the flow chart of the functionality of both (middle). The coloured boxes illustrate the subshowers calculated with cascade equations. For the simulation of 100 CONEX showers (cf. figure 7.2), the energy threshold $E_{\text{threshold}2}$ is equal to zero (lhs). Thus no CORSIKA simulation is performed. For the single CORSIKA shower, the energy thresholds 1 and 2 are the same (rhs).

same air shower by CORSIKA for the selected CONEX simulation, i.e. the predicted number of muons at the ground, the longitudinal development of the air shower components, the position of the shower maximum and all the other air shower characteristics. With the previous versions of CONEX and CORSIKA, the technical limitations have been too high and it was not possible to reproduce the exact same air shower. In the past, CONEX and CORSIKA have been two independent programs using different algorithms and random number generators. Thus, it was not possible to reproduce a shower which was simulated with CONEX based on cascade equations by CORSIKA, a full Monte Carlo code, since the random number sequences would differ and influence the simulated interactions. In figure 7.3, the structure of CONEX and CORSIKA is shown. The challenge was to combine both in one program, so that the change from cascade equations to Monte Carlo simulation became possible using at the same time the complex air shower routines as implemented in CORSIKA.

So far, the reproducibility worked reliably only for the selection criterion based on the mean shower maximum and only with restrictions¹ to the selected CONEX

¹For the reproducibility, only simulations were considered where the number of the created particles in the first interaction is at least four and the energy is divided approximately equally to all particles generated in this interaction.

shower. However, the selection of an air shower by the averaged shower maximum might not be the best, since LOPES is not measuring necessarily an averaged cosmic ray air shower.

With Tanguy Pierog (IK, KIT), we worked on a CORSIKA version in which CONEX is directly implemented and we made use of this new (so far not published) version to develop a selection criterion based on the number of muons measured by KASCADE. With CONEX implemented in CORSIKA it is guaranteed that the same algorithms are used and the random numbers of CONEX represent the random numbers of CORSIKA. Depending on the energy thresholds $E_{\text{threshold1}}$ and $E_{\text{threshold2}}$, a change from CONEX Monte Carlo to CONEX cascade equations or CORSIKA Monte Carlo simulations and a change after the CONEX cascade equations to the CORSIKA Monte Carlo simulations is possible. In the simulations generated for this comparison, the second energy threshold was set to zero for the 100 fast CONEX simulations (cf. lhs of fig. 7.3) and later set to $E_{\text{threshold1}}$ to get the full Monte Carlo simulation with CORSIKA for the specific air shower (cf. lhs of fig. 7.3).

Thus, only the random numbers (seeds) have to be adopted from the specific CONEX simulation to the specific CORSIKA simulation. With this newly developed CORSIKA version, the number of muons is reproduced within deviations less than 5%. Only with this, the selection criterion for LOPES became realisable. The details of this selection criterion are given in the next section².

If the radio detection is combined with another detection method, e.g. a particle detector array, the reconstructed parameters of the particle detectors such as energy, core position and incoming direction can be used as input for the CONEX simulations. For the selection of one single air shower, two general possibilities exist:

1. Select a typical air shower by calculating the mean value of a certain shower parameter, e.g. calculate the mean value of the shower maximum X_{max} and select the shower which has the smallest deviation from this.
2. Select a specific air shower by comparing a simulated shower parameter with a reconstructed observable from a measurement and select the shower with the smallest deviations, e.g. the number of muons at the ground measured by particle detectors or the shower maximum measured by fluorescence telescopes.

The applicability of each selection method depends on the particular analysis. For studies regarding the general behaviour of the radio emission, a selection based on a typical air shower is better. For evaluating the quality of REAS3 with measured

²In the following the selection criterion based on the number of muons is named as the *new* selection criterion, whereas the criterion based on the averaged shower maximum is called the *old* one.

data, the second method is preferable since the specific air shower represents the measured air shower with a higher probability than a typical air shower. Moreover, for the studies on the mass sensitivity of the radio signal, a selection criterion is preferable which does not explicitly fix the shower maximum. This selection method is only suitable if the complementary detection method provides an observable with small uncertainties, such as the number of muons in the case of KASCADE for LOPES simulations or the shower maximum reconstructed by the fluorescence telescopes of the Pierre Auger Observatory for AERA.

7.1.1

Application to LOPES data

As a starting point, the air shower parameters reconstructed by KASCADE (and KASCADE-Grande³) are used as input parameters for CONEX⁴, i.e. the primary energy, the azimuth angle, zenith angle and the core position of the air shower. A difference in the number of air showers simulated for proton and iron is made since the shower-to-shower fluctuations are less for iron than for proton. To optimize the computing time, the number of CONEX showers is adapted to the width of the fluctuations. For all simulations in this chapter, the number of air showers simulated with CONEX is 200 if the primary particle is a proton and 100 in case of an iron nucleus as primary particle. With the new selection criterion, it is important to set the input parameters for the CONEX simulation according to the KASCADE set-up. First, the observer height has to be 110 m as this represents the height above sea level of the KASCADE detectors. Furthermore, in CONEX, the cut-off energies of the muons need to be equal to the energy threshold for muons of KASCADE, i.e. muons with energies below 230 MeV are no more tracked in the CONEX simulation. This is important, since KASCADE is only sensitive to muons with energies larger than 230 MeV and the number of muons simulated with CONEX have to be comparable with the measurement. For the full CORSIKA simulation, however, the energy cuts have to be set lower, since these muons can produce electrons and positrons contributing to the radio signal of the air shower. With CONEX implemented in CORSIKA, it is possible to choose different energy cuts for the cascade equations than for the full Monte Carlo simulation. In principle, this is everything that has to be considered for the new criterion.

However, due to the application of the selection criterion to the muon number of KASCADE, it turned out that the number of muons reconstructed by KASCADE

³In the following, it is not distinguished between KASCADE and KASCADE-Grande since the procedure is equal for both. If any difference in the selection criterion has to be made, it is stated in the text.

⁴In the following, the CONEX implemented in CORSIKA is used and not the independent program.

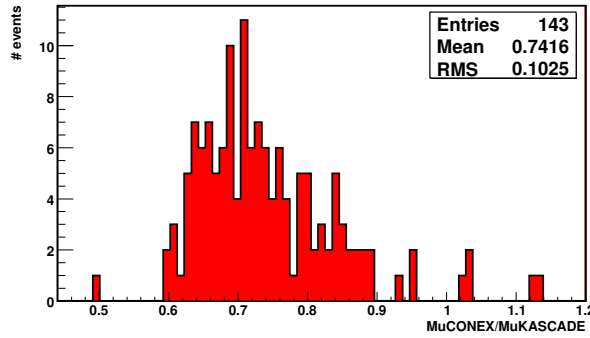


Figure 7.4: The histogram of the ratio between the mean muon number $\langle N_{\mu, \text{CONEX}} \rangle$ of the proton induced air shower and the KASCADE (not Grande) measured muon number for the events from the third zenith angle bin. The weighting factor is determined by the mean of this histogram, in this case 0.7416.

are higher than expected for the selected LOPES events⁵. Since KASCADE is built mainly for energies below 10^{17} eV which is the typical minimum energy cut of LOPES analyses, the punch through of the electromagnetic component seems to bias the measured number of muons (cf. figure 7.4). For the new selection criterion, this would lead to the situation that the air shower which has the largest number of muons is selected, which is not realistic at all. The solution is a downscaling explained below of the measured number of muons before comparing the numbers obtained by CONEX with those measured by KASCADE.

The procedure for downscaling the measured muon numbers was performed separately for the two primary particle types. For each event selected for the comparison, the averaged number of muons was calculated from the air showers simulated with CONEX. This results in a mean number of muons from CONEX for each LOPES event, e.g. for each of the proton induced air showers:

$$\langle N_{\mu, \text{CONEX}} \rangle = \sum_{i=1}^{200} \frac{N_{\mu, i}}{200} \quad (7.1)$$

where $N_{\mu, i}$ is the number of muons of a single air shower simulated by CONEX for one event. For all events, the per-event averaged number of muons was compared with the number of muons reconstructed by KASCADE. By determination of the mean ratio between the averaged and the reconstructed values, a weighting factor for the number of muons measured was derived for three different zenith angle bins (since the punch through is larger for vertical air showers than for inclined

⁵The same is valid for the events reconstructed with KASCADE-Grande, but the overestimation of the number of muons is smaller.

Table 7.1: The weighting factors of the number of muons reconstructed by KASCADE and KASCADE-Grande for three different zenith angle bins and the primary particles proton and iron nuclei. The weighting factors are used for the comparison of the number of muons simulated by CONEX and reconstructed by KASCADE. To determine the weighting factors, the same events were used as selected for the comparison in section 7.2.

	0 – 20°	20 – 32°	32 – 45°
KASCADE, proton	0.5997 ± 0.0502	0.6840 ± 0.0886	0.7416 ± 0.1025
KASCADE, iron	0.7779 ± 0.0655	0.8846 ± 0.1152	0.9555 ± 0.1298
K-Grande, proton	0.6408 ± 0.0591	0.7072 ± 0.0901	0.7502 ± 0.0841
K-Grande, iron	0.8329 ± 0.0776	0.9129 ± 0.1197	0.9623 ± 0.1077

showers).

In figure 7.4, the histogram for the determination of the weighting factor for the proton induced air showers reconstructed by KASCADE in the third zenith angle bin is shown. It can be seen that the number of muons reconstructed by KASCADE are in average $\sim 25\%$ larger than the number of muons derived with CONEX. A clear distribution around the value 0.74 is visible with a spread of roughly 15%. In table 7.1, the weighting factors applied in the three zenith angle bins for KASCADE and KASCADE-Grande are listed.

With the settings stated above and the corrected number of muons, the new selection criterion is applicable to the simulations used for the comparison with data. Figure 7.5 shows the longitudinal profiles of 100 simulated air showers for one single event with the primary energy of $1.24 \cdot 10^{17}$ eV and zenith angle of 43.6° . On the left-hand side, the longitudinal development of the number of muons ($\mu^- + \mu^+$) is shown. The air shower which has nearly the same number of muons at ground as measured by KASCADE is marked in light blue (long dashed). The air shower which has a shower maximum close to the averaged X_{max} is marked in dark blue (short dashed). On the right-hand side, the longitudinal development of the electrons and positrons of these showers is shown. It is obvious that the new and the old selection criteria result in the selection of two different showers.

For the comparison with data, the muon selection has the advantage with respect to the previous X_{max} selection that the number of muons is directly given by KASCADE. Furthermore, the shower maximum is not directly dependent on the number of muons at ground. Consequently, the range of X_{max} is much larger for a set of events (see figure 7.6) which is important for the analyses on the mass sensitivity of the radio signal and other characteristics dependent on X_{max} . However, the total range for the shower maximum is slightly restricted with the new selection criterion. In figure 7.6, the longitudinal profiles from six air showers

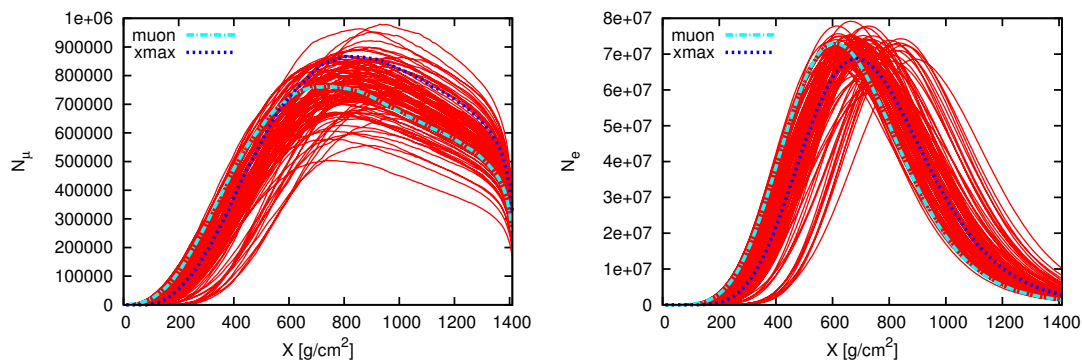


Figure 7.5: The longitudinal profiles of 100 air showers with the same input parameters. On the x-axis is the atmospheric depth X in $\frac{\text{g}}{\text{cm}^2}$ and on the y-axis the number of muons (lhs), respectively, the number of electrons and positrons (rhs). The showers which would be selected with the different selection criteria are marked.

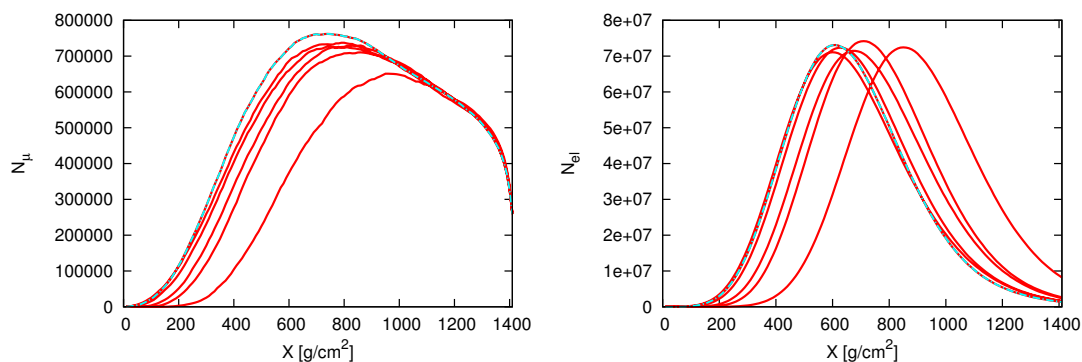


Figure 7.6: The longitudinal profiles of six air showers which have nearly the same number of muons at ground as measured with KASCADE and have been simulated with the same input parameters. On the x-axis is the atmospheric depth X in $\frac{\text{g}}{\text{cm}^2}$ and on the y-axis the number of muons (lhs) respectively the number of electrons and positrons (rhs). The longitudinal profiles of the single showers differ evidently. The selected shower is marked by the dashed line.

are shown for which the deviations in the simulated and measured numbers of muons is less than 1% for the same input parameters. Looking at the right-hand side of figure 7.6, it is obvious that the shower maximum for this specific event varies more than $200 \frac{\text{g}}{\text{cm}^2}$. The shower selected by the muon criterion is marked as before.

The variation in the longitudinal profiles for air showers which would lead to identical measured observables from experiments such as KASCADE is expected

Table 7.2: Overview of the number of events selected for the comparison of REAS3 simulations with LOPES data. The set-up of LOPES is listed in the first column, where LOPES 30 consisted of 30 antennas measuring the east-west polarisation of the radio signal and LOPES dual consisted of 15 antennas measuring the east-west polarisation and 15 antennas measuring the north-south polarisation of the radio signal. The second row contains the information if the shower core of the event was inside KASCADE or KASCADE-Grande.

LOPES setup	Shower core in	Number of events
LOPES 30	KASCADE	93
LOPES 30	KASCADE-Grande	47
LOPES dual	KASCADE	220
LOPES dual	KASCADE-Grande	168

to have a visible signature in the radio signal. Thus, the combined measurement of radio emission and particles might bring large profit (Huege et al., 2008; Schröder, 2011).

Furthermore, it has to be investigated how the radio signal of one specific event is changing with a different selected air shower close to the number of muons measured by KASCADE. However, this topic will not be discussed here. Simulations obtained with the muon selection have already been used to study the arrival times and the wave-front of the radio emission (Schröder, 2011). Moreover, they are currently used to study the sensitivity of the radio signal on the mass composition (Palmieri, 2011).

7.2

Results of the comparison with LOPES data

For the comparison of the radio signal predicted by REAS3 with the radio signal measured by LOPES, 528 events have been selected. The quality cuts applied to the events are listed in table 7.3 of Schröder (2011). In addition, there the details on the analysis of the LOPES events are given. The 528 events include different LOPES set-ups and events reconstructed by KASCADE or KASCADE-Grande. In table 7.2, the detailed numbers of the events for the different set-ups and reconstructions are listed. The events were simulated according to the muon selection presented in the previous section. The hadronic interaction models used for this comparison are QGSJetII (Ostapchenko, 2006) and UrQmd1.3.1 (Bass et al., 1998). Furthermore, each event was simulated for two different types of the primary particle of the air shower, namely proton and iron. Before comparing the output from the simulation with the data obtained with LOPES, a frequency

filter needs to be applied to the simulations since they are performed for the unlimited frequency band and LOPES is measuring only in the effective band of 43-74 MHz. The filtering of the simulations to a finite observing bandwidth is performed with REASPlot (a helper application included in the REAS package, see also section 4.5.1). However, in REASPlot a complete detector simulation is missing. In future, this detector simulation will be performed with “reas2event” (Link et al., 2011a) which is discussed at the end of this section.

As already discussed in section 3.1.6 and (Nehls, 2008), the electric field ϵ of the single antennas as a function of distance R to the shower axis is describable by an exponential function. With the improvement of the analysis of LOPES data, it became clear that the electric field at 100 m ϵ_{100} is better suited as a fit parameter than at the shower core (Schröder, 2011). With this, the exponential function used is

$$\epsilon = \epsilon_{100} \cdot \exp\left(-\frac{R - 100 \text{ m}}{R_0}\right), \quad (7.2)$$

where the fit parameter ϵ_{100} gives the electric field at 100 m axis distance and R_0 denotes the lateral slope of the distribution. Before, with REAS2 and the LOPES 30 set-up, the simulated and measured ϵ_0 and R_0 have been compared where ϵ_0 gives the electric field at the shower core. The results of this comparison are discussed in section 3.1.6 and in (Nehls, 2008) in greater depth. Meanwhile, not only the simulation was improved by including the missing radiation component, but also the quality of the LOPES analysis, e.g. the noise determination and the statistics of the events measured with LOPES increased. For all of the selected events, a number of quality cuts have been applied to the reconstructed lateral distributions. The quality cuts applied are $1 \text{ m} < R_0 < 3000 \text{ m}$ and $1 \mu\text{V/m/MHz} < \epsilon_{100} < 1000 \mu\text{V/m/MHz}$. They are equal to the quality cuts used in (Schröder, 2011; Palmieri, 2011).

Figure 7.7 shows the histograms for the scale parameter R_0 derived by REAS3 and reconstructed with the LOPES data. For the parameter obtained with REAS3, it was distinguished between the proton (lhs) and iron (rhs) induced air showers. For the proton induced air showers, the mean value of R_0 is smaller than for the iron induced showers, and on average, the simulations still predict somewhat steeper slopes than measured with LOPES. The histograms are suggestive of iron induced air showers fitting the data best, but this should be taken with a grain of salt, since the uncertainty on the LOPES reconstruction might influence this result. Comparing this result with former results derived with REAS2 and LOPES data as shown in figure 3.4, it is obvious that REAS3 reproduces the slope parameter R_0 much better. All slope parameters predicted by REAS2 have been less than 100 m, whereas with REAS3 slope parameters around 400 m appear in a few cases. For the first time, it is possible to reproduce also some flat

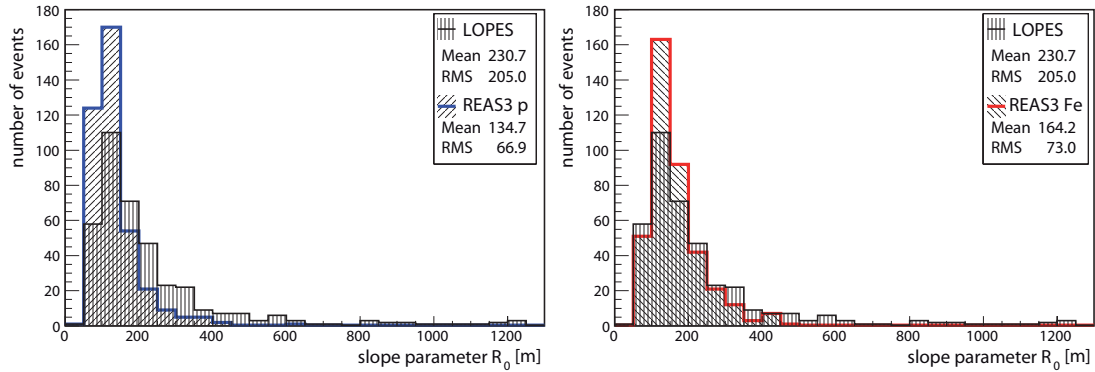


Figure 7.7: Comparison of the scale parameter R_0 derived by REAS3 and reconstructed with LOPES data. For REAS3 each event has been simulated for proton (blue histogram - lhs) and iron (red histogram - rhs) as primary particles. The histograms for the slope reconstructed by LOPES are identical in both figures.

events measured with LOPES without tuning any parameters of the simulation, but only taking the input parameters as provided by KASCADE.

These results should benefit the comparison of the field strengths at different lateral distances as shown in figure 3.5, where the REAS2 simulations predicted too high electric fields for small observer distances and too small electric fields for large observer distances. Figure 7.8 shows this comparison at the same lateral distances as earlier used for REAS2. The results shown here are for proton induced air showers since the former results shown in figure 3.5 are derived for proton induced showers only. The parameters ϵ_0 , ϵ_{75} , ϵ_{150} and ϵ_{225} result from an individual fit per event for each distance for the LOPES data as well as for the REAS3 simulations, i.e. four exponential fits have been performed per event. This explains that the number of events is not equal for the four plots shown in figure 7.8 (and figure 7.9, respectively) since the fit might succeed at a distance close to the core but fail at another distance and vice versa.

At first glance, the field strengths predicted by simulations and measurements agree remarkably well at all distances and not only at 75 m distance to the shower axis. Looking more carefully at the results, it is clear that for larger distances the field strengths predicted by REAS3 are smaller even though less scattered and less shifted than the previous REAS2 results. One explanation is that the measured small field strengths could be overestimated due to the noise at this distance. In figure 7.9, the comparison of the field strengths for the iron induced air showers is shown. The results for iron obtained with REAS3 agree qualitative with the results obtained for proton induced air showers. However, for larger distances, the agreement between simulations and data is better.

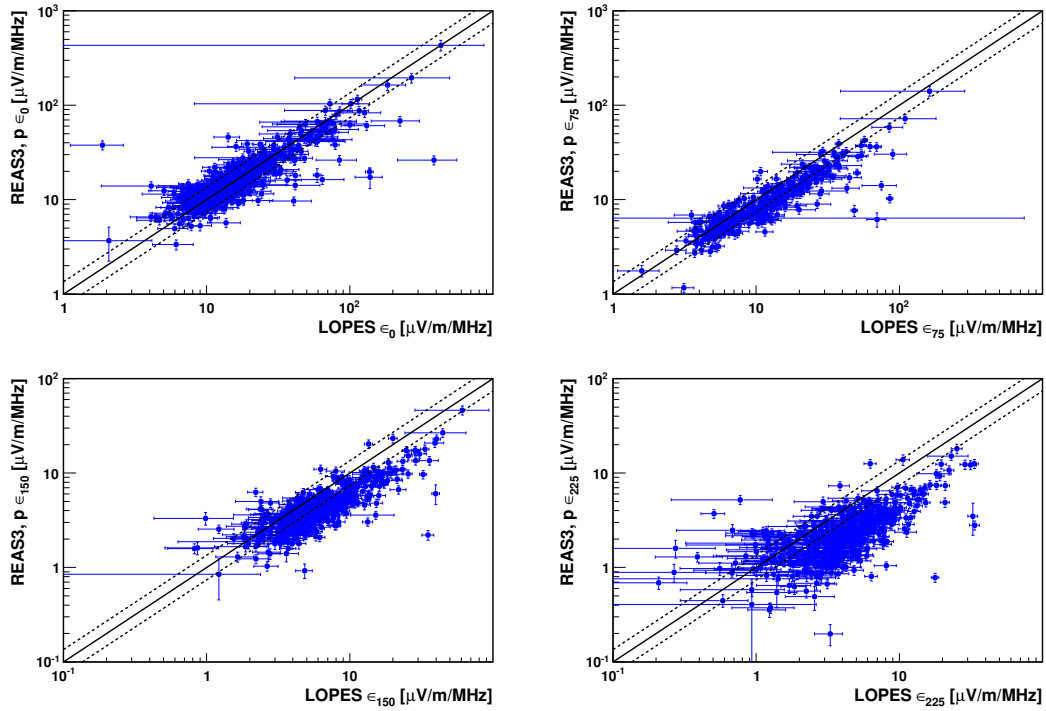


Figure 7.8: Comparison of the field strengths predicted by REAS3 for proton induced air showers with the measured field strength of LOPES at different distances to the shower core. Points on the diagonal would have equal field strengths for simulations and data. The dashed lines give the uncertainty band for the amplitude calibration of LOPES.

At last, it is interesting to look at a comparison of single events. One possibility for such a comparison is to look at the lateral distributions of the radio signal, i.e. the field strength measured with each antenna at different lateral distances from the shower axis. In figure 7.10, three examples of lateral distributions are shown. For the simulations, it is distinguished between the radio signal from proton (lhs in blue) and iron (rhs in red) induced air showers. The scale parameters R_0 and ϵ_{100} as reconstructed for the single events are listed in table 7.3. The grey belt denotes the 35% calibration uncertainty of LOPES (Nehls et al., 2008), the coloured belt denotes the 40% uncertainty on the energy reconstructed with KASCADE (Apel et al., 2010b). The comparison of the lateral distributions results in a classification of three groups of roughly all about the same size. First, there are events which show a very good agreement between the height of the signal and the slope of the lateral distribution function. Second, the slope parameters R_0 predicted by simulations and data match, but the amplitudes do not agree and are shifted mostly to lower values for the simulation. This could be related to the large

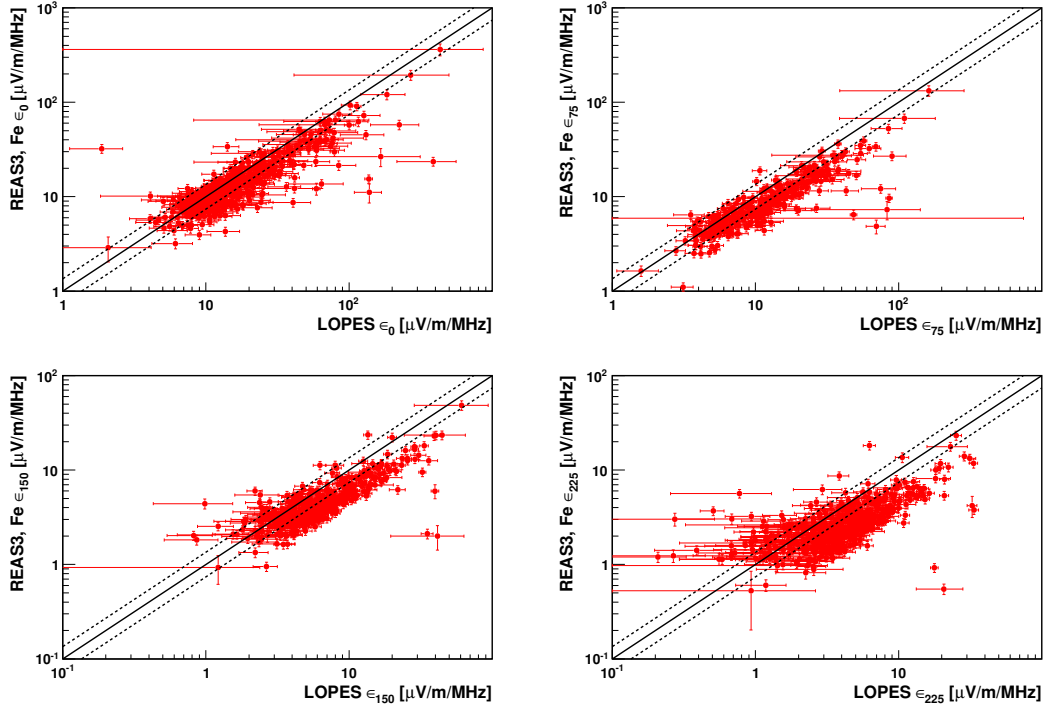


Figure 7.9: Comparison of the field strengths predicted by REAS3 for iron induced air showers with the measured field strength of LOPES at different distances to the shower core. Points on the diagonal would have equal field strengths for simulations and data.

Table 7.3: The parameter R_0 [m] and ϵ_{100} [$\mu\text{V}/\text{m}/\text{MHz}$] for the three events in figure 7.10 as reconstructed from the lateral distributions are listed for the LOPES data, and the REAS3 simulations with proton and iron nuclei as primary particles. The primary energy and the zenith angle of the events are stated in the brackets of the parameters. The order of the events listed matches with the order of the events shown in figure 7.10.

R_0 [m], ϵ_{100} [$\mu\text{V}/\text{m}/\text{MHz}$]	LOPES	REAS3, p	REAS3, Fe
R_0 (0.18 EeV, 25°)	123.2 ± 16.9	126.4 ± 6.4	150.9 ± 8.0
ϵ_{100} (0.18 EeV, 25°)	7.01 ± 0.46	7.25 ± 0.16	6.80 ± 0.12
R_0 (0.29 EeV, 32°)	162.8 ± 59.7	151.6 ± 24.1	222 ± 36
ϵ_{100} (0.29 EeV, 32°)	4.42 ± 0.42	2.50 ± 0.11	2.21 ± 0.07
R_0 (0.19 EeV, 5.7°)	$194.8 \pm 51.3.36$	48.74 ± 2.91	107.2 ± 4.9
ϵ_{100} (0.19 EeV, 5.7°)	6.24 ± 0.43	2.58 ± 0.22	4.75 ± 0.12

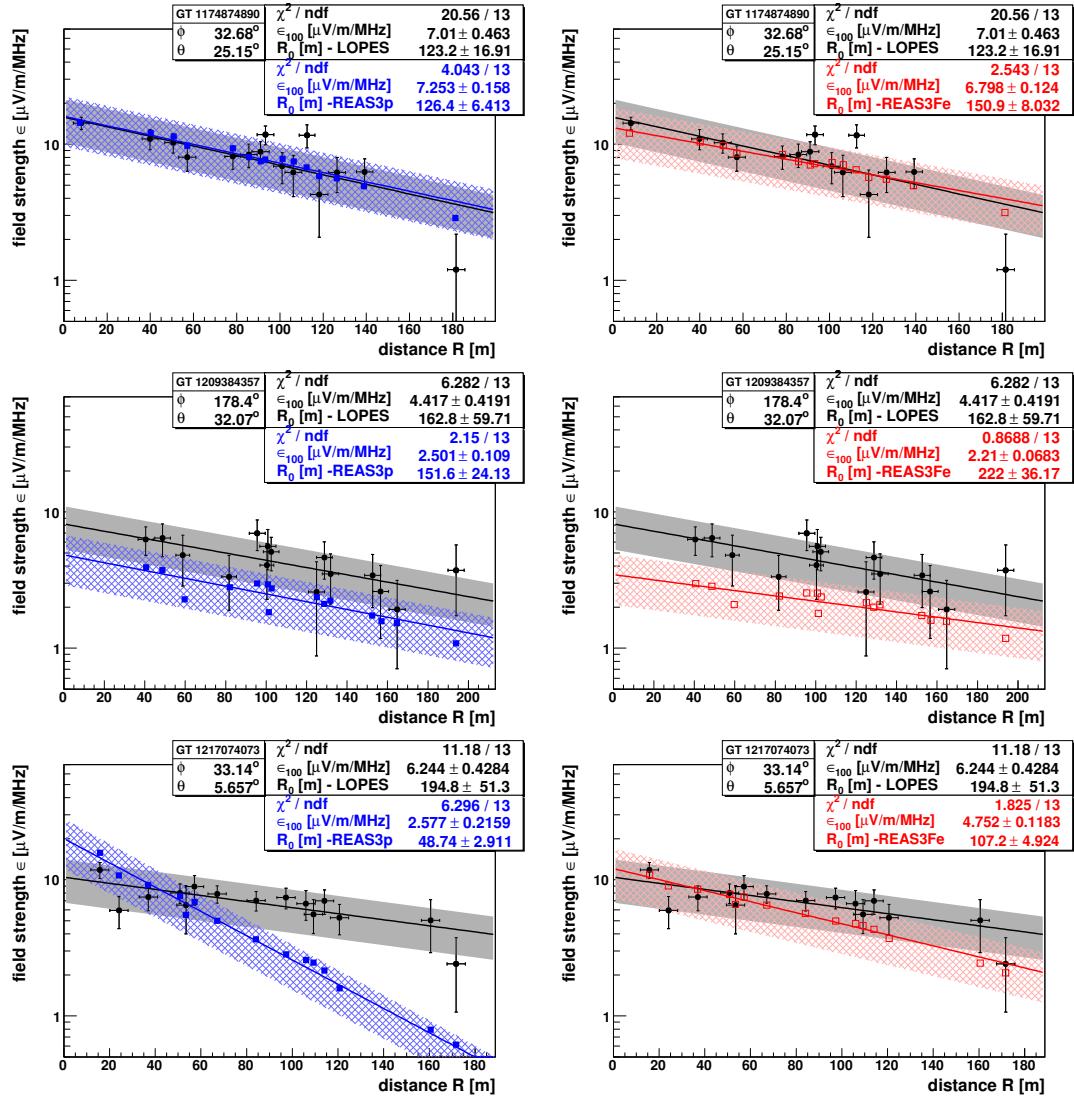


Figure 7.10: Comparison of the lateral distributions simulated by REAS3 for proton (lhs) and iron (rhs) induced air showers with the field strength measured of LOPES. For proton induced air showers, the events are allocable to three different groups: very good agreement, a good agreement in the lateral slope but not in the amplitude and no good agreement in the lateral slope, but the field strengths are acceptable. The influence of the primary particle type is obvious. The grey belt denotes the 35% calibration uncertainty of LOPES, the coloured belt denotes the 40% uncertainty on the energy reconstructed with KASCADE.

uncertainty on the primary energy reconstructed from KASCADE (in the order of 40%). If the energy of KASCADE is overestimated, the measured radio signal

might be too low to be correctly reconstructed and thus, these events might not pass the quality cuts.

In the other case that the energy is underestimated by KASCADE (but still high enough to be selected for the LOPES analyses), the simulations predict smaller amplitudes since they are performed with a smaller energy than the measured air shower had. This results in the observed shift of simulations to lower values.

Another explanation for the shift is the large calibration uncertainty of the LOPES experiment of 35% (Nehls et al., 2008) which would influence the predictions only in one direction, e.g. to lower values for all events. Obviously, these uncertainties are present for the other groups as well.

The third group contains events for which the slope of the lateral distribution is very different for the reconstructions from simulations and data. In most cases of events in this group, the slope parameter predicted by the simulations is smaller. Nevertheless, the predictions on the field strengths differ around a factor of only 2 to 3. One explanation for the differences might be that for REAS3, no detailed detector simulation has been performed. In future, the detector simulation will be possible with the application “reas2event” (Link et al., 2011a). Another possible explanation is that the refractive index of the atmosphere is not yet considered.

Already with these few examples it is shown that the simulations for iron and proton induced air showers vary strongly from event to event and that it thus is important to consider the primary particle type in an event-by-event analysis. In general, the comparison of the lateral distributions and the scale parameters R_0 and ϵ_{100} predicted by REAS3 and reconstructed with LOPES data show a good agreement and thus illustrate the improved understanding of the radio emission from air showers. Even so, a few questions are left. For further improvements of the comparison between simulations and data, it is necessary that the simulations are processable with the same analysis software as the data and that noise can be added to the simulations. In the near future, this will be possible with “reas2event”. With this, the cross-correlation-beam⁶ can be calculated for the simulations and more detailed comparisons of simulations and data are realisable, in particular those which depend on the cross-correlation beam.

To conclude, within the bounds of uncertainties (mainly the primary energy estimated by KASCADE and the calibration uncertainties of LOPES), REAS3 is mostly able to describe the data. Since LOPES was built as a prototype experiment, the quality of the data is not optimized and hence it is neither possible to verify nor to rebut the predictions by REAS3 definitely. With data taken by LOFAR and AERA, this situation will change. Within LOFAR, a lot of antennas will provide high-quality data even though LOFAR is not combined with an

⁶The cross-correlation-beam indicates the coherence of a signal in the individual antennas and is used for many analyses of LOPES.

air shower experiment such as LOPES. AERA will probe radio emission from air showers at energies of up to 10^{19} eV and has been optimized for good data quality.

In these days, the first coincident events of AERA with the surface detectors were recorded and simulations of REAS3 were processed for comparison. Even a “super-hybrid” event detected by the fluorescence telescopes, the surface detectors and the radio antennas has been reconstructed. This increases the need of top-down simulations as now possible with CORSIKA and REAS3 and the importance of a detailed simulation of radio emission from air showers as provided by REAS3.

A universal endpoint formalism

In the previous chapters, we showed that with the implementation of the endpoint formalism in REAS3, radio emission from cosmic ray air showers is calculated in a self-consistent way. The endpoint formalism helped significantly to increase the understanding of the measured data as shown in chapter 7 by comparing REAS3 with LOPES data. Aside from calculating radio emission from air showers with this formalism it became clear that it can be of general use. Hence, in this chapter, this approach is generalized to a universal formalism for the calculation of electromagnetic radiation from accelerated charged particles. The development of this approach led to a publication, see James et al. (2010).

The real strength of the endpoint formalism emerges when regarding the complexity of real situations such as calculating the radio emission from air showers. In this case, it is hardly possible to separate all different radiation processes into “classical” descriptions such as synchrotron radiation, Cherenkov emission or transition radiation and combine them again self-consistently. For example, as shown in chapter 4, calculating the synchrotron emission along the particle trajectories and combining it with the emission contributions due to the starting and the stopping of the particle is precarious. It has to be considered that the momentum direction from the starting- and stopping-point of the particle changed and that this change is already included in the synchrotron calculation. Such delicate issues will appear as long as complex and thus realistic situations are tried to be separated into different “mechanisms”. However, in chapter 4, we already showed that the endpoint formalism is ideal for describing radio emission with Monte-Carlo-simulations such as REAS3.

Within the limits of classical electrodynamics, the endpoint formalism is a universal method to calculate the radiation due to acceleration of charged particles.

With this precise and intuitive interpretation of radiation processes as superposition of individual, instantaneous acceleration events, the electromagnetic fields can be calculated in either the time- or the frequency-domain. The choice of the domain in which the endpoint-calculation is executed depends on the domain of the desired result¹. The only exception to this rule is when dispersive effects (changing refractive index with frequency) become important, in which case frequency-domain calculations would be more practical.

In this chapter, we show that with the endpoint formalism it is possible to reproduce the results from classical synchrotron radiation correctly (section 8.3). Thanks to the collaboration with Clancy W. James and Heino Falcke, we could show that the endpoint formalism is also applicable for the frequency-domain as presented in section 8.2.2. Since the Liénard-Wiechert potentials build the basis of the endpoint formalism, they are introduced in section 8.1. Moreover, the universality and the convenience of the endpoint approach is emphasized throughout the complete chapter.

8.1

Liénard-Wiechert potentials

In order to show the universality of the endpoint approach, its derivation is based on the Liénard-Wiechert potentials which lead to the electric field from charged particle motion. The Liénard-Wiechert potentials as given in equation 8.1 are derived directly from Maxwell's equations in the relativistic case²:

$$\Phi(\vec{x}, t) = \left[\frac{e}{(1 - n\vec{\beta} \cdot \vec{r})R} \right]_{\text{ret}} \quad \text{and} \quad \vec{A}(\vec{x}, t) = \left[\frac{e\vec{\beta}}{(1 - n\vec{\beta} \cdot \vec{r})} \right]_{\text{ret}} \quad (8.1)$$

where $q = \pm e$ denotes the particle charge, $R(t) = |\vec{R}(t)|$ is the distance from the particle to an observer position, n describes the refractive index at the particle position, $\vec{r}(t) = \vec{R}(t)/R(t)$ is the line-of-sight direction between particle and observer and $\vec{\beta} = \vec{v}(t)/c$ is directly given by the particle velocity $\vec{v}(t)$. The index “ret” means that the equation needs to be evaluated in retarded time $t' = t - nR(t)/c$. The electromagnetic emission of particles using the vector potentials of equation

¹Since the fast-Fourier transformation between time- and frequency-domain needs many points in the first domain to calculate a precise result in the second domain, the computing time is smaller if the calculations are performed independently in the time- and the frequency-domain. This was the case for the example of synchrotron radiation which is discussed in section 8.3.

²For a derivation for $n = 1$, see e.g. Jackson (1975). Using an arbitrary n produces the result for equation 8.3 from Zas et al. (1992) in the case where the relative permeability, μ_r , is unity.

8.1 is derived by calculating the electric field as:

$$\vec{E}(\vec{x}, t) = -\nabla\Phi(\vec{x}, t) - \dot{\vec{A}}(\vec{x}, t) \quad (8.2)$$

Two methods exist to evaluate equation 8.2 for the calculation of the electric field. First, the potentials are calculated from a distribution of source charges and the contributions from individual charges in the distributions are summed up. Following equation 8.2, the vector potentials will give the desired electric field (see e.g. Alvarez-Muñiz et al. (2010)).

In the second method, as used in this thesis, the electric field is calculated from the Liénard-Wiechert potentials using the relation given in equation 8.2. For a particle with Lorentz factor γ the electric field in a dielectric, non-magnetic medium is then:

$$\vec{E}(\vec{x}, t) = q \left[\frac{\vec{r} - n\vec{\beta}}{\gamma^2(1 - n\vec{\beta} \cdot \vec{r})^3 R^2} \right]_{\text{ret}} + \frac{q}{c} \left[\frac{\vec{r} \times [(\vec{r} - n\vec{\beta}) \times \dot{\vec{\beta}}]}{(1 - n\vec{\beta} \cdot \vec{r})^3 R} \right]_{\text{ret}}, \quad (8.3)$$

where the first term is the “static” near-field term (velocity field) and the second the “radiation” term. Since the radiation term is dependent on the time-derivative of $\vec{\beta}$, it is obvious that accelerated charges lead to emission contributions. In the following, the near-field term will be neglected because the “radiation” term completely dominates the signal for distances R relevant in practical applications.

To calculate the electric field arising due to an arbitrary radiation process, we consider individual, instantaneous acceleration events which are superposed subsequently. In the next section, the general idea of the endpoint formalism is discussed on the basis of the radiation from one single endpoint. In section 8.3, the application of the endpoint formalism is shown for the case of synchrotron radiation.

8.2

Radiation from one endpoint

Before the endpoint formalism is applied to any complex situation, the instantaneous acceleration of one single particle has to be calculated. The single particle gets accelerated from rest at time $t' = t'_0$ to a velocity $\beta = \beta^*$, i.e. $\dot{\beta} = \beta^* \delta(t' - t'_0)$, or equivalently gets decelerated from a velocity $\beta = \beta^*$ to rest ($\dot{\beta} = -\beta^* \delta(t' - t'_0)$). We define the electric field resulting from an acceleration as \vec{E}_{\pm} , where the acceleration vector $\dot{\vec{\beta}}$ can either be parallel (+) or anti-parallel (−) to the velocity vector $\vec{\beta}$, corresponding respectively to acceleration or deceleration. We proceed to derive \vec{E}_{\pm} from the radiation term of equation 8.3 in terms of the ‘lab-time’ t in the time- and frequency-domain. Similar derivations in both domains in the case of linear particle tracks (effectively two endpoints) appear also in Alvarez-Muñiz

et al. (2010), for the case of Cherenkov radiation: note that in the following, no assumption on the nature of the radiation needs to be made.

8.2.1

The time-domain derivation

The time-domain derivation was already used to describe the radio emission from air showers and has been implemented in REAS3 as described in chapter 4. In this chapter, a short review is given for consistency.

For the time-domain derivation, the radiative component of equation 8.3 is considered. The time-integral of the electric field is calculated for one starting-point or stopping-point, taking into account the conversion from retarded emission time t' to observer-time t as $t = t' + nR/c$ and $dt = dt'(1 - n\vec{\beta} \cdot \vec{r})$, via:

$$\begin{aligned} \int \vec{E}(\vec{x}, t) dt &= \frac{q}{c} \int_{\Delta t} \left[\frac{\vec{r} \times [(\vec{r} - n\vec{\beta}) \times \dot{\vec{\beta}}]}{(1 - n\vec{\beta} \cdot \vec{r})^3 R} \right]_{\text{ret}} dt \\ &= \pm \frac{q}{c} \left(\frac{\vec{r} \times [\vec{r} \times \vec{\beta}^*]}{(1 - n\vec{\beta}^* \cdot \vec{r}) R} \right) \end{aligned} \quad (8.4)$$

Here, $\Delta t = t_1 - t_0$ denotes the observer-time window corresponding to the retarded-time window $\Delta t' = t'_1 - t'_0$, which covers the acceleration process. For a starting-point (+ sign), the particle is at rest at the time t'_0 and has velocity $\vec{\beta}^*$ at t'_1 . The opposite is the case for a stopping-point (− sign).

Since the acceleration is instantaneous, the distance R_{acc} from the particle to the observer at the acceleration time is constant, and the time t_{acc} at which an observer would view the radiation emitted at time t'_{acc} is given by $t_{\text{acc}} = t'_{\text{acc}} + nR_{\text{acc}}/c$. The time window $\Delta t = t_1 - t_0$ in equation 8.4 is therefore chosen to satisfy $t_0 < t_{\text{acc}} < t_1$.

While the electric field $\vec{E}(\vec{x}, t)$ as a function of time becomes infinite in the case of instantaneous acceleration, the time-integrated electric field is finite and independent of the specific choice of Δt . Consequently, one can calculate the time-averaged electric field over the time-scale Δt as

$$\vec{E}_{\pm}(\vec{x}, t) = \pm \frac{1}{\Delta t} \frac{q}{c} \left(\frac{\vec{r} \times [\hat{r} \times \vec{\beta}^*]}{(1 - n\vec{\beta}^* \cdot \vec{r}) R} \right). \quad (8.5)$$

An adequate choice of Δt is dictated by the time resolution of interest. If Δt is chosen significantly longer than the time-scale over which the acceleration process occurs — which is in particular the case for the instantaneous acceleration considered here — the details of the acceleration process are of no importance.

8.2.2

The frequency-domain derivation

For the frequency-domain calculation, the basis is the same as for the time-domain derivation, i.e. the radiation term from equation 8.3. The frequency-domain calculation was not used in this thesis so far. It has been derived by C.W. James for the collaborative work on the publication in James et al. (2010), whereas we contributed with the time-domain derivation. Nonetheless, it is discussed for completeness in this chapter since a comparison of the time- and frequency-domain results will show that they give the same results and there are situations where a frequency-domain treatment is preferable.

For instantaneous acceleration at an endpoint, $\vec{\beta}$ is parallel to $\dot{\vec{\beta}}$ which means that the $\vec{\beta} \times \dot{\vec{\beta}}$ term from equation 8.3 vanishes:

$$\vec{E}_{\pm}(\vec{x}, t) = \pm \frac{q}{c} \left[\frac{\vec{r} \times [\vec{r} \times \vec{\beta}^* \delta(t' - t'_0)]}{(1 - n\vec{\beta} \cdot \vec{r})^3 R} \right]_{\text{ret}} \quad (8.6)$$

First of all, the Fourier-transform of equation 8.6 is taken and using the conversion from retarded time t' to observer time as for the time-domain derivation, i.e., $t = t' + Rn/c$ and $dt = dt'(1 - n\vec{\beta} \cdot \vec{r})$:

$$\begin{aligned} \vec{E}_{\pm}(\vec{x}, \nu) &= \int dt \vec{E}_{\pm}(\vec{x}, t) e^{2\pi i \nu t} \\ &\equiv \int dt' \vec{E}_{\pm}(\vec{x}, t(t')) (1 - n\vec{\beta} \cdot \vec{r}) e^{2\pi i \nu (t' + Rn/c)}. \end{aligned} \quad (8.7)$$

For the frequency-domain derivation, a conceptual and mathematical challenge is that at the time of acceleration, β , and hence $\vec{E}_{\pm}(\vec{x}, \nu)$, is undefined. However, the integral can be solved, since the acceleration lasts a finite (but small) time interval $\Delta t'$ with the limit of $\Delta t' \rightarrow 0$.

With $t'' = t' - t'_0$, the acceleration takes place over the interval $0 < t'' < \Delta t'$, where $\beta(t'') = \beta^* t'' / \Delta t'$, $\dot{\vec{\beta}} = \beta^* / \Delta t'$, and $R(t'') = R - 0.5c(\beta^* / \Delta t') t''^2 \vec{\beta} \cdot \vec{r}$. With this, the integral becomes:

$$\vec{E}_{\pm}(\vec{x}, \nu) = \pm \lim_{\Delta t' \rightarrow 0} \frac{q}{c} e^{2\pi i \nu t'_0} \times \int_0^{\Delta t'_0} \frac{\frac{1}{\Delta t'_0} e^{2\pi i \nu (t'' + nR(t'')/c)}}{(1 - \frac{nt''}{\Delta t'} \vec{\beta}^* \cdot \vec{r})^2 R(t'')} (\vec{r} \times [\vec{r} \times \vec{\beta}^*]) dt'' \quad (8.8)$$

For the limit of $\Delta t' \rightarrow 0$ the integral gets simplified to the following form:

$$\vec{E}_{\pm}(\vec{x}, \nu) = \pm \frac{q}{c} \frac{e^{ikR}}{R} \frac{e^{2\pi i \nu t'_0}}{1 - n\vec{\beta}^* \cdot \vec{r}} \vec{r} \times [\vec{r} \times \vec{\beta}^*] \quad (8.9)$$

As in the previous section, the ‘ \pm ’ is positive when the acceleration is parallel to the motion (acceleration from rest), and negative when the acceleration is anti-

parallel to the motion (acceleration to rest).

Note, that in calculating equations 8.5 and 8.9 no assumptions about the macroscopic motion of the particles have been made. The only information used in the derivations was that at a given instant, the particle became accelerated. Hence, the results given for a radiating endpoint are not only a special case of particle motion with very limited application. In James et al. (2010), it is shown how arbitrary particle motion can be described in terms of such an endpoint approach. In the following section the radiation from a single endpoint is discussed and in section 8.3 the use for physical theories is shown using the example of synchrotron radiation.

8.2.3

Building physical situations

In the previous sections, equations 8.5 and 8.9 were derived as the result of a particle accelerated from rest or to rest. In fact, these equations represent more than only this special acceleration events. Each arbitrary acceleration of a particle can be regarded as a superposition of two of these events, an acceleration and a deceleration process. The electric field does not cancel even if these events take place at the same position. Since the velocity, and hence $\vec{\beta}$, differ in either the direction or in the value, the superposition of deceleration and acceleration will not cancel.

More precisely, for a particle moving on a curved trajectory with a constant velocity, the direction of the velocity will change between the endpoint of the deceleration event and the endpoint of the acceleration event. This relation was already used in REAS3 to describe the radiation in the kinks of the particle trajectories which are curved due to the deflection in the Earth's magnetic field (cf. section 4.2). On the contrary, for gradually accelerating/decelerating particles, not the direction of the velocity will change but the values will be different for the two endpoints at the same place.

In each case, contributions from starting and stopping points will not cancel, and radiation will occur. Superposition of endpoints in this way is sometimes viewed as destroying the 'old' particle and creating a 'new' one. Consequently, for a particle which is moving with constant velocity, i.e. no change of $\vec{\beta}$ in neither the direction nor the amplitude, the radiation of an acceleration and deceleration event will vanish at the same place when the motion is described piece-wise as a series of endpoints. Hence, a particle following a simple linear motion does not radiate which is in agreement with classical electrodynamics.

Each arbitrary change in the particle velocity can be handled by combining two simultaneous, coincident endpoints, the first to 'stop' the particle by bringing it from its old velocity to rest, the second to 'start' the particle by accelerating it to its new velocity. Multiple particles/events can be treated by adding the

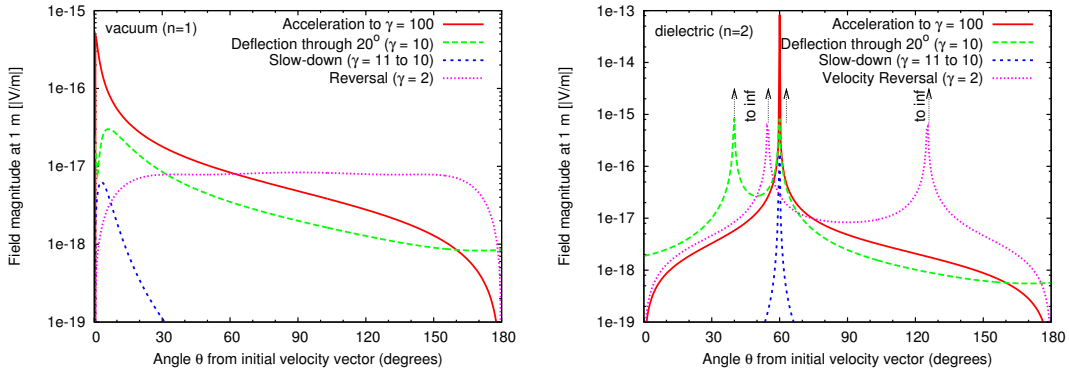


Figure 8.1: The emitted radiation of a relativistic electron in four elementary cases as described in the text. Left: in vacuum, and right: in a medium with $n = 2$ (James et al., 2010).

contributions with appropriate $\vec{\beta}$, R , n , and t_0 . Any propagation effects between the source and the observer as, e.g., absorption in a medium or transmission through an interface should be applied to the radiation from each endpoint. This can be solved, since the relevant parameters are well defined and unique for each endpoint. Note that for ray-tracing methods, the rays will be diverging, and transmission problems should be handled accordingly.

In Figure 8.1, the electric field magnitude resulting from the acceleration of a relativistic electron in four different situations is shown, each for vacuum and a dielectric with refractive index $n = 2$: a single endpoint representing an electron accelerating from rest (‘acceleration’ – solid red line); the deflection of an energetic electron through 20° (‘deflection’ – long dashed green line); the deceleration of a fast electron (‘slow-down’ – short dashed blue line); and a reversal of direction of a mildly relativistic electron with no change in speed (‘reversal’ – dotted pink line). Note in the three highly relativistic cases the characteristic beaming in the forward direction in the vacuum case and about the Cherenkov angle $\theta_C = \cos^{-1}(1/(\beta n))$ in the $n = 2$ dielectric. For velocity reversal, significant peaks are observed at the Cherenkov angle since $\beta n > 1$, while in the vacuum case, no appreciable beaming is evident and the emission is broad, which is characteristic of (non-relativistic) dipole radiation.

The four examples illustrated in figure 8.1 are all point-like acceleration events. For most real situations, however, the particle motion will be smooth. Nevertheless, this is not a limitation in practice, since every numerical simulation describes a series of uniform motions joined by instantaneous acceleration events, for which either equation 8.5 or equation 8.9 will calculate the emitted radiation exactly. Given that the degree to which the radiation is calculated with such endpoint contributions resembles the real radiation, this is limited only by the degree to

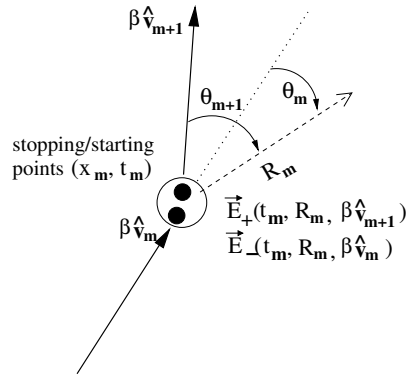


Figure 8.2: Sketch of the contributions from a stopping- and a starting-point for calculating synchrotron radiation as given in equation 8.10 (James et al., 2010).

which the simulated motion resembles the true motion. Moreover, this means that a particle simulator must be accurate to within a small fraction of the wavelengths of interest. A discussion of this effect in practice is given in Alvarez-Muñiz et al. (2000). In the following section, it is shown how to reproduce the classical result of synchrotron radiation using the endpoint formulation to show that the frequency- and time-domain calculations give the same results.

8.3

Application to established theory

Synchrotron radiation arises from a relativistic particle undergoing infinite helical motion (a superposition of circular motion in a 2D plane and linear motion perpendicular to the plane) in a vacuum ($n = 1$), as is typically induced by the presence of a uniform magnetic field. Here, we treat the case of a particle with velocity β executing a single circular loop of radius L in the $x - y$ plane only in a vacuum. This motion is viewed by an observer at a very large distance R in direction \vec{r} . Such motion can be represented by a series of N starting and stopping points as follows:

$$\sum_{m=0}^{N-1} \vec{E}_+(t_m, R_m, \beta \vec{v}_{m+1}) + \vec{E}_-(t_m, R_m, \beta \vec{v}_m), \quad (8.10)$$

where the calculation of each velocity unit vector \vec{v}_m , time t_m , and distance R_m to the observer is a matter of simple geometry. While the $1/R_m$ term can be assumed constant, R_m also changes the relative phase-factors between emission at different endpoints. This is shown schematically in Figure 8.2. Each starting-point always has a corresponding stopping-point at the same position. Although they are located at the same position, i.e. the distance to the observer R_m and the

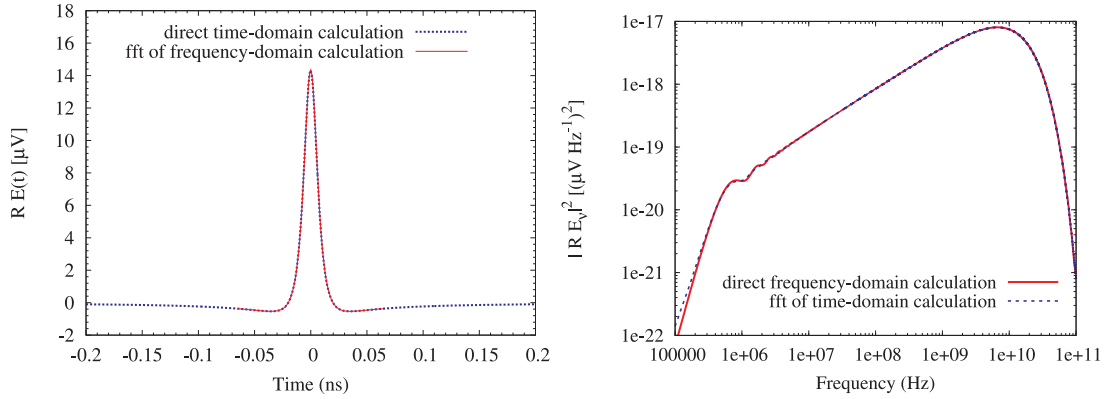


Figure 8.3: Left: the time-trace of a synchrotron pulse of an electron moving on a single loop with $\beta = 0.999$ and an radius $r = 100$ m. Right: the power spectrum of the same pulse shown on the lhs. For both cases, the direct calculations are compared with the fast-Fourier-transformation of the other domain (James et al., 2010).

time t_m are the same, the contributions of both do not cancel, since the direction of the velocity vectors $\beta\vec{v}$ differ. It has to be paid attention that the initial starting point has the a corresponding final stopping point, i.e. the number of particles is kept constant for the whole situation. Otherwise the initial starting and final stopping terms would dominate the desired synchrotron radiation terms from the circular motion. Hence, with equation 8.10 the physical situation is equivalent to an already existing particle with uniform motion which is executing a loop once as described above and afterwards still existing but moving on a straight line with constant velocity in the same direction as before the loop. This ensures that the particle is before and after the loop not radiating and the result gives the pure synchrotron term. Looking at equation 8.10 it appears that there is exactly one term with $\beta\vec{v}_0$ for $m = 0$ (a stopping event) and $\beta\vec{v}_N$ for $m = N - 1$ (a starting event) and exactly two terms for $0 < m < N - 1$ (one starting and one stopping event).

Figure 8.3 shows the numerical evaluations of equation 8.10 for an electron with $\beta = 0.999$ ($\gamma \approx 22.4$) moving on a loop of radius 100 m. This is equivalent to an electron with energy 11.4 MeV in a magnetic field of 3.809 Gauss perpendicular to the direction of motion. The observer is assumed to lie in the very-far-field in the plane of the loop. For the time-pulse as well as for the frequency spectra, a direct calculation has been made using equations 8.5 and 8.9, respectively. The results from the time- and frequency-domain calculations have then been fast-Fourier-transformed. Hence, the direct calculation of the time-domain could be compared with the Fourier-transformed result of the frequency-domain, and vice versa.

The expected characteristics are reproduced by both: a steep spectral fall below the cyclotron frequency ($\nu = 2\pi L(\beta c)^{-1}$), and a slow rise in power until an exponential cut-off above the critical frequency $\nu_{\text{crit}} = 1.5\gamma^3\beta c/L \approx 50$ GHz. In the time-domain, a sharp pulse of characteristic width $1/\nu_{\text{crit}}$ is seen. That the results calculated by Fourier transform do not exactly match the direct calculations is due to the difficulty in generating sufficient data to make an accurate transform. However, the correspondence is obvious. Integrating the power radiated over all angles reproduces the better-known synchrotron power spectrum, as appears in standard textbooks such as Jackson's 'Classical Electrodynamics' (Jackson, 1975).

In James et al. (2010), the endpoint formalism is used additionally to reproduce the results of Vavilov-Cherenkov radiation and transition radiation. Since the focus of this thesis is the radio emission of cosmic ray air showers, these two situations are not discussed here.

8.4

Discussion of the endpoint formalism

As already mentioned, there are also limitations of the endpoint formalism as e.g. its classical foundation in Maxwell's equations: it breaks down in any quantum-mechanical limit. Neither radiation processes involving only a single photon can be treated, nor the radiation of extremely energetic photons. Nevertheless, these limitations are common to all classical methods of treating radiation and are not increased by this approach. Furthermore, like any method using a distribution of sources, the accuracy of the endpoint method will reflect the accuracy with which the distribution of endpoints reflects the true particle motion on scales of the highest time resolution (smallest wavelength) of interest. Even so, radiation can be calculated with the endpoint formalism in very complex physical situations, taking the accuracies into account. This is obvious regarding the complexity of air shower physics and the possibility to calculate radio emission from air showers with the endpoint methodology (cf. chapter 4). Some other examples are presented in James et al. (2010).

The second limitation is that the 'near-field' term from equation 8.3 is not considered. This implies not that with the endpoint approach it is impossible to calculate radiation in the near-field of a source distribution. Since each endpoint is point-like, any observer is always in the far-field of any particular endpoint. Thus a near-field calculation requires mostly to re-calculate the direction to the observer from each endpoint individually. Only in certain special circumstances, such as the case of Vavilov-Cherenkov radiation from non-accelerated systems, the near-field term will provide a significant contribution to the observed electric fields. In general, this near-field term will only become important when a large part of the charge distribution passes very close to the detectors, and for most

experiments it will represent at most a minor correction only. Above all, the near-field contribution is negligible for the calculation of radio emission from cosmic ray air showers.

To summarise, with the endpoint formalism all radiation from particle acceleration can be described in terms of superposition of instantaneous acceleration events and this with only one single formula. This formalism gives a general methodology for applying this method to an arbitrary (complex) problem. One complex but realistic problem is the calculation of radio emission from extensive air showers. With the endpoint formalism, this problem can be solved in a self-consistent way without the need of taking different “radiation contributions” (such as synchrotron, the variation of transverse currents, the variation of the number of charged particles, etc.) separately into account. This is a real advantage since the different “radiation processes” in an air shower can not be separated easily and combined self-consistently again afterwards. The details on the implementation of the endpoint formalism in REAS3 and its consequences in the understanding of air shower radio emission were discussed in the previous chapters of this thesis.

CHAPTER 9

Conclusion

In the last years, the detection of radio emission from air showers made tremendous progress and is starting to be applied on much larger scales than the previously running experiments. Therefore, a detailed understanding of the emission process is needed more than ever. Aim of the present work was the improvement of this theoretical understanding. Before the start of this work, different models simulating the radio emission from air showers made conflicting predictions in particular on the shape (unipolar vs. bipolar) and the amplitude of the pulses.

Nowadays, it is clear that the models predicting unipolar pulses missed a radiation component caused by the variation of the number of charged particles in an air shower. Among these models was also the radio simulation code REAS2. Within the scope of this work, the following results have been achieved:

- We developed a method to include the missing radiation component in a self-consistent way in REAS3. With the endpoint formalism, it is guaranteed that all processes leading to radio emission are considered without making any assumptions or approximations. Many existing models can now easily be revised according to the lessons learned with REAS3.
- With a detailed study on the pulse shape, we understood in which way particles of the air shower contribute to the overall radio signal.
- We showed with the comparison of REAS3 and the model MGMR that for the first time, two independent and complementary simulation approaches obtain similar results. Only at small observer distances, the results differ by a factor of 2-3. Hence, we discussed the influence of the underlying air shower and atmosphere models and the parametrisations of MGMR.

- For the comparison of REAS3 simulations with LOPES data, we developed a new methodology to select an air shower for the consideration of shower-to-shower fluctuations which is of interest for all air shower experiments. In case of LOPES, the shower selection is based on the number of muons measured by KASCADE and enables the one-to-one comparison between simulated and measured air showers and their radio emission. We achieved a strongly improved agreement with respect to earlier comparisons between REAS simulations and LOPES data. REAS3 predicts comparable lateral slopes and - even more impressive - comparable amplitudes as LOPES measures without relying on any free parameters.
- Due to the universality and the didactic quality of the endpoint formalism developed within the scope of the present thesis, we showed that the formalism provides a universal tool which can be relevant for scientists in various fields.

In summary, with this work and in particular with REAS3, we increased enormously the understanding of the radio emission from air showers. The comparison with LOPES data, however, is limited by the uncertainties on the the amplitude calibration of LOPES and the high noise level at the KIT. Therefore, comparisons with data of higher quality are needed. These high quality events will come with AERA and LOFAR, both are currently taking first data.

No more than a month ago, first coincidences between AERA and the surface detectors, and even one “super-hybrid” event with the particle detectors, the radio antennas and the fluorescence telescopes were recorded. This increases the merit of “top-down” simulations and the importance of a detailed simulation of radio emission from air showers. Both, we developed in the scope of this work. Moreover, REAS3 is used to study cosmic ray events detected by ANITA (Hoover et al., 2010), a balloon experiment at the south pole searching for neutrinos.

We also showed that the refractive index of the atmosphere influences the radio emission from air showers, in particular the arrival times. For further analysis, a realistic refractive index of the atmosphere should be considered in the simulation approaches.

Furthermore, it needs to be studied if information gets lost due to the histogramming of the air shower. To investigate this, the endpoint formalism will be implemented directly in CORSIKA. The results of REAS3 might also change with the improvement of the high-energy hadronic interaction models. With comparisons between the interaction models and LHC data at higher energies, the models are being tested and revised where appropriate.

With the usability of the endpoint theory, the link to other fields of research is possible. Thus, the present work enriches not only the field of radio detection from cosmic ray air showers, but also the modelling of electromagnetic radiation processes in other fields of research.

Bibliography

- Abraham, J. et al. (Pierre Auger Collaboration) (2010a). *Measurement of the Depth of Maximum of Extensive Air Showers above 10^{18} eV*. Phys. Rev. Lett., 104 (9): 091101. doi:10.1103/PhysRevLett.104.091101.
- Abraham, J. et al. (Pierre Auger Collaboration) (2010b). *The fluorescence detector of the Pierre Auger Observatory*. Nuclear Instruments and Methods in Physics Research Section A: Accelerators, Spectrometers, Detectors and Associated Equipment, 620 (2-3): 227 – 251. doi:DOI:10.1016/j.nima.2010.04.023.
- Allan, H. R. (1971). *Radio Emission From Extensive Air Showers*. Prog. in Element. part. and Cos. Ray Phys., Vol. 10: 171–302.
- Allard, D. et al. (2005). *UHE nuclei propagation and the interpretation of the ankle in the cosmic-ray spectrum*. Astronomy & Astrophysics, 443 (3): L29–L32. doi:10.1051/0004-6361:200500199.
- Alvarez-Muñiz, J., Carvalho, Jr, W. R., Tueros, M. and Zas, E. (2010). *Coherent Cherenkov radio pulses from hadronic showers up to EeV energies*. [arXiv:1005.0552](#).
- Alvarez-Muñiz, J., Vázquez, R. A. and Zas, E. (2000). *Calculation methods for radio pulses from high energy showers*. Phys. Rev. D, 62: 63001–+. doi:10.1103/PhysRevD.62.063001.
- Alvarez-Muñiz, J., Romero-Wolf, A. and Zas, E. (2010). *Čerenkov radio pulses from electromagnetic showers in the time domain*. Phys. Rev. D, 81 (12): 123009. doi:10.1103/PhysRevD.81.123009.
- Anderson, C. D. (1933). *The positive electron*. Phys. Rev., 43 (6): 491–494. doi:10.1103/PhysRev.43.491.

- Antoni, T. et al. (KASCADE Collaboration) (2003). *The Cosmic-Ray Experiment KASCADE*. Nucl. Instr. Meth. A, 513 (3): 490–510.
- Antoni, T. et al. (KASCADE Collaboration) (2005). *KASCADE measurements of energy spectra for elemental groups of cosmic rays: Results and open problems*. Astroparticle Physics, 24 (1-2): 1–25. doi:DOI:10.1016/j.astropartphys.2005.04.001.
- Apel, W. D. et al. (LOPES Collaboration) (2006). *Progress in air shower radio measurements: Detection of distant events*. Astropart. Physics, 26: 332–340. doi:10.1016/j.astropartphys.2006.07.003.
- Apel, W. D. et al. (KASCADE Collaboration) (2009). *Energy Spectra of Elemental Groups of Cosmic Rays: Update on the KASCADE Unfolding Analysis*. Astropart. Phys., 31: 86–91.
- Apel, W. D. et al. (LOPES Collaboration) (2010a). *Lateral distribution of the radio signal in extensive air showers measured with LOPES*. Astropart. Phys., 294–303.
- Apel, W. D. et al. (KASCADE Collaboration) (2010b). *The KASCADE-Grande experiment*. Nucl. Instr. Meth. A, 620: 202–216.
- Apel, W. D. et al. (KASCADE Collaboration) (2010c). *The spectrum of high-energies cosmic rays measured with KASCADE-Grande*. Astropart. Phys., submitted.
- Apel, W. D. et al. (LOPES Collaboration) (2011). *Thunderstorm Observations by Air-Shower Radio Antenna Arrays*. Advances in Space Research, in press. doi:10.1016/j.asr.2011.06.003.
- Ardouin, D. et al. (CODALEMA Collaboration) (2005). *Radio-detection signature of high-energy cosmic rays by the CODALEMA experiment*. Nucl. Instr. Meth. A, 555: 148–163. doi:10.1016/j.nima.2005.08.096.
- Ardouin, D. et al. (CODALEMA Collaboration) (2006). *Radioelectric field features of extensive air showers observed with CODALEMA*. Astropart. Physics, 26: 341–350. doi:10.1016/j.astropartphys.2006.07.002.
- Ardouin, D. et al. (TIANSHAN Collaboration) (2010). *The TIANSHAN Radio Experiment for Neutrino Detection*. ArXiv e-prints - submitted to Astroparticle Physics. [1007.4359](#).
- Arqueros, F., Hörandel, J. and Keilhauer, B. (2008). *Air fluorescence relevant for cosmic-ray detection—Summary of the 5th fluorescence workshop, El Escorial 2007*. Nuclear Instruments and Methods in Physics Research Section A:

- Accelerators, Spectrometers, Detectors and Associated Equipment, 597 (1): 1 – 22. doi:DOI:10.1016/j.nima.2008.08.056. Proceedings of the 5th Fluorescence Workshop.
- Asch, T. (2009). *Self-Triggering of Radio Signals from Cosmic Ray Air Showers*. FZKA Report 7459, Forschungszentrum Karlsruhe.
- Askaryan, G. A. (1962). Soviet Phys. JETP, 14: 441.
- Askaryan, G. A. (1965). Soviet Phys. JETP, 21: 658.
- Auger, P. et al. (1939). *Extensive Cosmic-Ray Showers*. Reviews of Modern Physics, 11: 288–291. doi:10.1103/RevModPhys.11.288.
- Baade, W. and Zwicky, F. (1934). *Remarks on super-novae and cosmic rays*. Phys. Rev., 46 (1): 76–77. doi:10.1103/PhysRev.46.76.2.
- Baltrusaitis, R. M. et al. (1985). *The Utah Fly's Eye detector*. Nuclear Instruments and Methods in Physics Research Section A: Accelerators, Spectrometers, Detectors and Associated Equipment, 240 (2): 410 – 428. doi: DOI:10.1016/0168-9002(85)90658-8.
- Bass, S. A., Belkacem, M., Bleicher, M. et al. (1998). *Microscopic models for ultrarelativistic heavy ion collisions*. Progress in Particle and Nuclear Physics, 41: 255 – 369. doi:DOI:10.1016/S0146-6410(98)00058-1.
- Berezhko, E. G. (2008). *Cosmic Rays from Active Galactic Nuclei*. The Astrophysical Journal Letters, 684 (L69-L71). doi:doi:10.1086/592233.
- Berezinsky, Veniamin (2005). *Dip in uhedr and transition from galactic to extragalactic cosmic rays*. URL <http://fr.arxiv.org/abs/astro-ph/0509069>.
- Bergmann, T. et al. (2007). *One-dimensional hybrid approach to extensive air shower simulation*. Astroparticle Physics, 26 (6): 420 – 432. doi:DOI:10.1016/j.astropartphys.2006.08.005.
- Blümer, J., Engel, R. and Hörandel, J. R. (2009). *Cosmic rays from the knee to the highest energies*. Progress in Particle and Nuclear Physics, 63: 293–338. doi:10.1016/j.ppnp.2009.05.002.
- Budnev, N. M. and et al. (Tunka Collaboration) (2009). *The Tunka-133 EAS Chrenkov array - status, first results and plans*. In Proceedings of the 31st ICRC, Łódź, Poland, 1069. astro-ph/1003.0089.
- Buitink, S. et al. (LOPES Collaboration) (2007). *Amplified radio emission from cosmic ray air showers in thunderstorms*. Astronomy & Astrophysics, 467: 385–394. doi:10.1051/0004-6361:20066006.

- CTA consortium (2010). *Design Concepts for the Cherenkov Telescope Array CTA*. ArXiv:1008.3703.
- Dawson, B. R. and et al. (Pierre Auger Collaboration) (2007). *Hybrid Performance of the Pierre Auger Observatory*. In Proc. of the 30th ICRC, Merida, Mexico. Astro-ph/0706.1105, URL <http://arxiv.org/abs/0706.1105>.
- de Vries, K. D., Scholten, O. and Werner, K. (2010). *Modeling radio signals from Extensive Air Showers*. Nucl. Instrum. Meth., in press.
- DuVernois, M. A., Cai, B. and Kleckner, D. (2005). *Geosynchrotron radio pulse emission from extensive air showers: Simulations with AIRES*. In Proc. of the 29th ICRC, Pune, India, 311–+.
- Engel, R., Kalmykov, N. N. and Konstantinov, A. A. (2005). *Simulation of Cherenkov and Synchrotron Radio Emission in EAS*. In Proc. of the 29th ICRC, Pune, India, volume 6, 9–12.
- Falcke, H. and Gorham, P. W. (2003). *Detecting radio emission from cosmic ray air showers and neutrinos with a digital radio telescope*. Astropart. Physics, 19: 477–494. doi:DOI:10.1016/S0927-6505(02)00245-1.
- Falcke, H. et al. (LOPES Collaboration) (2005). *Detection and imaging of atmospheric radio flashes from cosmic ray air showers*. Nature, 435: 313–316. doi:10.1038/nature03614.
- Falcke, H. et al. (LOFAR Collaboration) (2006). *A very brief description of LOFAR - the Low Frequency Array*. In IAU GA 2006, Highlights of Astronomy (edited by van der Hucht, K. A.), volume 14. Astro-ph/0610652, [astro-ph/0610652](http://arxiv.org/abs/astro-ph/0610652).
- Fermi, E. (1949). *On the Origin of Cosmic Radiation*. Physical Review, 75 (8): 1169.
- Fliescher, S. et al. (Pierre Auger Collaboration) (2010). *Radio Detection of Cosmic-Ray-Induced Air Showers at the Pierre Auger Observatory*. Proceedings of the ARENA 2010 Conference, Nantes, France, Nuclear Instruments and Methods in Physics Research A. doi:10.1016/j.nima.2010.11.045.
- Gaisser, T. K., Protheroe, R. J., Turver, K. E. and McComb, T. J. L. (1978). *Cosmic ray showers and particle physics at energies 10^{15} - 10^{18} eV*. Rev. Mod. Phys., 50 (4): 859–880. doi:10.1103/RevModPhys.50.859.
- Gaisser, T. K. and Stanev, T. (2006). *High-energy cosmic rays*. Nuclear Physics A, 777: 98–110.

- Giller, M. et al. (2004). *Energy spectra of electrons in the extensive air showers of ultra-high energy*. Journal of Physics G: Nuclear and Particle Physics, 30 (2): 97. doi:10.1088/0954-3899/30/2/009.
- Greisen, K. (1966). Phys. Rev. Lett., 16: 748–750.
- Haungs, A., Rebel, H. and Roth, M. (2003). *Energy spectrum and mass composition of high-energy cosmic rays*. Reports on Progress in Physics, 66 (7): 1145. URL <http://stacks.iop.org/0034-4885/66/i=7/a=202>.
- Heck, D. et al. (1998). *CORSIKA: A Monte Carlo Code to Simulate Extensive Air Showers*. FZKA Report 6019, Forschungszentrum Karlsruhe.
- Heitler, W. (1954). The Quantum Theory of Radiation. Oxford University Press, London, third edition.
- Hess, V. F. (1912). Z. Phys., 13: 1084.
- Hinton, J. A. (2004). *The status of the H.E.S.S. project*. New Astron.Rev., 48: 331–337.
- Hoover, S. et al. (ANITA-Collaboration) (2010). *Observation of ultrahigh-energy cosmic rays with the anita balloon-borne radio interferometer*. Phys. Rev. Lett., 105 (15): 151101. doi:10.1103/PhysRevLett.105.151101.
- Hörandel, J. R. (2004). *Models of the knee in the energy spectrum of cosmic rays*. Astroparticle Physics, 21: 241–365.
- Horneffer, A. (LOFAR CR-Team) (2010). *Air Shower Measurements with LOFAR*. In Proceedings of the ARENA 2010 conference, Nantes, France, Nuclear Methods in Physics Research A.
- Horneffer, A., Apel, W. D., Arteaga, J. C. and et al. (LOPES Collaboration) (2008). *Primary Particle Energy Calibration of the EAS Radio Pulse Height*. In International Cosmic Ray Conference, volume 4 of *International Cosmic Ray Conference*, 83–86.
- Horneffer, A. et al. (LOPES Collaboration) (2004). *LOPES: detecting Radio Emission from Cosmic Ray Air Showers*. In Astronomical Telescopes and Instrumentation 2004: Gravitational Wave and Particle Astrophysics Detectors, Proceedings of the SPIE, volume 5500, 129–138.
- Huege, T. (2004). Radio Emission from Cosmic Ray Air Showers. Ph.D. thesis, Rheinische Friedrich-Wilhelms-Universität Bonn, Germany. URL <http://nbn-resolving.de/urn:nbn:de:hbz:5N-04797>.

- Huege, T. (2009). *Simulations and theory of radio emission from cosmic ray air showers*. In Proceedings of the ARENA 2008 conference, Rome, Italy, Nuclear Methods in Physics Research A, volume 604, S57–S63. doi:10.1016/j.nima.2009.03.165.
- Huege, T. and Falcke, H. (2003). *Radio emission from cosmic ray air showers. Coherent geosynchrotron radiation*. Astronomy & Astrophysics, 412: 19–34. doi:10.1051/0004-6361:20031422.
- Huege, T. and Falcke, H. (2005a). *Radio emission from cosmic ray air showers. Monte Carlo simulations*. Astronomy & Astrophysics, 430: 779–798. doi:10.1051/0004-6361:20041873.
- Huege, T. and Falcke, H. (2005b). *Radio emission from cosmic ray air showers: Simulation results and parametrization*. Astropart. Phys., 24: 116. doi:10.1016/j.astropartphys.2005.05.008.
- Huege, T., Ludwig, M., Scholten, O. and de Vries, K. D. (2010a). *The convergence of EAS radio emission models and a detailed comparison of REAS3 and MGMR simulations*. NIM A, in press. Proceedings of the 2010 ARENA conference, Nantes, France, arXiv:1009.0346.
- Huege, T., Ulrich, R. and Engel, R. (2006). *Geosynchrotron radio emission from CORSIKA-simulated air showers*. In Proc. of the ARENA2006 conference, Newcastle, England.
- Huege, T., Ulrich, R. and Engel, R. (2007). *Monte Carlo simulations of geosynchrotron radio emission from CORSIKA-simulated air showers*. Astropart. Physics, 27: 392–405. doi:10.1016/j.astropartphys.2007.01.006.
- Huege, T., Ulrich, R. and Engel, R. (2008). *Dependence of geosynchrotron radio emission on the energy and depth of maximum of cosmic ray showers*. Astroparticle Physics, 30: 96–104. doi:10.1016/j.astropartphys.2008.07.003.
- Huege, T. et al. (LOPES Collaboration) (2010b). *The LOPES experiment - recent results, status and perspectives*. doi:10.1016/j.nima.2010.11.081. Proceedings of the ARENA 2010 conference, Nantes, France.
- Isar, P. G., Apel, W. D., Arteaga, J. C. and et al. (LOPES Collaboration) (2009). *Polarization studies of the EAS radio emission with the LOPES experiment*. In Proceedings of the 31st ICRC, Lodz, Poland, 1128.
- Jackson, J. D. (1975). Classical Electrodynamics. John Wiley & Sons, New York, second edition.

- James, C. W., Falcke, H., Huege, T. and Ludwig, M. (2010). *An ‘endpoint’ formulation for the calculation of electromagnetic radiation from charged particle motion*. Phys Rev. E, submitted. arXiv:1007.4146.
- Jelley, J. V. et al. (1965). *Radio Pulses from Extensive Cosmic-Ray Air Showers*. Nature, 205: 327.
- Kahn, F. D. and Lerche, I. (1966). *Radiation from cosmic ray air showers*. In Proc. Roy. Soc., volume A-289, 206.
- Kazanas, D. and Nicolaidis, A. (2003). *Cosmic rays and large extra dimensions*. GEN.REL.GRAV., 35: 1117. URL <http://www.citebase.org/abstract?id=oai:arXiv.org:hep-ph/0109247>.
- Knapp, J. et al. (2003). *Extensive air shower simulations at the highest energies*. Astropart. Physics, 19: 77–99.
- Konstantinov, A. A. (2009). *Radio emission of extensive air showers as a detection method for ultra-high energy cosmic rays*. Ph.D. thesis, Lomonosov Moscow State University, Moscow.
- Lafèbre, S. et al. (2009). *Universality of electron-positron distributions in extensive air showers*. Astroparticle Physics, 31: 243–254.
- Lagage, P. O. and Cesarsky, C. J. (1983). *Cosmic-ray shock acceleration in the presence of self-excited waves*. Astronom. Astrophys., 118: 223–228.
- Lidvansky, A. S. (2005). *Air Cherenkov Methods in Cosmic Rays: A Review and Some History*. [astro-ph/0504269](http://arxiv.org/abs/astro-ph/0504269).
- Link, K. et al. (LOPES Collaboration) (2011a). *Interferometrische Analyse der LOPES-Daten und REAS3-Simulationen*. Beitrag zur DPG-Frühjahrstagung in Karlsruhe.
- Link, K. et al. (LOPES Collaboration) (2011b). *The LOPES experiment*. In Nuclear Physics B (Proc. Suppl.); Proc. of the CRIS2010 conference, Catania, Italy, volume 212-213C, 323–328.
- LOFAR Team (2011). [Http://www.lofar.org/first-pulsar-polarisation-profiles-lofar](http://www.lofar.org/first-pulsar-polarisation-profiles-lofar).
- Ludwig, M. and Huege, T. (2010a). *REAS3: A revised implementation of the geosynchrotron model for radio emission from air showers*. Nucl. Instr. Meth. A, in press. doi:10.1016/j.nima.2010.10.115. Doi:10.1016/j.nima.2010.10.115.

- Ludwig, M. and Huege, T. (2010b). *REAS3: Monte Carlo simulations of radio emission from cosmic ray air showers using an “end-point” formalism*. *Astropart. Phys.*, 34: 438–446. doi:10.1016/j.astropartphys.2010.10.012. Doi:10.1016/j.astropartphys.2010.10.012.
- Matthews, J. N. (2005). *A Heitler model of extensive air showers*. *Astroparticle Physics*, 22: 387–397. doi:10.1016/j.astropartphys.2004.09.003.
- Medvedev, M. V. (2007). *Extragalactic shocks as cosmic accelerators*. *Highlights of Astronomy*, 14: 95–96. doi:10.1017/S1743921307009970.
- Melissas, M. et al. (Pierre Auger Collaboration) (2010). *Overview of radio-detection of cosmic ray air showers and prospects for a large scale experiment*. In Proceedings of the 22nd ECRS, Turku, Finland, to appear in: *Astrophysics and Space Sciences Transactions*.
- Menjo, H. et al. (2011). *Monte Carlo study of forward π_0 production spectra to be measured by the LHCf experiment for the purpose of benchmarking hadron interaction models at 10^{17} eV*. *Astroparticle Physics*, 34 (7): 513 – 520. doi: DOI:10.1016/j.astropartphys.2010.11.002.
- Neddermeyer, S. H. and Anderson, C. D. (1937). *Note on the nature of cosmic-ray particles*. *Phys. Rev.*, 51 (10): 884–886. doi:10.1103/PhysRev.51.884.
- Nehls, S. (2008). *Calibrated Measurements of the Radio Emission of Cosmic Ray Air Showers*. FZKA Report 7440, Forschungszentrum Karlsruhe.
- Nehls, S. et al. (2008). *Amplitude calibration of a digital radio antenna array for measuring cosmic ray air showers*. *Nucl. Instr. Meth.*, 589: 350–361. Submitted.
- Nigl, A., Apel, W. D., Arteaga, J. C. and et al. (LOPES Collaboration) (2008). *Frequency spectra of cosmic ray air shower radio emission measured with LOPES*. *Astronomy & Astrophysics*, 488: 807–817.
- Ostapchenko, S. (2006). *QGSJET-II: results for extensive air showers*. *Nuclear Physics B - Proceedings Supplements*, 151 (1): 147 – 150. doi:DOI:10.1016/j.nuclphysbps.2005.07.027. ISVHECRI 2004.
- Palmieri, N. (2011). in preparation. Ph.D. thesis.
- Pierog, T. et al. (2006). *First results of fast one-dimensional hybrid simulation of EAS using conex*. *Nuclear Physics B - Proceedings Supplements*, 151 (1): 159 – 162. doi:DOI:10.1016/j.nuclphysbps.2005.07.029. VERY HIGH ENERGY COSMIC RAY INTERACTIONS.

- Pierre Auger Collaboration (1996). *The Pierre Auger Project Design Report*. Technical report. [Http://www.auger.org](http://www.auger.org).
- Platino, M. (Pierre Auger Collaboration) (2009). *AMIGA - Auger Muons and Infill for the Ground Array of the Pierre Auger Observatory*. In Proceedings of the 31st ICRC, Lodz, Poland.
- Privitera, P. (2010). *Microwave detection of Ultra-High Energy Cosmic Rays*. In Proceedings of the International Symposium on the Recent Progress of Ultra-high Energy Cosmic Ray Observation, Nagoya, Japan.
- Protheroe, R. J. and Szabo, A. P. (1992). *High energy cosmic rays from active galactic nuclei*. Phys. Rev. Lett., 69 (20): 2885–2888. doi:10.1103/PhysRevLett.69.2885.
- Ptuskin, V. S. et al. (1993). *Diffusion and drift of very high energy cosmic rays in galactic magnetic fields*. Astron. Astroph., 268: 726–735.
- Putze, A. (2010). *Direct cosmic-ray detection*. Nuclear Instruments and Methods in Physics Research Section A: Accelerators, Spectrometers, Detectors and Associated Equipment, In Press, Corrected Proof: -. doi:DOI:10.1016/j.nima.2010.11.133.
- Ravel, O. (CODALEMA Collaboration) (2010). *The CODALEMA experiment*. Nuclear Instruments and Methods in Physics Research Section A: Accelerators, Spectrometers, Detectors and Associated Equipment, In Press, Corrected Proof: -. doi:DOI:10.1016/j.nima.2010.12.057.
- REAS-Webpage (2011). URL <http://www-ik.fzk.de/~huege/reas>.
- Röttgering, H. et al. (2003). *LOFAR: a new radio telescope for low frequency radio observations: science and project status*. In Texas in Tuscany. XXI Symposium on Relativistic Astrophysics, 69–76. doi:10.1142/9789812704009_0007.
- Scholten, O. and Werner, K. (2009). *Macroscopic model of geomagnetic-radiation from air showers*. Nucl. Instr. Meth. A, 604: S24–S26.
- Scholten, O., Werner, K. and Rusydi, F. (2008). *A macroscopic description of coherent geo-magnetic radiation from cosmic-ray air showers*. Astroparticle Physics, 29: 94–103. astro-ph/0709.2872.
- Schröder, F. G. (2011). Instruments and Methods for the Radio Detection of High Energy Cosmic Rays. Ph.D. thesis. URL <http://digbib.ubka.uni-karlsruhe.de/volltexte/1000022313>.

- Schröder, F. G. et al. (LOPES Collaboration) (2010). *On Noise Treatment in Radio Measurements of Cosmic Ray Air Showers*. In Nucl. Instr. and Meth. A; Proceedings of the ARENA 2010 conference, Nantes, France. doi:DOI:10.1016/j.nima.2010.11.009. DOI: 10.1016/j.nima.2010.11.009, in press.
- Sciutto, S. J. (1999). *AIRES: A system for air shower simulations (Version 2.2.0)*. astro-ph/9911331. , see also <http://www.fisica.unlp.edu.ar/auger/aires>, URL <http://arXiv.org/abs/astro-ph/?9911331>.
- Sigl, G., Schramm, D. N. and Bhattacharjee, P. (1994). *On the origin of highest energy cosmic rays*. Astroparticle Physics, 2: 401–414. doi:10.1016/0927-6505(94)90029-9.
- Simpson, J. A. (1983). *Elemental and isotopic composition of the galactic cosmic rays*. Annual Review of Nuclear and Particle Science, 33: 323–382. doi:10.1146/annurev.ns.33.120183.001543.
- Suprun, D. A., Gorham, P. W. and Rosner, J. L. (2003). *Synchrotron radiation at radio frequencies from cosmic ray air showers*. Astropart. Physics, 20: 157–168. doi:10.1016/S0927-6505(03)00177-4.
- Swordy, S. P. (1995). *Expectations for cosmic ray composition changes in the region 10^{15} to 10^{16} eV*. In Proceedings of the 24th ICRC, Rome, Italy, volume 2, 697.
- Telescope Array Collaboration (2011). URL <http://www.telescopearray.org>.
- Ulrich, R. (2010). *Fast Hybrid Air Shower Simulations with CONEX*. Lecture at CORSIKA school 2010 in Ooty, India.
- van den Berg, A. et al. (Pierre Auger Collaboration) (2007). *Radio detection of high-energy cosmic rays at the Pierre Auger Observatory*. In Proceedings of the 30th ICRC, Merida, Mexico. Astro-ph/0708.1709.
- van den Berg, A. et al. (Pierre Auger Collaboration) (2009). *Radio detection of high-energy cosmic rays at the Pierre Auger Observatory*. In Proceedings of the 31st ICRC, Lodz, Poland.
- de Vries, K. D., Scholten, O. and Werner, K. (2010). *Macroscopic geo-magnetic radiation model; polarization effects and finite volume calculations*. Nuclear Instruments and Methods in Physics Research Section A: Accelerators, Spectrometers, Detectors and Associated Equipment, In Press, Corrected Proof: —. doi:DOI:10.1016/j.nima.2010.10.127.

- Weber, J. H. et al. (KASCADE Collaboration) (1999). *Analysis of the muon/electron ratio in EAS*. In Proceedings of the 26th ICRC, Salt Lake City, Utah, USA, volume 1, 341.
- Werner, F. (CROME Collaboration) (2011). *Das CROME-Experiment zur Messung der Mikrowellenemission ausgedehnter Luftschauer*. Beitrag zur DPG-Frühjahrstagung in Karlsruhe.
- Werner, K. and Scholten, O. (2008). *Macroscopic Treatment of Radio Emission from Cosmic Ray Air Showers based on Shower Simulations*. *Astroparticle Physics*, 29: 393–411. doi:10.1016/j.astropartphys.2008.04.004.
- Zas, E., Halzen, F. and Stanev, T. (1992). *Electromagnetic pulses from high-energy showers: Implications for neutrino detection*. *Phys. Rev. D*, 45: 362–376. doi:10.1103/PhysRevD.45.362.
- Zatsepin, G. and Kuzmin, V. (1966). *Zh. Eksp. Teor. Fiz.*, 4: 114–117.

Meine Doktorarbeit entstand durch die Hilfe und Unterstützung vieler Menschen. Mein besonderer Dank gilt:

Prof. Johannes Blümer, der durch die Übernahme des Referats meine Arbeit am IEKP ermöglichte und mir sein Vertrauen entgegenbrachte.

Prof. Michael Feindt danke ich für die Übernahme des Korreferats.

Hervorheben möchte ich die Betreuung von Tim Huege, der mich in seiner Nachwuchsgruppe einstellte und förderte wie forderte. Ich danke ihm für seine Geduld, Ratschläge, offene Kritik und Aufgaben, die zu meiner fachlichen wie persönlichen Entwicklung viel beigetragen haben.

Daran anschließend gilt mein Dank Andreas Haungs, der mir die Zeit meiner Doktorarbeit nicht nur durch seine fachliche Kompetenz erleichtert hat, sondern vor allem durch seine stets aufmunternde Art in den mühsamen Phasen immer motivieren konnte.

Die Betreuung von Andreas und Tim zusammen mit der Wahl des Themas haben keinen Zweifel aufgebracht, dass ich für mich die richtige Entscheidung zur Promotion getroffen habe.

Den Rückhalt und die Zusammenarbeit zwischen den Mitgliedern der “kosmischen Karlsruher”, v.a. der Radiogruppe, empfand ich als besonders stark und dafür möchte ich allen danken. Insbesondere:

Katrin Link für die vielen Diskussionen sowohl ihr Thema als auch meins betreffend, die sportliche Begleitung, gemeinsamen Schichten und vor allem für die neue Freundschaft. Für diese danke ich ebenso Julia Bäuml als Mitgründerin der Killergirls und für die Einführung und tolle Zeit in Malargüe.

Nunzia Palmieri (*grazie per i bei momenti insieme*) und Gina Isar danke ich für die gemeinsame Zeit im Büro und die vielen Gespräche, die sich daraus ergeben haben.

Mein Dank gilt Frank Schröder nicht nur für die Erstellung der Bilder in Kapitel 7.2 sondern auch für seine Zuverlässigkeit und den Antrieb für das Erstellen des neuen Selektionsverfahrens. Vor allem bei Diskussionen um dieses Verfahren und generell bei Fragen um CORSIKA war Tanguy Pierog mir stets eine große Hilfe. Marcel Finger und Michael Wommer waren bereitwillig meine Ansprechpartner, wann immer es um KASCADE(-Grande) ging.

Die Hilfsbereitschaft und ehrliche Meinung von Benjamin Fuchs lernte ich sehr zu schätzen. Maximilien Melissas danke ich für die vielen lustigen Ideen, das gute Essen und dafür dass ich ihm wenigstens manchmal helfen durfte und konnte - Je te remercie de ta confiance!

Für diverse Hilfeleistungen und viele schöne Erinnerungen, die mir an die gemeinsame Zeit bleiben, danke ich außerdem: Adrian Schmidt, Christoph Rühle, Dieter Manger, Donghwa Kang, Doris Wochele, Fabiana Cossavella, Felix Werner, Hans-Jürgen Gils, Heike Bolz, Horia Bozdog, Jan Oertlin, Jan Reich, Jan Weseler, Jürgen Wochele, Klaus Bekk, Markus Roth, Martin Will, Michael Konzack, Paul Doll, Ralph Engel, Stefan Braun, Steffen Nehls, Steffen Müller und Sven Over.

Sabine Bucher und Brigitte Gering danke ich für die Entlastung im Bereich aller Verwaltungsaufgaben und die große Hilfe bei jeglichen Dienstreisen.

Außerhalb des KIT danke ich Clancy W. James, Heino Falcke, Krijn D. de Vries, Olaf Scholten und Stijn Buitink für die vielen hilfreichen Diskussionen sowie der LOPES-, der KASCADE-Grande- und der Pierre Auger-Kollaboration.

Privat haben mich ebenfalls viele Freunde auf meinem Weg unterstützt (und ertragen). Besonders danken möchte ich Mareike, Steffi, Vio und Irmi für langjährige beste Freundschaften sowie Oliver (nicht nur) für die regelmäßigen Mittagspausen, dem Kochkreis, den BDP-lern (Andreas, Horst, Geli, Steve, Lena, Sebastian,...) und “meinen” Physikern (Tobias, Hauke, Daniel, Nicolas, Markus), die mich seit Beginn des Studiums begleiten und motivieren, allen voran Petra, der ich besonders für die ehrliche und herzliche Freundschaft danken möchte.

Ohne die Zuversicht, das Verständnis und den Rückhalt meiner gesamten Familie wäre diese Arbeit nicht möglich gewesen. Besonders danke ich meinen Eltern Gerd und Ute für “einfach alles” und meinen Geschwistern Angela, Andreas und Christian dafür, dass sie so sind wie sie sind und wir zusammen q-l. Außerdem danke ich meinem Schwager Florian für seine hilfreichen Ratschläge und meinem Neffen Kelvin für seinen verzaubernden Charme, der mich die Strapazen der Doktorarbeit oftmals vergessen ließ.

Abschließend danke ich Daniel (alias “King Huber”), der mich sowohl privat als auch beruflich unterstützt, motiviert und begleitet und mich mit seiner lebenswerten Art stets zum Lachen bringt (was nicht nur an seinem Repertoire an anspruchsvollen Witzen liegt). Ich danke dir von Herzen für deinen Halt, deine Zuversicht und unsere gemeinsamen Erlebnisse und freue mich auf alle, die uns noch erwarten.